Great are the works of the Lord, studied by all who delight in them.

Psalm 111:2 ESV

University of Alberta

Petrographic and X-ray Microtomographic Analysis of the Upper Montney
Formation, Northeastern British Columbia, Canada

by

Tiffany Leigh Playter

A thesis submitted to the Faculty of Graduate Studies and Research
in partial fulfillment of the requirements for the degree of

Master of Science

Department of Earth and Atmospheric Sciences

©Tiffany Leigh Playter
Spring 2013
Edmonton, Alberta

Dedication

This work is dedicated to my daughter Julia Playter. Your laughter and smiles made this work possible.

Abstract

Utilizing electron microprobe (EMP), scanning electron microscope (SEM) and petrographic analysis, 14 thin sections from the Upper Montney Formation were analyzed. Five microfacies were identified. Rock types observed include: dolomitic lithic arkos, dolomitic litharenite, dolomitic feldspathic litharenite and dolomitic feldspathic litharenite.

These microfacies are interpreted to be dominantly event beds, possibly sourced from turbidity currents. Depositional environments range from the lower shoreface to offshore. Pyrite analysis suggests deposition in dominantly disoxyic conditions, with 3 anoxia spikes in association with a decrease in ocean acidity.

Additionally, microfocus-computed tomographic analysis was conducted on a representative sample from the Upper Montney. By comparing these analyses with EMP images, 3-D mineral characterization was made possible. This technique reveals low overall porosity and the presence of dedolomite.

Acknowledgements

     I would like to thank Sergei Matveev for assistance with the microprobe, Andrew Locock for the helpful discussions about x-rays and Deanne Rollings for help with the SEM. Additionally, thanks to Greg Baniak and Carolyn Currie for their helpful edits. Thanks also to the Ichnology Research Group at the University of Alberta for their general help and support. My supervisors, Murray Gingras and J-P Zonneveld deserve extra thanks for their many hours of editing, discussion and general guidance.

     Furthermore, thanks to my friends and family for their support. Specifically my parents, Dixie and Ray Davies and siblings Amanda, Victor and Ben. Thanks also to my mother-in-law Diane and father-in-law Gordon for their support. Lastly, I would like to thank my husband, Mike, who helped me in every way possible and my daughter Julia who constantly inspires me to be better.

     I thank God also, for pulling me through some hard times, instilling me with curiosity and giving me the opportunity to pursue it. Thank you everyone.

Table of Contents

List of Tables

List of Figures

Introduction

Introduction

      The Montney Formation consists of sandstone, siltstone and coquina that were deposited along the western margin of Pangaea during the Lower Triassic (see Figure 1; Davies et. al., 1997; Moslow and Davies, 1997; Dixon, 2000; Moslow, 2000; Utting et. al., 2005; Hayes et. al., 2007; Zonneveld et. al., 2010). Mineralogically, the Montney Formation contains a low proportion of clay minerals (2 to 8% Illite) and is dominated by quartz, dolomite, potassium feldspar, plagioclase feldspar, mica, calcite and pyrite. Although percentages of minerals (such as quartz) vary, in general, quartz content is 60% or less and dolomite is the most abundant type of lithic fragment. Observable rock types include: dolomitic lithic arkose, dolomitic feldspathic litharenite and dolomitic litharenite. These rock types were noted during this study, which focused on the lithology of the Upper Montney Formation and questions related to the conditions during deposition. To this end, thin section analysis, in addition to scanning electron microscope (SEM) and electron microprobe (EMP) analysis, was conducted on 14 siltstone samples of the Montney Formation from northern British Columbia. Additionally, a sample was analysed using a new method of comparative analysis which combines EMP analysis and micro-computerised tomographic (micro-ct) imaging. This allowed for 3-D visualisation of the mineral phases.

      Microfocus computed tomographic (micro-ct) analysis has been utilized in sedimentological, paleontological and porosity studies (Kentner, 1989 ; Bertels *et. al.,* 2001; Van Geet *et. al.,* 2002; Snelling *et. al.*, 2010;). In addition, this form of analysis has also begun to be applied to mineralogical studies (Remeysen and Swennen, 2008). These analysis have been carried out largely using techniques such as dual-energy scanning. In contrast, one of the aims of this study is to explore an alternative method, calibration using electron microprobe analysis (EMP). By using a micro-computed tomographic scanner, in partnership with an electron microprobe, 3-D analyses of the mineral composition and fabric of a fine grained sample (average grain size less than 10 microns) have been attained.

Additionally, five distinct microfacies were observed using SEM, EMP and petrographic imaging. The analysis of these microfacies reveals deposition sourced by storm activity and ephemeral flooding. Bioturbation was observed to be sporadic and rare and may reflect doomed pioneers. Body fossils were observed to be dissolved and the overall biological imprint on the Montney is low. Pyrite analysis reveals deposition in a dysoxic environment and dolomite grains eroded by calcite (dedolomite) points to a large detrital dolomite component that may have been sourced by sulphate reducing bacteria. Analysis of these microfacies has produced a diagenetic model for Montney sedimentation which includes: the deposition of detrital grains (quartz, dolomite, feldspar, mica and bioclastic debris) below calcium compensation depth, shallow burial, rapid transport through the sulphate reduction zone, and subsequent calcite cementation and dedolomitization. Kerogen, preserved within pore spaces is a likely source for Montney hydrocarbons.

Epoch/Age			Subsurface Alberta and BC	Outcrop Jasper Area
Middle Triassic		Ladinian 242 Ma	Halfway Formation	Llama Member
		Anisian 247 Ma	Doig Formation ⎯ ⎯ ⎯ ⎯ Phosphate Zone	Whistler Member
Lower Triassic	Olenekian	Spathian	Montney Formation	Vega Member
		Smithian 251 Ma		
	Induan	Dienerian		Phroso Member
		Griesbachian 252 Ma		

Figure 1 Geological Timescale showing lithostratigraphic divisions for the Lower and Middle Triassic modified from Zonneveld *et. al.*'s (2010) adaptation of Tozer (2010), Orchard and Tozer (1997) and Orchard and Zonneveld (2009). Dates were taken from Lukas (2010). Note that the nomenclature changes from subsurface to outcrop and varies by location.

References

Bertels, S.P., Dicarlo, D.A. and Blunt, M.J., 2001. Measurement of aperture distribution, capillary pressure, relative permeability, and in situ saturation in a rock fracture using computerized tomography scanning. Water Resources Research v. 37, p.649-662.

Davies, G.R., Moslow, T.F. and Sherwin, M.D. 1997. The Lower Triassic Montney Formation, west-central Alberta. In: Triassic of the Western Canada Sedimentary Basin. T.F. Moslow and J. Wittenberg (eds.) Bulletin of Canadian Petroleum Geology, v. 45, p. 474-505.

Dixon, J. 2000. Regional lithostratigraphic units in the Triassic Montney Formation of western Canada. Bulletin of Canadian Petroleum Geology, v.48, p. 80-83.

Hayes, L.E., Beatty, T.W., Henderson, C.M., Love, G.D., and Summons, R.E., 2007. Evidence for photic zone euxinia through the end-Permian mass extinction in the Panthalassic Ocean (Peace River Basin, Western Canada). Palaeoworld, v. 16, p. 39-50.

Kenter, J.A.M., 1989. Applications of computerized-tomography in sedimentology. Marine Geotechnology v. 8, p. 201–211.

Lukas, S.G. 2010. The Triassic timescale: an introduction. Geological Society, London, Special Publication, v. 334, p. 1-16.

Moslow, T.F. 2000. Reservoir architecture of a fine-grained turbidite system: Lower Triassic Montney Formation, Western Canada Sedimentary Basin. *In:*

Deep-water reservoirs of the world, Conference Proceedings, Gulf Coast SEPM. P. Weimer, R.M. Slatt, J. Coleman, N.C. Rosen, H. Nelson, A.H. Bouma, M.J. Styzen, and D.T. Lawrence (eds.). p. 686-713.

Moslow, T.F. and Davies, G.R. 1997. Turbidite reservoir facies in the Lower Montney Formation, west-central Alberta. *In:* Triassic of the Western Canada Sedimentary Basin. T.F. Moslow and J. Wittenberg (eds.), Bulletin of Canadian Petroleum Geology v. 45, p. 507-536.

Orchard, M.J. and Tozer, E.T., 1997. Triassic conodont biochronology, its calibration with the ammonoid standard, and a biostratigraphic summary for the Western Canada. In: Moslow, T.F. and Wittenberg (eds.), Triassic of the Western Canada Sedimentary Basin. Bulletin of Canadian Petroleum Geology, v. 45, p. 675-692.

Orchard, M.J and Zonneveld, J-P. 2009. The Lower Triassic Sulphur Mountain Formation in the Wapiti Lake area: lithostratigraphy, conodont biostratigraphy, and a new biozonation for the lower Olenekian (Smithian). Canadian Journal of Earth Sciences 46, p. 757-790.

Remeysen, K. and Swennen, R., 2008. Application of microfocus computed tomography in carbonate reservoir characterization: Possibilities and limitations. Marine and Petroleum Geology v. 25, p. 486-499.

Snelling, A., Zalasiewicz, J., and Reeds, I., 2010. Using x-ray images to analyze graptolite distribution and alignment in welsh mudrocks. Proceedings of the Yorksire Geological Society v. 58, p. 129–140.

Tozer, E.T., 1994, Canadian Triassic ammonoid faunas: Geological Survey of Canada Bulletin, v. 467, p. 663

Utting, J., MacNaughton, R.B., Zonneveld, J-P., and Fallas, K., 2005.
Palynostratigraphy, organic matter and thermal maturity of the Lower Triassic
Toad, Grayling and Montney formations of Yukon, British Columbia and
Alberta and comparison with the Sverdrup Basin, Nunavut. BCPG 53, p. 5-24.

Van Geet, M., Swennen, R., Durmishi, C., Roure, F. and Muchez, P., 2002.
Paragenesis of Cretaceous to Eocene carbonate reservoirs in the Ionian fold
and thrust belt (Albania): relation between tectonism and fluid flow.

Zonneveld, J-P., Gingras, M.K. and Beatty, T.W. 2010. Diverse ichnofossil
assemblages from the Lower Triassic of northeastern British Columbia:
evidence for shallow marine refugia on the northwestern coast of Pangaea.
Palaios, v. 25, p. 368-392.

Petrographic analysis of the Lower Triassic Montney Formation, northwestern British Columbia, Canada

Introduction

The Lower Triassic Montney Formation of the Western Canada Sedimentary Basin consists of sandstone, siltstone and coquina that were deposited along the western margin of Pangaea (Davies et. al., 1997; Moslow and Davies, 1997; Dixon, 2000; Moslow, 2000; Utting et. al., 2005; Hayes et. al., 2007; Zonneveld et. al., 2010). Shoreface and offshore (including turbidite) successions constitute the majority of clastic sedimentary units preserved in the Lower Triassic of western Canada (Davies et. al., 1997; Dixon, 2000; Moslow, 2000; Zonneveld et. al., 2010). The Montney Formation is up to 300 m thick and extends over an area approximately 150,000 km² in north-eastern British Columbia and Alberta (Davies, 1997; Zonneveld et. al., 2010). Hydrocarbons are stored within organic-rich siltstone intervals with TOCs ranging from 0.5% to 7% (average of 4% in productive intervals) and original gas in place estimates range from 200 to 1500 TCF (5.67-42.48 million m³; Moslow, 2000; Ibrahimbas and Riediger, 2004; Faraj *et al*., 2002). The Montney Formation has become well known for its unconventional gas potential (Walsh et al., 2006; Zonneveld, 2009), but as yet, little has been published concerning the mineralogy of the fine-grained reservoir strata. The unit has a characteristic mineralogy consisting of quartz, dolomite, potassium feldspar, plagioclase feldspar, mica, phosphate and pyrite (Davies, 1997; Dixon, 2000; Moslow, 2000; Zonneveld et. al., 2010). Although often referred to as a shale-gas play, the Montney Formation contains a low proportion of clay minerals (2-8% Illite) in most areas and is dominated by silt-sized to very fine-grained sand-sized grains (Davies, 1997; Dixon, 2000; Moslow, 2000; Zonneveld et. al., 2010). These fine-grained deposits comprise the majority of the formation and are thus crucial to understanding not only reservoir characteristics, but the stratigraphic evolution of the Montney as well.

7

To gain insight pertaining to the mineralogy, inter-grain / cement relationships and depositional constraints on the Montney Formation, a petrographic investigation was initiated on the Upper Montney interval in the Kobes region of northern British Columbia. In addition to thin section analyses, samples were examined using a scanning electron microscope (SEM) and an electron microprobe (EMP). Five microfacies were observed (summarised in Table 1-1 and Figures 1-1 and 1-2).

Previous Work

The Montney Formation was first defined by Armitage (1962), who described the subsurface type section in northwestern Alberta located in Texaco NFA Buick Creek well 6-26-87-21W6. In the type section the lower Montney was described as an interbedded dark grey dolomitic siltstone and shale and the upper Montney was described as an interlaminated light brown siltstone and fine-grained sandstone (Armitage, 1962; Davies *et. al.* 1997). Gibson and Edwards (1990) noted that the Montney is generally either calcareous or dolomitic throughout its extent.

The Montney Formation was divided into three informal members and dated using palynology by Davies *et. al.* (1997): the Lower member (Griesbachian to Dienerian), the Coquinal Dolomite Middle (CDM) member (Dienerian to Smithian) and the Upper member (Smithian to Spathian). This classification scheme is most commonly used and is most applicable for Alberta in areas where the CDM is present. An alternative lithostratigraphic classification scheme was proposed by Dixon (2000). He proposed that the Lower member of Davies *et. al.*(1997) be referred to as the Sandstone member; the Coquinal Dolomite Middle member and the Upper member would also be renamed the Coquinal Dolomite member and the Siltstone member respectively. A fourth member (the Shale member) was also included by Dixon (2000) and the term Siltstone-sandstone member was used to delineate the Montney where no Middle member is present. This classification has been adopted by few practitioners and is not used in the present thesis. It has not proven to be an improvement on the framework developed by Davies et al. (1997). Within the study

area, the Montney Formation is divided informally into the Lower Montney and Upper Montney following common industry terminology.

A core analysis of the Montney turbidites in the Valhalla-La Glace area was conducted by Moslow and Davies (1997). Moslow (2000) also conducted a study on the Montney turbidites (in the region of the Sexsmith, Valhalla and La Glace fields) to produce facies interpretations and define reservoir characteristics. Ultimately, this study showed that turbidite deposition occurred along fault-controlled ramp breaks and was associated with syn-sedimentary tectonism. A detailed palynotological study was conducted by Utting *et. al.* (2005) on the lowermost Montney Formation in northeastern British Columbia, northwestern Alberta and southeastern Yukon. This study provided accurate dating, palaeoenvironmental information and a thermal maturation history. This study supported claims by Davies (1997) that the climate during Montney deposition was hot and arid.

Structural Setting

The Montney Formation is thickest in the area of the Peace River Embayment (PRE), a structural trough located on the western margin of the North American craton (see Figure 1-3; Barclay *et. al.*, 1990; Davies *et. al.,* 1997). The PRE was formed during the early Mississippian by the collapse of the Peace River Arch. It widened gradually as extension and subsidence took place. By the Triassic, it extended at least 350 km east to west and was 900 km long (NNW-SSE) (Barclay *et. al.*, 1990; Davies *et. al.,* 1997). Although the cratonic margin in the area of the PRE was previously thought to be tectonically stable and inactive during the Triassic (Davies, 1997) recent evidence suggests that this may not be the case. Eastward moving volcanic arcs, forearc and backarc basins occurred westward of the continental margin and collided with North America throughout the Mesozoic, with early collisions occurring in western and Northern Canada as early as the Lower Triassic (Berenak, 2006; Beranek and Mortensen, 2008; Ferri and Zonneveld, 2008). Tectonic events, including those to the west as well as activity to the south may have contributed to sedimentation in the PRE by causing the reactivation of faults in the

Dawson Creek Graben Complex (Davies, 1997). The Dawson Creek Graben Complex (DCGC) lies in the centre of the PRE and actively subsided during the Carboniferous and Permian (Barclay *et. al*., 1990). During the Triassic, the DCGC experienced continuous, but intermittent subsidence with episodic fault reactivation (Davies, 1997). The DCGC influenced Montney deposition throughout the PRE (Davies, 1997), and had a direct impact on the Montney succession looked at in this study as the itlies directly south of the study area. Reactivation of these faults (specifically the Ft. St. John Graben) may have been one of the triggers for turbidite deposition seen in the study samples.

Palaeoenvironmental Factors

The end-Permian mass extinction, which occurred roughly 252 million years ago, had a profound effect on organisms worldwide, particularly in western Canada (e.g., Hayes et. al., 2007; Zonneveld et al., 2010). This mass extinction was the most severe on record, with 90-95% of skeletonized marine species having gone extinct (Erwin, 2006). Within the marine realm, ~83% of genera, 57% of families and 17% of orders were lost (Raup, 1979). Regionally extensive, shallow water anoxic to dysoxic conditions are thought to have played a major role in the extinction (Hayes et. al., 2007; Zonneveld et. al., 2010). These oxygen-poor conditions extended into the proximal shelf and were globally extensive, with prolonged oxygen starved conditions persisting well into the Middle Triassic (Hayes et. al., 2007; Zonneveld et. al., 2010). This long-term anoxia delayed the recovery of post-extinction fauna for millions of years (Zonneveld et. al., 2010). Diversity (both global and within-habitat), for much of the Lower Triassic, remained low with impeded diversification and prolonged elevated extinction levels (Zonneveld et. al., 2010).

As well as pervasive anoxia, Early Triassic oceans were characterised by increased levels of dissolved CO_2 and thus increased oceanic acidity (Woods *et. al.,* 2007). This resulted in shallowing of the aragonite and calcite compensation depths (ACD and CCD; Woods *et. al.,* 2007). It has been postulated that carbonate preservation in western Canada was affected by the depth of the ACD and CCD

(Zonneveld, 2011). The Montney is characterised by thick intervals devoid of preserved carbonate fossils and comparably thin horizons with preserved shell debris. These horizons may represent intervals wherein oceanic acidity was temporarily alleviated and thus shell material was preserved (Zonneveld, 2011). This has strong implications for reservoir quality and the presence of non-dolomite carbonates in the study interval.

Triassic successions (including the Montney Formation) in the Peace River Embayment were deposited on the western margin of the Pangaean Supercontinent. (see Figure 1-4; Davies, 1997; Edwards, *et. al.* 1994). Paleogeographic reconstructions place the Peace River Embayment at approximately 30° North with western Canada rotated from its present position 30° clockwise (Davies, 1997; Golonka *et. al.,* 1994; Golonka and Ford, 2000). During the Triassic, the shelf margin trended approximately north to south through what is now northeastern British Columbia and the rocky mountains (along the Alberta - British Columbia border) (Davies, 1997). Desert and semidesert conditions are thought to have existed inland (Sellwood and Valdes, 2006) with ephemeral river input basinward (Davies 1997). Climate modelling for the Triassic shows temperatures ranging from approximately 20 ℃ (December-January-February) to 40℃ (June-July-August) within the Western Canadian Sedimentary Basin (Sellwood and Valdes, 2006). Evaporite deposits, present in units such as the Charlie Lake Formation, in addition to palyonological analyses (which show an abundance of taeniate bisaccate pollen and polyplicate pollen), indicate an arid coastal environment during Montney deposition (Davies, 1997; Utting *et. al.*, 2005).The Peace River Embayment was subject to onshore cold-water upwelling and north to northeast trade winds, which influenced sedimentation (Golonka et. al., 1994, Davies, 1997). Strong westward winds would have created winter storms off the coast and explain the common storm deposits seen in the Montney Formation (Davies, 1997). Environmental conditions suggest that aeolian transport contributed to Montney sedimentation (Davies, 1997).

Biostratigraphy and the age of the Montney in the study area

The Sulphur Mountain Formation (outcrop equivalent to the Montney Formation) has been dated using conodont biostratigraphy (Orchard and Zonneveld, 2009). The Sulphur Mountain Formation is divided into three members: the Phroso, Meosin Mountain and Vega members (Orchard and Zonneveld, 2009). The Vega Member is equivalent to the Upper Montney Formation (Orchard and Tozer, 1997; Orchard and Zonneveld, 2009; Tozer, 2010; Zonneveld *et. al.,* 2010).

The Late Smithian *mosheri* conodont zone (subdivided into the *milleri* and *phryna* subzones) spans the *Anawasatchites tardus* ammonoid zone. The lower Vega Member occurs in the *phryna* Subzone (Smithian) with the higher parts of the Vega Member assigned to the *milleri* Subzone (Smithian) and the Spathian (Orchard and Zonneveld, 2009). Although many taxa are observed in late Smithian samples, the presence of *Scythogondolella milleri* denotes late Smithian age (Orchard and Zonneveld, 2009). Spathian conodont faunas were observed in the upper portion of the Vega Member (Orchard and Zonneveld, 2009). These include taxa such as *Novispathodus abruptus, Neogondolella* ex. gr. *regalis* and *Triassospathodus* ex. gr. *homeri* (Orchard and Zonneveld, 2009).

Methods

Samples were taken at approximately 10m intervals from within the Montney cored interval of well d-48-A/94-B-9. Thin sections were made of these samples (14 in total). Photomicrographs of all thin sections were taken using a Zeiss Axio Imager A1 transmitted light compound microscope. Magnification was set to 10x to obtain all photomicrographs. Plane-polarized light and cross-polarized light were used. Representative photomicrographs were selected from depths of 1963 m, 1979 m, 1986 m, 1990 m, 1993 m, 2033 m, 2044 m, 2063 m and 2068 m. All thin sections were then coated with carbon for scanning electron microscope (SEM) and electron microprobe (EMP) analysis.

A Zeiss EVO MA 15 scanning electron microscope was used to obtain small-scale backscattered electron images, secondary electron images and elemental maps of selected thin sections. Elements analysed for include: Si, S, Mg, Ca, Fe, Ti, C, K, Na, Al, Ni, Cu, Pb, P and O. Magnification varied depending on the region of interest and ranged from 761x to 2500x. Voltage for these images was set to 20.0 kV. Representative SEM images were chosen from depths of 1963 m, 1986 m, 1990 m, 1993 m, 2041 m, 2052 m and 2063 m.

A Cameca SX100 electron microprobe (equipped with both electron dispersion and wave dispersion spectrometers) was used to obtain large-scale element maps of selected thin sections (5 by 5 mm, 5 by 7 mm, 5 by 15 mm or 10 by 15 mm depending on the size of the thin section). Elements analysed for include: Ca, Fe, K, Na, Si, Al, C, Mg, S and Ti. Voltage for these analysis was set to 20.0 kV. Representative images were selected for display from depths of 1963 m, 1986 m, 1990 m, 1993 m and 2033 m.

Microfacies

Microfacies 1

Microfacies 1 is the most common microfacies in the study interval. It consists of finely laminated quartz (55%), feldspar (potassium feldspar with little albite or anorthite; 20%), dolomite (11%), calcite (7%) pyrite (5%) and mica (2% or less); this microfacies is classified as being a dolomitic lithic arkose. Clay is visible in trace amounts. Grains are angular to sub-angular. Laminae vary in thickness from approximately 0.2 mm to nearly 2 mm or more and alternate between very fine sand (50 to 100 µm) laminae with little/no matrix and matrix supported laminae (see Figure 1-5A and B; matrix grains, 10 µm or less (fine silt); floating grains 20-50 µm (coarse silt)). Laminae are sharp-based, commonly fine upwards (Figure 1-5C) and pinch and swell (Figure 1-5E; suggesting ripples). Additionally, rare foresets are visible topping the coarser laminae (Figure 1-5D). Small-scale erosional features and load casts

(Figure 1-5F) are visible on the millimetre scale at the base of many very fine sand laminae.

Very fine sand laminae are dominated by calcite and quartz, with little to no aluminium or potassium bearing minerals. Matrix-supported / fine to coarse silt laminae contain muscovite and potassium feldspar; these minerals were not observed within the very fine sand laminae. EMP analyses reveal distinctive zonation of the aluminium and potassium content, reflecting the isolation of potassium feldspar and micas to the finer grained laminae (see Figure 1-6C and D). Quartz and calcite appear throughout, but are concentrated in the very fine grained sand laminae. Although concentrations of quartz occur most abundantly within the very fine sand laminae, EMP elemental map of silica content reveals significant levels overall (Figure 1-6B). Dolomite occurs throughout but is less abundant overall than quartz and feldspar (see Figure 1-6A and E for calcium and magnesium EMP maps). Dolomite grains are observed to be eroding in association with calcite (along rims and internally; Figure 1-7), although the abundance of calcite cement is low (Figure 1-8). Smaller (approximately 10 µm across or less), sub-angular to sub-rounded, dolomite and calcite fragments are visible between larger grains. Rutile grains (10-15 µm diameter) are rarely visible with SEM analysis and titanium bearing minerals occur in trace amounts (Figures 1-9, 1-10, 1-11 and 1-12).

Pyrite grains occur throughout (Figures 1-7 through 1-12). They appear large and angular as well as rounded and range in size from approximately 40 µm to less than a micron in diameter. Framboids are also common and are generally small, with occasional large ones in excess of 20 µm. The framboids are commonly within the size range of 5-10 µm, however framboids 2 µm or less are also observed. Although appearing throughout, larger pyrite grains are more abundant in the very fine sand laminae while smaller pyrite nodules are more abundant in the fine to coarse silt faction. In trace amounts, sub-angular phosphate grains are commonly observed with SEM analysis and range in size from a few microns to a few tens of microns in size (the smaller size fraction being more common; Figure 1-7 and 1-8).

Horizontal fractures are visible (Figure 1-5E) and commonly follow the very fine sand-sized, calcite and quartz-dominated beds; they also curve through beds parabolically (Figure 1-6F). These fractures often swell to irregular pores with little/no cementation observed and are discontinuous. Rare intergranular porosity is visible with pores being 1 μm or less in diameter. Visible porosity is less than 1% (excluding fractures) or 2 - 3% (including the fractures). SEM analysis reveals the breakdown of potassium-bearing feldspars and mica into clay (illite). This clay can be seen between the grains of the matrix-supported laminae. Intergranular clay was not observed within the coarser laminae. Trace amounts of kerogen are visible within these clays and appear to be associated with the intergranular porosity. Determination of the kerogen content of the larger cracks was more problematic as the samples were coated in carbon for analysis.

Interpretation:

The correlation between feldspar and mica occurrence and grain size in the Montney Formation was first observed by Davies *et al.* (1997). Our findings here support these previous observations. The high potassium content of finer laminae have implications in regards to petrophysical observations and interpretations (Davies *et. al.,* 1997). The radioactive potassium present in the sediments would deflect the gamma log more than would be expected. In addition, the amount of dense mineral matter, (pyrite and dolomite for example), should have an effect on density logs (Davies *et. al.,* 1997). The low amount of intergranular clay in the coarser grained laminae is likely a result of the lack of feldspar and mica in these laminae. Fractures may be formed due to the dissolution of carbonate grains or as a result of unloading (and therefore would not exist in the subsurface).

Pyrite has been observed in association with end-Devonian shale deposited during the mass extinction (Marynowski *et. al.*, 2012). This pyrite was interpreted as being indicative of euxinic conditions in the photic zone (Marynowski *et. al.*, 2012). Additionally, an overall lack of observed calcium carbonate was attributed to an increase in ocean acidity sourced by volcanic input (Marynowski *et. al.*, 2012). An

increase in marine acidity may explain the low amount of calcium carbonate observed in this microfacies, however, unlike Marynowski *et. al.*, 2012, no volcanic deposits were observed.

The sharp-based nature of the laminae, along with occasional fining upwards beds ripples and basal scouring suggests deposition in association with events such as storm activity or ephemeral river input. These event deposits may be turbiditic in nature and when the litholog is taken into account, possible Bouma sequences Bouma B,C and D) can be identified in association with soft sediment deformation (Figure 1-1).

Classical turbidites (Bouma, 1962) are interpreted to be deposited by low-density turbidity currents (Lowe, 1982; Mulder and Alexander, 2001; Arnott, 2010). However, these deposits can also form from gravity driven concentrated density flows (Mulder and Alexander, 2001). Classical turbidite deposits are commonly normally graded and can be subdivided into five distinct divisions: A though E (Bouma, 1962; Walker, 1992). Division A of a typical Bouma sequence consists of structureless/ massive sand that grades upwards into division B, parallel-laminated sand (Bouma, 1962; Walker, 1992). Division B grades upwards into division C, current rippled sand (Bouma, 1962; Walker, 1992). Parallel laminated silt and mud laminae (division D) overly division C and underlie the final division (E), consisting of mud deposits primarily of pelitic origin (Bouma, 1962; Walker, 1992). The upper portion of division E is hemipelagic and is deposited slowly after the turbidity current event has ended (Bouma, 1962; Walker, 1992).

Turbidite deposition has previously been described occurring within the Montney in the Valhalla-La Glace region by Moslow and Davies, 1997. However these deposits are attributed to mass-wasting along the continental ramp edge which produced a turbidite channel and lobe complex. No such ramp slope break was noted in the region where the samples for this study originated, however more extensive regional study may reveal such an edge. Gravity driven concentrated density flows (such as those produced by slope failure) can produce Bouma C-E or A deposits,

however these deposits tend to differ from surge flows, surge-like flows or quasi-steady currents by a few factors: concentrated density flows are capable of transporting large clasts while true turbidity currents can only transport grains finer than medium sand; The thickness of Bouma division A (relative to the other divisions) can be more substantial in concentrated density flows; Bouma division B may also be less common in concentrated density flows because of high sedimentation rates (Arnott and Hand, 1989; Mulder and Alexander, 2001). As the possible Bouma divisions noted in the litholog are very fine grained, have thin or no Bouma division A and include Bouma division B, deposition *via* a concentrated density flow seems less likely.

The fine-grained nature of these sediments supports an offshore location of deposition, distal to the sediment point source. Pelagic fallout could account for the segregation of mica and feldspar seen within this microfacies. These deposits may have been sourced by ephemeral flooding or storm activity along the coast, which would bring minerals such as detrital dolomite basinward.

Microfacies 2

This microfacies contains the greatest amount of carbonate and is characterised by abundant dolomite (69%). Quartz and potassium feldspar are less abundant (8% quartz, 4% potassium feldspar). EMP analysis shows sodium and aluminium content is low.

Calcite appears as spheres, ranging from 50-130 μm in diameter and consists of coarsely crystalline calcite (see Figure 1-13A, B and D) grains reaching diameters of 50 μm in the larger spheres). Calcite content constitutes approximately 16%. This microfacies is classified as a dolomitic litharenite. Calcite nodules, although scattered throughout, are concentrated within laminae (approximately 1 mm thick) and are thought to be calcispheres or recrystalized ooids (see Figure 1-14A). Coarse silt-sized calcite (averaging 30 μm in diameter) also occurs within vertical fractures which

cross-cut the laminae. All fractures observed are completely filled by coarse grained calcite cement and are often discontinuous (Figure 1-14A, B, C and D).

Quartz occurs in thin laminae which vary in thickness laterally, averaging ~0.2 mm, but reaching up to 1 mm in places (see EMP Si map, Figure 1-14D). Minor amounts of feldspar are present throughout (i.e. not confined to discrete laminae). Laminae fine upwards and in one thin-section are cross-cut by a thick interval of a poorly sorted massive deposit (over 5 mm thick) which displays the same mineralogy and grain size as the underlying laminae with calcispheres but devoid of quartz laminae.

Grain size varies, with a size range of 10 to 50μm (fine to coarse silt), calcite being the coarsest fraction (excluding the nodules). Dissolved, disarticulated bivalve shell fragments are visible, but are diminutive (averaging approximately 150 μm in length) and not visible with the naked eye (Figure 1-13C). These moldic pores are still open, but do contain small groupings of pyrite framboids (less than 4 μm in diameter). Framboids are common throughout and range in size from less than 4 μm to 8 μm. Occasional larger grains of crystalline pyrite are also visible (10-15 μm in diameter). Pyrite constitutes 2-3% in overall abundance. Rare, articulated shell fragments, infilled with coarsely crystalline calcite, also occur. Porosity is low (1-1.5%). Trace amounts of titanium bearing minerals (possibly rutile) were also observed. Above 2044 m depth, the bedding in this facies was observed to become less distinct and shell fragments are very rare. In addition, mica content increases to approximately 1%.

Interpretation:

Microfacies 2, with fining upward laminae cross-cut by a massive deposit suggests deposition in association with events such as storms or ephemeral flooding (as with Microfacies 1). The small grain size suggests deposition below wave base. Comparision with the litholog (Figure 1 and 2) reveals the predominance of planar and ripple lamination and rare bioturbation in association with the occurrence of Microfacies 2. No massive bedding was noted on the litholog. However, because the

massive deposit was only observed in the top portion of one thin section, the nature of the massive deposit is unclear. It may in fact be a thicker lamina, with the "basal scour" being evidence of ripple lamination..

The high carbonate content (shell fragments, calcispheres, etc.) is in contrast to what is observed in Microfacies 1, suggesting a change in sediment sourcing (landward). This could be because of a change in source area (for example, a change in ephemeral river locations) or a change in the environmental conditions in the region of sediment sourcing and deposition. Compared to Microfacies 1, if a change in environmental conditions is considered, the presence of bioclastic debris may signify a change in oxygen levels and therefore a change in acidity. Woods *et. al.* (1999) documented an increase in calcite cements occurring in association with anoxic waters. The precipitation of calcium carbonate was postulated to occur in anoxic environments in association with an increase in bicarbonate input by sulfate reduction in the water column (Kempe, 1990). This increase in bicarbonate causes an increase in pH (Kempe, 1990). The degassing of CO_2 in association with eddy diffusion or upwelling also causes supersaturation to occur with respect to carbonate (Kempe, 1990). The increase in pH would not only facilitate the precipitation of inorganic calcite cements, as observed by Woods *et. al.*, 1999, but would also allow for the preservation of carbonate bioclasts. Woods *et. al.,* 1999 suggested that the precipitation of inorganic carbonate cements they observed occurred where anoxic bottom waters met oxygenated surface waters.

This microfacies is associated with anoxic spikes observed using pyrite analysis (see Discussion) and so supports the involvement of anoxic waters. The presence of bioclasts suggests deposition close to the oxic zone. Deposition of this facies may have then occurred in a shallower environment (proximal offshore or lower shoreface). A decrease in H_2S input may also account for the apparent pH increase.The diminutive size and low abundance of the bioclasts suggests a stressed environment, perhaps low oxygen levels in the photic zone.

The calcite spheres observed are similar to ooids seen by Groves *et. al.* (2005) in late Permian and early Triassic (Greisbachian) sediments. The Triassic oolites observed by Groves *et. al.* (2005) are partly dolomitized, and are recrystalized. These oolites occur with no/rare bioclasts or other allochems and are interpreted as having been deposited in an energetic setting (shoreface or tidally influenced deeper water; Groves *et.al.*, 2005). Because of the facies association between the oolites and other other microbialite deposits in addition to the lack of bioclasts, these oolites were termed "disaster oolites" by the authors (see also, Groves, 2004 and Groves *et. al.*, 2003). The mechanism of ooid formation determined by the authors was inorganic precipitation similar to that observed by Lloyd *et. al.* (1987) on the western interior of the West Caicos Bank. A lack of nutrients in the inner platform of the Caicos Bank resulted in a low occurrence of carbonate-secreting invertebrates (Lloyd *et. al.*, 1987; Groves *et. al.*, 2005). Ooids were found to precipitate inorganically when cabonate-rich water encroached on the beaches, where it was warmed and agitated (Lloyd *et. al.*, 1987; Groves, *et. al.,* 2005). The inorganic precipitation of ooids would be facilitated by the decline of the skeletal carbonate sink because of the end-Permian mass extinction (Groves, 2004; Groves *et. al.,* 2005). Carbonate oversaturation related to anoxia would also contribute to favourable conditions for inorganic ooid formation (Groves, 2004; Groves *et. al.*, 2005).

The layers of calcite spheres observed in Microfacies 2 may have been of similar origin before transport to deeper water *via* a storm event or ephemeral river input. The ooid layers may then signify fluctuating periods of increased anoxia. Further investigation landward may yield more significant ooid deposits.

However, as these calcite spheres lack cores, they may instead be calcispheres, which have been observed in association with anoxic events (Drzewieck and Simo, 1997). These calcispheres were interpreted to be the product of organisms that inhabited an unstable, eutrophic environment (Drzewiecki and Simo, 1997). If they are the product of algal activity, that may be an indication of why there was an increase in anoxia.

Microfacies 3

Microfacies 3 is planar laminated and consists of quartz (60%), dolomite (16%) calcite (10%), feldspar (10%), mica (2%) and pyrite (2%). This Microfacies is classified as a dolomitic feldspathic litharenite. Microfacies 3 is similar to Microfacies 1 in mineral occurrence, the presence of coarser-grained (very fine sand) and finer-grained (fine to coarse silt) laminae and overall grain size (see Figures 1-15A, B, C and D). The finer-grained laminae dominate this microfacies, with beds reaching thicknesses of several millimetres. Fractures were not observed in thin-section in this microfacies.

EMP analysis shows dolomite occurrence is not confined to a specific type of lamina, and is common throughout (see Figure 1-16C and D). Magnesium levels in other minerals, such as feldspars, are elevated only in the finer-grained laminae (Figure 1-16D). Sodium content is low overall, with sodium-bearing minerals (albite) showing no affinity for specific laminae. Potassium content is absent from these coarser grained laminae, however potassium feldspar is visible in the finer laminae. Silica content is very high overall (Figure 1-16A).

SEM analyses reveals calcite cement in the finer-grained laminae and the degradation of dolomite grain rims and cores where calcite is present (Figure 1-17). Coarser-grained calcite (50 to 100 μm) is visible in the coarser-grained laminae. Two dolomite populations were observed: sub-angular to sub-rounded dolomite grains which are interpreted to be detrital in origin; (commonly partially degraded into calcite), and isolated clusters of dolomite rhomboids, which appear to nucleate off of the first dolomite population and thus are interpreted to be authigenic in origin. Titanium-bearing minerals, such as Rutile, although rare, are not associated with a specific type of laminae.Quartz is abundant in the calcite-dominated, coarser-grained laminae (as in Facies 1). Mica (muscovite) is also present in the fine-grained laminae. Pyrite, although scattered throughout, is far more prevalent in the fine-grained laminae. Framboid size averages approximately 4-10 μm, with occasional

framboids as large as 20-25 µm in diameter (see Figure 1-16). In addition, crystalline pyrite is visible, averaging from 15-30 µm in size. Porosity is low in this facies, less than 0.5%, largely due to calcite cementation.

In addition to parallel laminae, climbing ripples occur within the coarser grained laminae (Figure 1-18). Bioturbation is associated with a thick (~5 mm thick) series of coarser grained laminae in which climbing ripples are present. The laminae immediately above, within and below this interval are disturbed and two *Planolites* burrows (approximately 3 mm in diameter) are visible. Recrystalization of calcite has degraded the burrow margins. Possible escape structures are also visible (on the millimetre scale). Bioturbation is absent in remaining laminae.

Interpretation:

Microfacies 3, as with the aforementioned microfacies, consists of event deposits, possibly associated with ephemeral river input or storm activity. The fine-grained nature of the sediment suggests deposition in deeper water. This microfacies occurs in an area of rippled and planar lamination in a coarsening upward sequence in the litholog. Hummocky cross stratification occurs in the litholog a meter up from where Microfacies 3. This may indicate that storm activity is responsible for the event deposits of Microfacies 3. This would also suggest that deposition occurred near storm wave base.

Rapid deposition, by mechanisms such as a turbidity current, accounts for the climbing ripples observed. Climbing ripples occur frequently in fine-grained turbidite deposits (Bouma, 1962; Walker, 1965; Mutti and Normark, 1987; Hodgson *et. al.,* 2006; Jobe *et. al.,* 2012). These structures can occur when fallout of suspended load coincides temporally with bedload transport (Jobe *et. al.* 2012). The formation of climbing ripples is grain-size dependant (Jobe *et. al.* 2012) and occurs most often in very fine to fine-grained sand (Allen, 1968, Jobe *et. al.,* 2012). Unidirectional currents in the lower-flow regime are responsible for bedload transport and when this coincides with rapid fallout of sediment from suspension, migrating ripples are not removed (Allen, 1968; Jobe *et. al.,* 2012). This results in ripples upstream migrating

over ripples downstream (Jobe *et. al.*, 2012). These conditions occur when, over a short distance, the intensity of turbulence within a flow decreases (non-uniform flow; Jobe *et. al.*, 2012). This causes a rapid loss of suspended sediment to occur (Jobe *et. al.*, 2012). A decrease in velocity associated with a change in slope or a loss of confinement can produce non-uniform turbidity currents (Jobe *et. al.*, 2012). The climbing ripples observed in this microfacies may then be associated with non-uniform flow. If a break in slope caused a drop in velocity, this microfacies would have been deposited below the shoreface.

Bioturbation, on a whole, is poorly observed within these thin sections. The bioturbation that is observed seems to correspond with rapid deposition (climbing ripples and convolute bedding) which likely occurred during storm-induced sediment turbididty flows or hyperpycnal flows. So called, "doomed pioneers" were first discussed by Föllmi and Grimm (1990) to explain anomalous trace fossils associated with gravity flow deposits. Organisms are first entrained by a turbulent sedimentation event, such as a storm, and subsequently transported to a new, typically more distal, environment (Föllmi and Grimm, 1990). This new environment, previously uninhabited by the organisms due to environmental stress factors, is colonised by the organisms (Föllmi and Grimm, 1990). However, due to the inhospitable nature of the environment (such as oxygen depletion), colonisation is short lived and the organisms would perish (Föllmi and Grimm, 1990). The presence of *Planolites* in association with climbing ripples in Microfacies 3, and the lack of bioturbation above or below these event deposits, supports this hypothesis. Bioturbation should occur in adjacent laminae as well if the site of deposition was the true habitat of the trace-maker. However, because analysis was conducted using thin sections, the true prevalence of bioturbation in association with this microfacies cannot be properly ascertained. In addition, diagenesis makes ichnological analysis more difficult.

Microfacies 4

Microfacies 4 is poorly sorted (Figure 1-19A and B) and appears massive (Figure 1-19C and D) and mineral content is dominated by dolomite (60%). Calcite

accounts for approximately 20%. Quartz is low in abundance (9%) and feldspar totals approximately 7% (potassium feldspar ~ 4%, albite ~3%). Pyrite occurs throughout (~ 2%), as does mica (2% or less). This microfacies is classified as a dolomitic litharenite.

SEM analyses show dolomite grains eroded by calcite, along rims and internally (Figure 1-20). Rare dolomite rhomboids are also visible (Figure 1-20). Again, these rhomboids are strikingly different in character to the sub-angular to sub-rounded dolomite grains, which are of detrital origin. The grain edges are sharp and little erosion along the grain boundaries has taken place in contrast to the irregular, broken nature of the detrital grain boundaries. All other mineral grains are irregular in shape and angular to sub-rounded. Grain size ranges from 100 μm (very fine sand; rare) to less than 1 μm [with 1-10 μm (very fine silt) being the most common]. Calcite cement is present between grains, as is some clay. Minor kerogen can be seen within intergranular micropores, where calcite cement is absent. Larger, irregular pores (up to 0.25 mm in length) occur and may be the product of calcite dissolution. Overall porosity, however, is less than 1%. Pyrite occurs as framboids (average size of 4-8 μm), and in rare cases coats calcite grains. One such grain is possibly the cross-cut of a recrystallized bivalve shell (see Figure 1-21A and B). It is diamond shaped and approximately 0.2 mm long. No other shell fragments were observed. Larger (1-17 μm) crystalline pyrite was also observed.

EMP analysis show significant levels of calcium (Figure 1-21D) and magnesium (Figure 1-21E) throughout. Silicon levels (Figure 1-21C) are relatively low. This is in contrast to what was observed in Microfacies 1, 3 and 5.

Interpretation:

Microfacies 4 was observed in only one thin section. As with Microfacies 2, the thickness of the massive bed cannot be accurately determined owing to the size limitations of the thin section. On a larger scale of observation, this bed may exhibit grading or other sedimentary structures not visible in the single thin section. The fine-grained nature of the sediment suggests deposition below wave base. The massive

nature could be explained by deposition *via* a turbidity current (Bouma, 1962). The internal degradation of dolomite grains by calcite is interpreted as being dedolomite.

On the litholog this microfacies occurs in a region of relatively high bioturbation including Fugichnia*, Cylindrichnus* and *Phycosiphon*. This may be an example of shallow-marine refugia observed by Zonneveld *et. al.* (2010) and may represent deposition in in the offshore transition to lower shoreface. When compared with the gamma-ray log, this microfacies comes from the boundary region between the Montney and the Doig Formations and so may in fact be from the Doig Formation (see Figure 1-1).

Microfacies 5

Microfacies 5 contains convolute bedding. Both finer grained (fine to coarse silt) and coarser grained (very fine sand) laminae are preserved in some areas (similar grain size to laminae observed in Microfacies 1). Laminae average approximately 2 mm in thickness, however thinner laminae (~0.2 mm) are also observed. Dolomite content is low, approximately 12% and calcite is also observed in low concentrations (8% or less). This microfacies is classified as a dolomitic feldspathic litharenite. Carbonate content is very similar to that seen in Microfacies 1. Quartz is the dominant mineral (~60%). Potassium feldspar is 12% while albite and anorthite content are low (less than 5%). Muscovite is less that 1% while pyrite constitutes approximately 2%. Calcite and dolomite are observed to predominate in coarser-grained laminae, which are undulatory and, in some places, completely obliterated (see Figure 1-22A and B). Coarser-grained laminae also pinch and swell (Figure 1-22C and D). Carbonate content is lower in the finer grained laminae. Quartz, although found throughout, can also be found in these coarser-grained layers. Feldspar and mica are not observed in the coarser laminae and are confined to non-carbonate/low carbonate layers. Pyrite exists throughout, along with titanium bearing minerals such as Rutile. All grains are sub-angular to sub-rounded. In contrast to previous facies, SEM analyses reveal that pyrite occurs as framboids,

ranging in size from 4-7 μm, with rare larger framboids from 10-20 μm in size (Figure 1-23). Some crystalline pyrite is also visible (8-15 μm). Porosity is on the order of 2%, with both intergranular porosity, and dissolved grains (see Figure 1-24A B, C and G). This facies exhibits the highest micro-porosity. Kerogen can be observed in the micropores and is the most abundant in this microfacies, although the true kerogen content of the larger pores is difficult to determine because of the carbon coating. Bioturbation is visible in association with the convoluted bedding (Figure 1-24A, D, E and F); the trace fossil *Lingulichnus* is present (Figure 1-25). In addition, a single rip-up clast was observed.

Interpretation:

The high micro-porosity observed in this microfacies is a function of low carbonate cementation and low clay content. This allowed intergranular spaces to remain open. Microfacies 5, which exhibits highly convoluted bedding and a rip-up clast, was deposited during rapid deposition. Similar laminae patterns are visible in Microfacies 1 (excluding the intense bioturbation/convolute bedding), suggesting this microfacies was deposited in a basinal setting similar to that of Microfacies 1. This microfacies could have been deposited during an event such as a storm.

Lingulichnus has been observed in association with storm-generated sandstone beds in the Triassic Toad and Liard formations in northeastern British Columbia (Zonneveld and Greene, 2010). In situ occurrences of this trace fossil often occur in proximal offshore through lower shoreface tempestites (Zonneveld *et. al.,* 2007).The small proportion of *Lingulichnus* seen in these sandstone beds was interpreted to be a result of the patchiness of infaunal communities (pre and post-event) and could explain the rarity of *Lingulichnus* seen in thin section (Zonneveld and Greene, 2010). Lingulide brachiopods are capable of surviving many of the stresses associated with storms, such as storm-induced burial, exhumation, transport and reestablishment (Zonneveld and Greene, 2010). The *Lingulichnus* seen in this microfacies may be the result of storm-induced transport *via* a turbidity current, which would be consistent with the convolute bedding observed. The rarity of trace fossils

seen within these thin sections, however, could merely be a reflection of the overall lack of organisms after the end-Permian mass extinction (Zonneveld et. al., 2010) and represents one of the problems associated with interpreting Early Triassic aged strata such as the Montney.

Discussion

Turbidite deposition

The planar laminae, ripples, climbing ripples and massive bedding observed can be explained by turbidic deposition (Bouma, 1962). Although determining Bouma sequences in thin section is problematic, the litholog shows possible Bouma B, C and D deposits. Events such as storms and hyperpycnal flows are possible sources of turbidic deposition (Mulder and Alexander, 2001). The influence of storms on Montney sedimentation has been documented in work such as Davies (1997) and Moslow and Davies (1997).

Fluid turbulence is the main transport mechanism for particles in a turbidity current (Middleton and Hampton, 1973; Mulder and Alexander, 2001). Bagnold, 1962, defined the limit for particle support by turbulent flow as being 9% sediment concentration by volume (Mulder and Alexander, 2001; Arnott, 2010). This upper limit defines turbidity currents (*senso stricto*; Mulder and Alexander, 2001). Broader definitions exist to explain turbidity currents, such as that used by Piper and Normark, (2009). They define a turbidity current is a current of sediment and water which behaves as a Newtonian fluid (at least in part) and is denser than the surrounding environment. This paper will be using the classification scheme proposed by Mulder and Alexander, 2001, where turbidity currents lie on a continuum with concentrated density flows but are still defined as currents whose main process of sediment transport is fluid turbulence (using Bagnolds limit). This definition excludes the terms high density or high concentration (i.e. the high-density turbidites of Lowe, 1982) as, in these cases, fluid turbulence would not be the dominant method of sediment

transport (Mulder and Alexander, 2001). With high sediment concentration, additional mechanisms play a more important role in suspending sediment such as buoyancy and dispersive pressure (Arnott, 2010).

Using flow behaviour as the distinguishing criterion, turbidity flows have been subdivided into three catagories: surge flows, surge-like flows and quasi-steady currents (Mulder and Alexander, 2001). Surges are uncommon and occur when the body of an accelerating flow overtakes the head, resulting in a flow with little to no tail (Mulder and Alexander, 2001). The flow in this case is non-uniform and short in duration (Mulder and Alexander, 2001). Surge-like turbidity flows may develop a body and also occur over a short period of time (Mulder and Alexander, 2001). Flows of this nature can be generated by storm activity which causes sediment on the shelf to be suspended in clouds which later collapse (Mulder and Alexander, 2001). These flows can also be produced when a higher density flow undergoes transformation via acceleration and erosion (Mulder and Alexander, 2001). Particles transported by surges and surge-like flows are usually sand size or smaller and, because of the short duration of flow and the relatively low sediment concentration, thin fine beds or laminae often result unless the flow size is very large (Mulder and Alexander, 2001). Deposits consisting of well developed Bouma divisions b-d can be produced by longer duration surge-like flows where the body and tail have more time to develop (Mulder and Alexander, 2001). Thus, the thinly bedded, fine grained Bouma divisions observed in the microfacies (in conjunction with the litholog) may have ultimately been sourced by surge or surge-like flows generated by storm activity along the coast.

Turbidites may also be generated by hyperpycnal currents (Mulder and Alexander, 2001; Mulder et. al. 2003; Piper and Normark, 2009). These currents (termed quasi-steady hyperpycnal turbidity currents by Mulder and Alexander, 2001) occur when fluid entering a marine basin or lake from a river mouth is denser than the surrounding water, resulting in a plunging underflow (Alexander and Mulder, 2002; Mulder et. al. 2003). These currents can transport particles finer than medium sand large distances into the deep-sea (Mulder, et. al. 2003). The sediment density

required for a hyperpycnal current to develop in the marine realm ranges from 36 to 44 kg/m3, depending on salinity and temperature (Mulder and Syvitski, 1995; Alexander and Mulder, 2002; Mulder *et. al.* 2003). The term quasi-steady is used to describe these currents, differentiating them from surges and surge-like flows, because the flow duration is substantially longer (days to weeks versus hours for surges and surge-like flows) and the body of the current is the dominant depositional volume with the head having an insignificant role in the resulting deposits (Mulder and Alexander, 2001). Few rivers carry enough suspended sediment to produce hyperpycnal flows year round (Mulder *et. al.* 2003). Instead, most hyperpycnal currents are triggered by river flooding which can be caused by storms, excessive rainfall or monsoons (Mulder and Alexander, 2001). Flash floods, such as those that can occur in hot arid environments, can be caused by heavy rains (such as with the Djer river in North Africa) or triggered by hurricanes and cyclones (such as in Mexico) and occur where water input is intermittent but large in volume (Mulder *et. al.,* 2003). In this case, months or years may pass between flood events (Mulder, *et. al.,* 2003). Because flow velocity can increase so quickly during the waxing phase of a flash flood, most initial deposits become reworked and thus the typical hyperpycnite pattern (inversely graded beds followed by a Bouma sequence) may not be present (Mulder and Alexander, 2001). In this case, the resulting Bouma deposits can be misinterpreted as having been generated by a surge or surge-like flow (Mulder and Alexander, 2001).

As the Montney was deposited during an arid climate, with mega-monsoons occurring in the northern hemisphere (Preto *et. al.,* 2010), it is possible that the event beds observed in these Microfacies may have been the result of hyperpycnal flows during flash-flood events. The general lack of freshwater fossils typically seen in hyperpycnal deposits (Mulder and Alexander, 2001) may be attributed to the general lack of fossils during this time (in association with the end-Permian mass extinction). As winter storms may have been common along the coast during Montney deposition (Davies *et. al.,*1997), a combination of storm-induced surge-like flows and flood-

induced hyperpycnal flows may ultimately be the origin of these Montney deposits. Storm activity coincides with the trace fossils observed (doomed pioneers).

Pyrite Deposition

Pyrite framboids or iron monosulfide microcryst aggregates form at the redox boundary in the iron-reducing zone (Bond and Wignall, 2010). Crystalline and amorphous pyrite grains develop below this region in the anoxic sulfate-reducing zone (Wilkin *et. al.,*1996; Wilkin and Barnes, 1997; Bond and Wignall, 2010). Framboids can also develop in the water column, providing bottom waters are euxinic with free H_2S in the water column (Wilkin *et. al.,* 1996; Bond and Wignall, 2010). Under these conditions, framboids reach diameters of 5-6µm or less, ceasing to grow once they sink beneath the iron-reducing zone (Bond and Wignall, 2010). In weakly oxygenated bottom waters (dysoxic conditions), framboids form within the top layers of sediment and, because size is determined by the availability of reactants, framboid size is variable and larger sizes are more common (Wilkin *et. al.,* 1996; Bond and Wignall, 2010). In this environment, specific variability in pyrite formation allows framboids to be used to determine redox conditions (Bond and Wignall, 2010).

Five redox conditions, as determined by pyrite analysis, were determined by Bond and Wignall (2010). Euxinic conditions produce abundant, small framboids with a narrow size range (3-5µm) with sediments that are typically finely laminated. Anoxic conditions are evidenced by abundant, small framboids (4-6µm) with occasional larger ones in finely laminated sediments. In both cases, framboids are the dominant pyrite form with very little crystalline pyrite present. Lower dysoxic conditions with weakly oxygenated bottom waters produce framboids with an average size of 6-10µm with some larger framboids and crystalline pyrite. Rare bioturbation occurs under these conditions (Bond and Wignall, 2010). Upper dysoxic conditions, where there is a partial oxygen restriction in bottom waters, leads to the development of rare to moderately common framboids with a broad size range (with a small proportion less that 5 µm in size). In this environment, the majority of pyrite forms as

crystals and sediments are more likely to exhibit bioturbation (Bond and Wignall, 2010). In oxic waters with no oxygen restrictions, no framboids form and pyrite crystals are rare; sediments are bioturbated and massive (Bond and Wignall, 2010)

Microfacies 3 and 5 contain framboids, crystalline pyrite, and bioturbation, and are classified as being deposited in a lower dysoxic environment. Due to the amount of crystalline pyrite observed in Microfacies 4, it could be classified as lower dysoxic, however bioturbation is absent and the average framboid size is small, so environmental conditions were likely closer to being anoxic. Microfacies 1 and 2, because of the larger framboid size and abundance of crystalline pyrite, was likely deposited under lower dysoxic conditions. However, bioturbation was not observed which suggests there was very little or no oxygen in bottom waters for long periods of time. These findings agree with those of Bond and Wignall (2010) who, after conducting a pyrite study of multiple Permian/Triassic sites, found that samples (Griesbachian age) taken from Paris Canyon of Idaho were deposited under dysoxic conditions. These samples were originally deposited along the western margin of Pangea in the Panthalassa ocean several hundred kilometres south of the Peace River Basin (Bond and Wignall, 2010).

Dolomite Deposition

Although an aeolian source has been postulated to be a major source of Montney sedimentation (Davies 1997), Pilkey (1966) found only 10% detrital dolomite within bottom sediments of the Gulfwhich was attributed to aeolian deposition. The contribution of wind-blown dolomite to bottom sediments is most likely minor (Warren, 2000). Thus, an additional source for the Montney detrital dolomite accumulations is needed, such as precipitation *via* sulphate-reducing bacteria. Dolomite formation has been connected to periods of low oceanic oxygen levels (Burns *et. al.*, 2000; Krause *et. al.*, 2012) during which regular aerobic processes were decreased resulting in more organic matter for anaerobic breakdown processes such as sulfate reduction (Jørgensen, 1982; Krause *et. al.*, 2012). Further work is required, however, to

investigate the role of sulphate-reducing bacteria in producing the detrital dolomite observed. Whether diagnostic features of bacterial involvement (such as dumb-bell morphology or the presence of micro-spheres on the surface of the dolomite crystals; Warren, 2000) would be preserved after sediment transport is questionable. However, negative $\delta^{13}C$ values of the dolomites would support a bacterial interpretation (Warren, 2000).

The formation of dolomite under modern surface conditions is impeded by kinetic factors (Machel and Mountjoy; 1987, Warren, 2000; Van Lith *et. al.*, 2003; Wright and Wacey, 2005; Krause *et. al.* 2012) such as the strength of the Mg^{2+} hydration shell (Lippmann, 1973) and the presence of sulphate ions (Baker and Kastner, 1981). Microbial activity, specifically the involvement of sulphate-reducing bacteria, has been shown to circumvent these kinetic barriers by removing sulphate, increasing carbonate alkalinity and raising the pH (Vasconcelos *et. al.*, 1995; Vasconcelos and McKenzie, 1997; van Lith *et. al.*, 2003; Krause *et. al.*, 2012). Removal of sulphate also raises the availability of magnesium ions as sulphate in seawater occurs as a magnesium-sulphate pair (Vasconcelos and McKenzie, 1997; Warthmann *et. al.*, 2000; van Lith *et. al.*, 2003; Wright and Wacey, 2005). Carbonate alkalinity and pH are increased as a function of the oxidization of cyanobacteria and organic matter by sulphate-reducing bacteria in addition to other microbes (Wright and Wacey, 2005).

Dolomite produced by sulphate-reducing bacteria has most notably been observed at Lagoa Vermelha, a hypersaline lagoon in Brazil (Vasconcelos *et. al.*, 1995; Vasconcelos and McKenzie, 1997; Warren, 2000). A model for dolomite formation *via* bacterial sulphate-reduction was developed based on the Lagoa Vermelha findings by Vasconcelos and McKenzie (1997). In this model, high-Mg calcite and Ca-dolomite is precipitated within an anoxic turbid layer at the sediment water interface. The consumption of photosynthetically produced organic matter within this anoxic layer by sulphate-reducing bacteria was shown to directly result in the precipitation of dolomite. The authors observed that mineral nucleation occurs on the surface of the bacteria, where the microenvironment has been altered during

metabolic processes. Modern laboratory experiments have supported this (e.g. Warthmann *et. al.*, 2000). Bacterial involvement was observed to continue as the dolomite crystals underwent early diagenesis, resulting in an increase in the order of the crystal structure.

Crystal morphologies resulting from the involvement of sulphate-reducing bacteria vary. Smooth euhedral dolomite crystals were observed at Lagoa Vermelha after an "aging process" during shallow burial; dumbbell-shaped crystals have commonly been observed in laboratory experiments (van Lith *et. al.*, 2003) and spheroidal grains have been noted by authors such as Wright and Wacey (2005). Other crystal morphologies, such as twisted planar layering, have also been observed (van Lith *et. al.*, 2003).

Experiments have shown that sulphate-reducing bacteria can nucleate dolomite under anoxic conditions at surface temperatures. However, until recently this phenomenon has only been documented occurring under hypersaline conditions. Work by Krause *et. al.* (2012) has challenged this and has shown that dolomite can be produced by sulphate-reducing bacteria under modern seawater salinity and temperature in anoxic conditions. Using the sulphate-reducing bacterium *Desulfobulbus mediterraneus,* ordered Mg-rich dolomite was precipitated in a synthetic anaerobic substrate. The molar ratio of Mg^{2+} and Ca^{2+} was set to reflect modern seawater salinity (molar ratio of 5). Spheroidal dolomite particles ~2-3 μm in diameter were observed to have formed in association with the bacterium after 14 days. Dolomite was observed to have formed by day 3, however these crystals were incredibly small (nanometric scale). Whether the dolomite crystals would have continued to grow larger is a matter of speculation as the study conclude after 14 days. However, the work of Krause *et. al.* (2012) does demonstrate that Mg-rich dolomite can form under anoxic marine conditions with microbial mediation. This expands the microbial dolomite model of Vasconcelos and McKenzie (1997) to include marine settings (Krause *et. al.*, 2012).

Comparison with Litholog and Gamma-ray log

Figure 1-1 shows the occurrence of each microfacies in relation to the litholog (courtesy of J.P. Zonneveld) and the gamma-ray log. In general, the observations made using thin-sections agree with the big picture provided by the litholog. Microfacies 1 occurs where there is generally planar and rippled laminae and no trace fossils (the red lines rarely intersect symbols of observed bioturbation). On a larger scale (in this figure the entire litholog was compressed to a single page), this agreement is more pronounced. Microfacies 1 is found within beds of the litholog that are on the boundary between coarse silt and very fine sand.

In regards to Microfacies 3, it is indistinguishable from Microfacies 1 on the litholog as the small fractures were not observed. Bioturbation observed in thin section, such as *Planolites,* does correlate with the bioturbation observed within the litholog. However, *Lingulichnus* (seen in Microfacies 5) does not occur within the litholog.

Microfacies 2, which contained no trace fossils but diminutive bivalve fragments, occurs in regions of moderate bioturbation where no fossil content was observed within the litholog. This may reflect the difficulty in observing diminutive fossil content with the naked eye and thus suggests that fossil content within the Montney may be more prevalent but difficult to observe. The ooids/calcispheres also would be difficult to observe without magnification.

When observed in context of the litholog and gamma-ray log, Microfacies 4 seems likely to be part of the Doig Formation as it occurs in what could be the Doig Phosphate Zone. This would explain why this Microfacies was observed in only a single sample. The presence of some possible bioclastic debris agrees with what was observed in the litholog. The planar laminae indicated on the litholog suggest that, at a larger scale, the massive nature of the bedding observed in thin-section may simply be thicker planar laminae.

Although convolute bedding does occur in the litholog, it does not coincide with that seen in Microfacies 5. Pyrite was found to be prevalent in all microfacies, but is not observed consistently within the litholog. The small size of the pyrite makes it difficult to observe.

The overall alternation of rippled beds and planar laminae, in addition to the convoluted bedding depicted in the litholog supports the idea of these deposits consisting of event beds. In regards to the gamma-ray log, a trend is observable; Microfacies 1 often occurs in association with large gamma-spikes and this may correspond to higher amounts of feldspar observed.

Diagenetic History and Reservoir Potential

Deposition of detrital dolomite, quartz, feldspar, calcite, mica and organics occurred through sediment gravity flows likely transported into the marine realm by ephemeral flooding due to storm activity. Because deposition occurred below the carbonate compensation depth (ccd), all primary calcite was dissolved (as evidenced by the moldic porosity seen). This is made possible by the elevation of the ccd to shallow marine settings because of changes in ocean acidity (Woods *et. al.*, 1999; Beauchamp and Grasby, 2012). An increase in ocean acidity during the end-Permian mass extinction has been postulated to have caused the shallow-water carbonate dissolution observed in South China (Payne *et. al.*, 2010; Beauchamp and Grasby, 2012). The character of the pyrite observed within Montney samples suggests deposition in a dominantly dysoxic environment and shallow burial within the iron redox zone (Bond and Wignall, 2010). Low oxygen levels contributed to the preservation of organic matter. After burial, calcite dissolution, pyrite formation and diagenesis began, the dolomite began to destabilise and revert to calcite, forming dedolomite. In addition, calcium-rich fluids began to deposit calcite within the pore spaces. In the case of Microfacies 4, dedolomitization may have been facilitated by subaerial exposure (evidenced by a *Glossifungites* surface recorded in the litholog; Vandeginste and John, 2012). Alternatively, the dedolomite observed could have

resulted from the involvement of calcium-sulphate-rich fluids (Vandeginste and John, 2012). Minor interaction with brine fluids and a change in diagenetic conditions may have also contributed to the small amount of diagenetic dolomite observed. Finally, with increased heat and pressure, kerogen trapped within the pore spaces began to produce gas, making the Montney Formation self-sourcing.

Reservoir potential of the Montney Formation is influenced by numerous factors. Preservation of the organic matter due to low oxygen levels allowed for the kerogen to be preserved. Rapid passage through the sulphate reduction zone prevented the organic matter from being consumed by sulphate reducing bacteria, which also prevented the pores from being occluded by pyrite deposition. This rapid passage could be explained by ephemeral flooding partnered with a high frequency/ high severity of seasonal storm activity which would produce turbidity currents. Calcite cementation was extensive, but not complete, prohibited by the presence of organics. In addition, dedolomitization created porosity, adding to the resource potential of the Montney Formation.

Conclusions

This petrographic study, SEM and EMP analysis of 14 Montney samples has allowed for the identification of five distinct microfacies. Thin section analysis revealed that sub-mature grains predominate in all five microfacies. Banding was seen in most microfacies, consisting of finer-grained (medium silt) dark bands (1mm-0.5 cm) and light, coarser grained (very fine sand) bands (1-3 mm). Feldspar and mica were found to be excluded from the coarse grained laminae. Some deposits, in contrast, were observed to be massive. Dissolved bioclastic material, seen in Microfacies 2, indicates initial deposition occurred below the calcium carbonate compensation depth. Sedimentary structures seen within these microfacies (ie. Bouma sequences and soft sediment deformation) suggest deposition by multiple turbidity flows (from storms or ephemeral river input) as opposed to aeolian sourcing. Bioturbation, although rare, was observed in two thin-sections and is interpreted to

represent organisms transported with the turbidity current and were unsuccessful at colonising the oxygen poor environment.

The analyses of these microfacies reveals a complex depositional history involving detrital quartz, dolomite, feldspar, mica and bioclastic debris deposited by turbidity currents. Pyrite analysis reveals deposition in a dysoxic environment while the preservation of kerogen within micro-pores suggests a rapid transition through the sulphate reduction zone. Later calcite cementation and dedolomitization has both occluded pores (infilled by calcite cement) and created them (additional micro-pores formed during dedolomitization). This has led to variable porosity, however high intergranular porosity can be seen in some thin sections. The preserved kerogen within these pores has allowed for the Montney Formation to be self-sourcing.

The resource potential of the local Montney Formation is influenced by a number of critical factors, which are: (1) deposition in a low oxygen setting allowed for kerogen to be preserved; (2) pyrite precipitation was interrupted by rapid transition through the sulphate reduction zone, also preventing the decay of organic matter by sulphate reduction; (3) later calcite cementation did not completely occlude all pores (likely influenced by the presence of organic matter); and (4) the process of dedolomitization, evidenced by degraded and eroded dolomite grains and cores, generated additional porosity.

	Microfacies 1	Microfacies 2	Microfacies 3	Microfacies 4	Microfacies 5
Rock Classification	dolomitic lithic arkos	dolomitic litharenite	dolomitic feldspathic litharenite	dolomitic litharenite	dolomitic feldspathic litharenite
Mineral Composition	Quartz 55%	Dolomite 69%	Quartz 60%	Dolomite 60%	Quartz 60%
	Feldspar 20%	Calcite 16%	Dolomite 16%	Calcite 20%	Feldspar 17%
	Dolomite 11%	Quartz 8%	Calcite 10%	Quartz 9%	Dolomite 12%
	Calcite 7%	Feldspar 4%	Feldspar 10%	Feldspar 7%	Calcite 8%
	Pyrite 5%	Pyrite 2%	Mica 2%	Pyrite 2%	Pyrite 2%
	Mica 2%	Mica 1%	Pyrite 2%	Mica 2%	Mica 1%
Porosity	2-3%	1%	less than 0.5%	1%	2%
Sedimentary Features	fining upward laminae, ripples	fining upward laminae	parallel laminations	massive	convolute bedding
		massive deposit	climbing ripples		parallel laminations
		calcispheres/ooids			
Fossil Content	none observed	brachiopod shells	*Planolites*	rare	*Lingulichnus*
Fracture	horizontal and parabolic	vertical, infilled	none observed	none observed	none observed
Interpretation	event deposits; offshore	event deposits; proximal	event deposits; near storm	offshore transition-lower	event deposits; offshore
		offshore to lower shoreface	wave base	shoreface	
Formation	Montney	Montney	Montney	Doig	Montney

Table 1-1 Summary table of the five Microfacies observed in the Upper Montney. Microfacies 1, 3 and 5 have very similar mineral content and sedimentary features but differ in fracture and fossil content. The porosity of Microfacies 3 is also much lower than that observed in Microfacies 1 and 5. Microfacies 2 and 4 have similar mineral content but differ in fossil content.
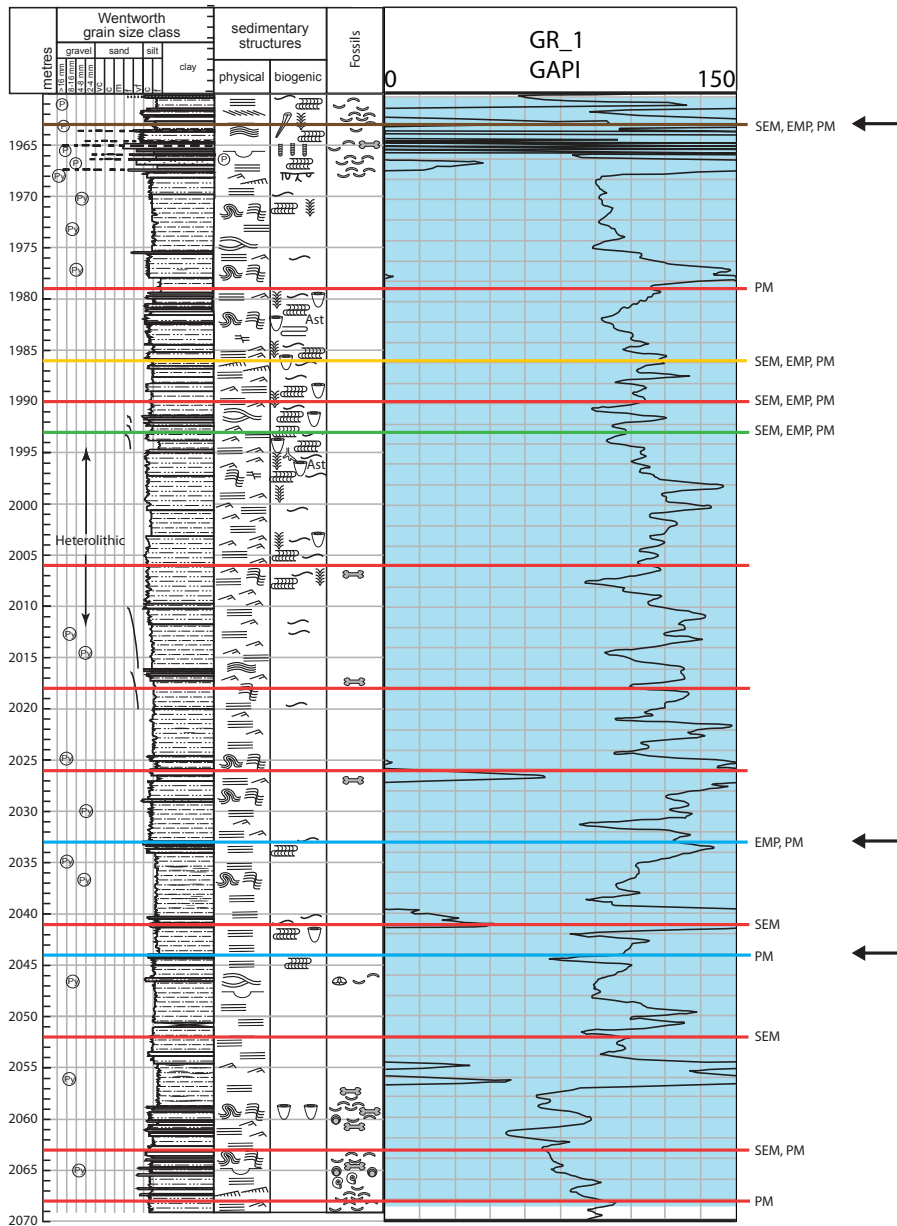
Figure 1-1 Composite figure depicting the litholog (courtesy of J.P. Zonneveld), Gamma Ray log and the occurrence of each microfacies within the Upper Montney of well d-48-A/94-B-9. The applicable area of the Gamma Ray log is highlighted in blue. Microfacies 1 is denoted by red lines; Microfacies 2 is denoted by blue lines; Microfacies 3 is denoted by a green line; Microfacies 4 is denoted by a brown line and Microfacies 5 is denoted by a yellow line. Note that Microfacies 3, 4 and 5 were only observed once. Additionally, as Microfacies 4 occurs near the boundary between the Montney and the Doig formations, this microfacies may in fact be from the Doig Formation. Three arrows on the right hand side represent anoxia spikes during deposition as determined by pyrite analysis. See Figure 2 for a complete legend.

Legend

Py	Pyrite	——	Microfacies 1
P	Phosphate	——	Microfacies 2
	Scour	——	Microfacies 3
	Wavy bedding	——	Microfacies 4
	Planar bedding	——	Microfacies 5
	Low angle cross-stratification	SEM	SEM analysis available
	Ripple Laminae (bidirectional/starved)	EMP	EMP analysis available
	Soft sediment deformation	PM	Photomicrograph available
	Hummocky cross-stratification	←	Anoxia spike
	Soft sediment faulting		
	Glossifungites		
	Conichnus/Bergaueria		
	Planolites		
	Phycosiphon/Anconichnus		
	Helminthopsis/Helminthoida		
	Teichichnus		
	Fugichnia		
	Cylindrichnus		
Ast	*Asterosoma*		
	Thalassinoides/Camborygma		
	Vertebrate skeletal elements		
	Terebratulid Brachiopod		
	Bioclastic debris		
	Acrotretid brachiopod		
	Ammonoid		

Figure 1-2 Legend corresponding to Figure 1.
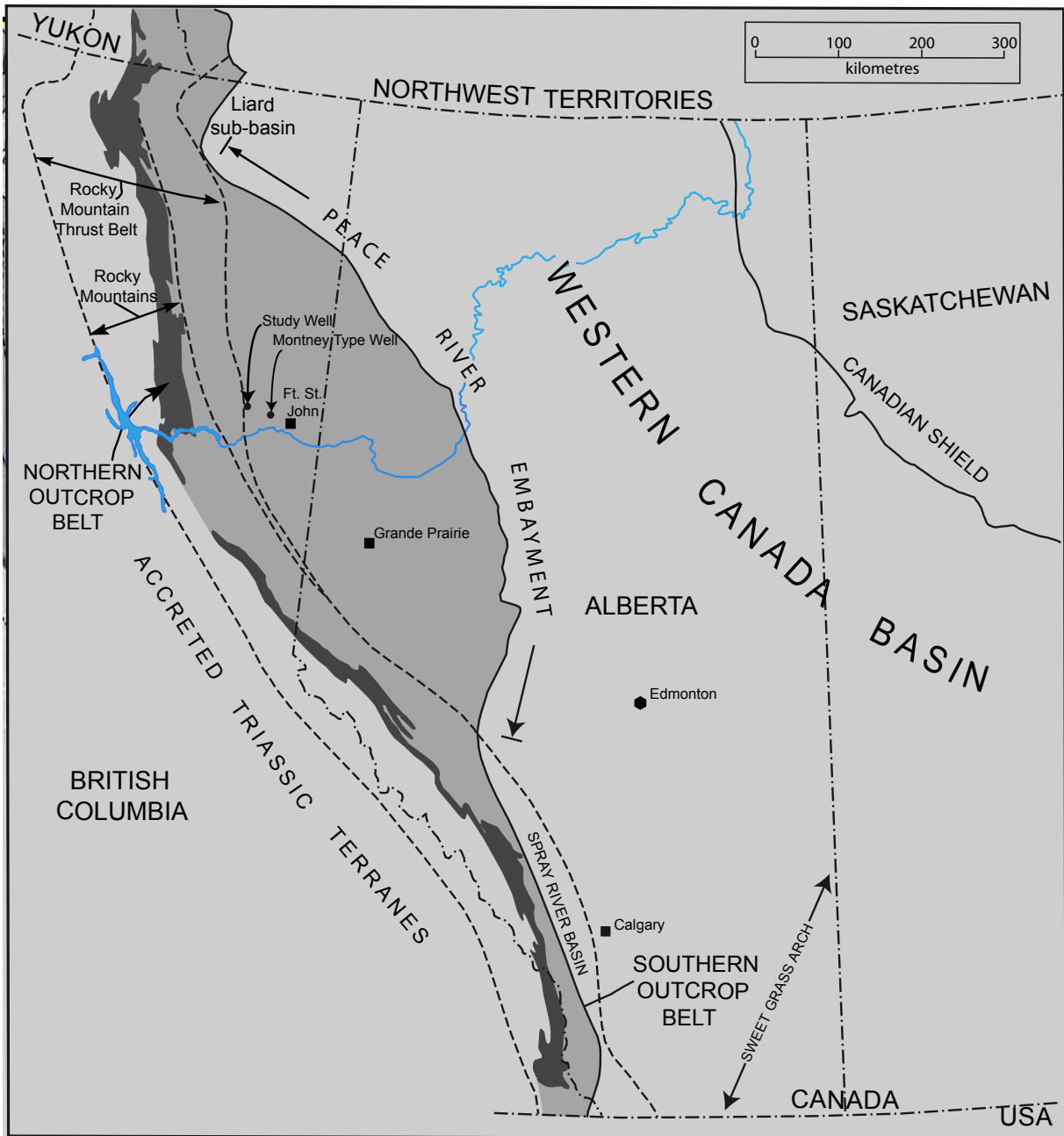
Figure 1-3 Map of the Peace River Embayment during the time of Montney deposition modeled after Davies, 1997. The location of the sample well used in this study as well as the location of the Montney Type Well are denoted by two circles. The grey regions represent the continental shelf during the time of deposition.
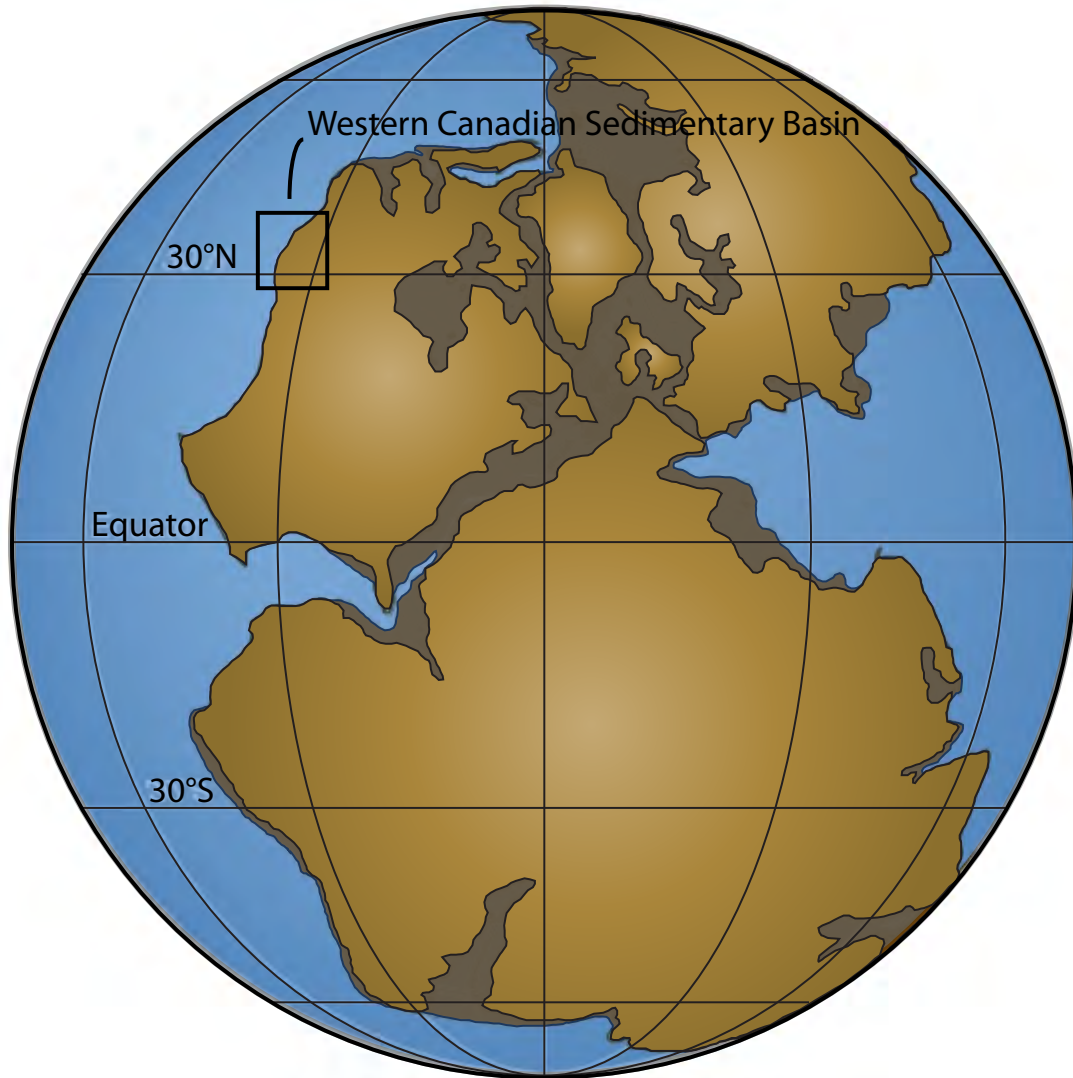
Middle Triassic (240 Ma)

Figure 1-4 Paleogeographic reconstruction of Pangea during the Triassic, based on the work of Domeier *et. al.*, 2012. The dark grey regions represent present-day continental crust that is submerged and extends to the continent-ocean boundary. Longitude is divided into 30° intervals.
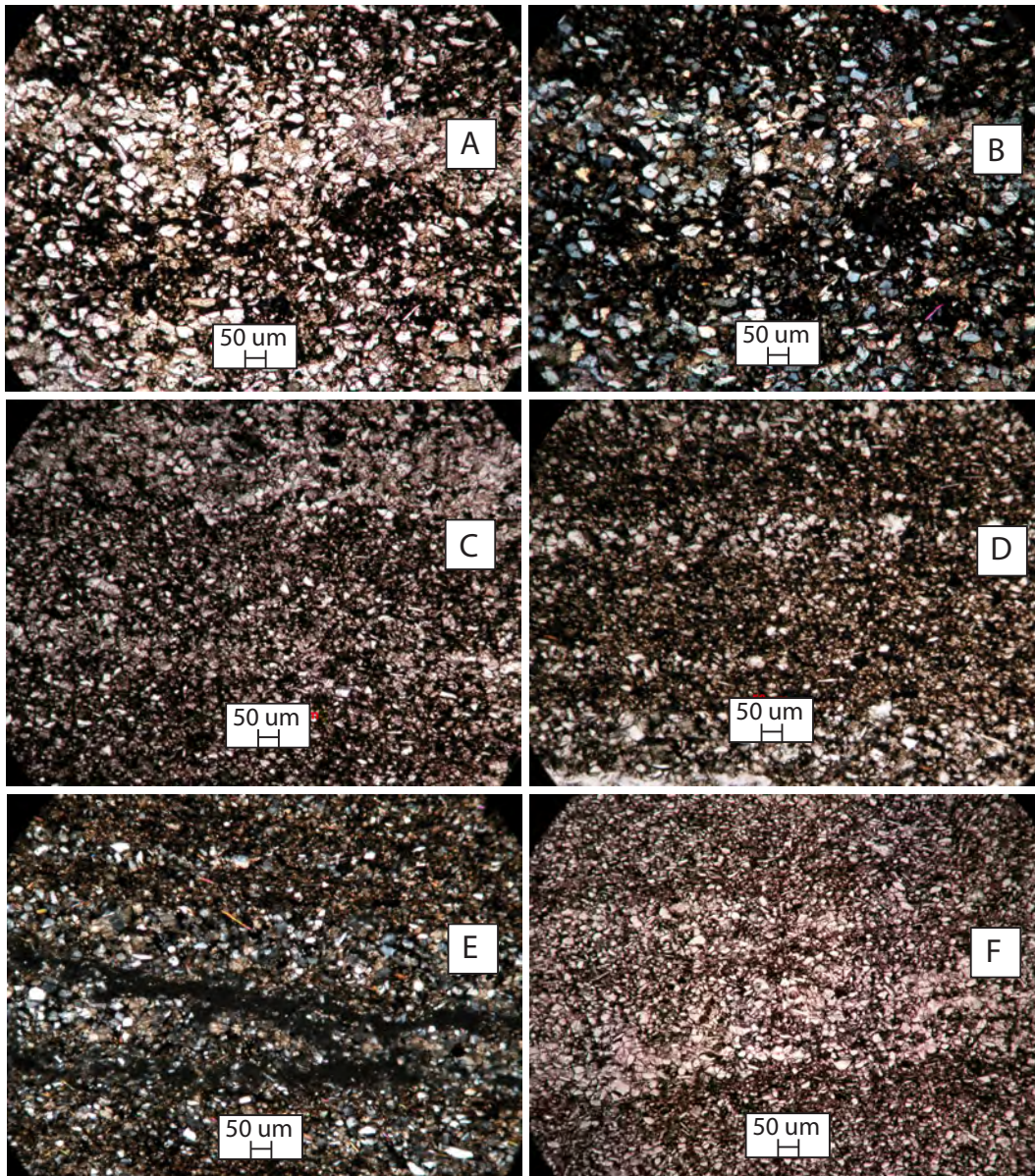
Figure 1-5 Thin section photomicrographs showing the coarse and fine-grained laminae observed in Microfacies 1. Note the dark colour of the fine-grained laminae is due to the small grain size. **A** was taken under plane polarized light and shows the fining upwards of the laminae at 2063 m depth. **B** shows the same region under cross polarized light. Note the dominance of silicate minerals such as Quartz and Feldspar. The fining upwards trend is also observable in **C**, taken under plane polarized light from 1979 m depth. The pinching and swelling nature of the coarse-grained laminae is observable in **D**, taken under plane polarized light from 1990 m depth. On a larger scale, this pinching and swelling is observed to form foresets. The horizontal, parabolic fractures are visible in **E**, taken under crossed polarized light from 1990 m depth. The fractures tend to occur in association with the coarser laminae. Erosional features are observable at the base of the coarse-grained laminae in **F** (note the undulatory nature), taken from 2068 m depth. The coarse-grained laminae often are sharp based. This photomicrograph was taken under plane polarized light. All photomicrographs are from samples taken from well d-48-A/94-b-9.
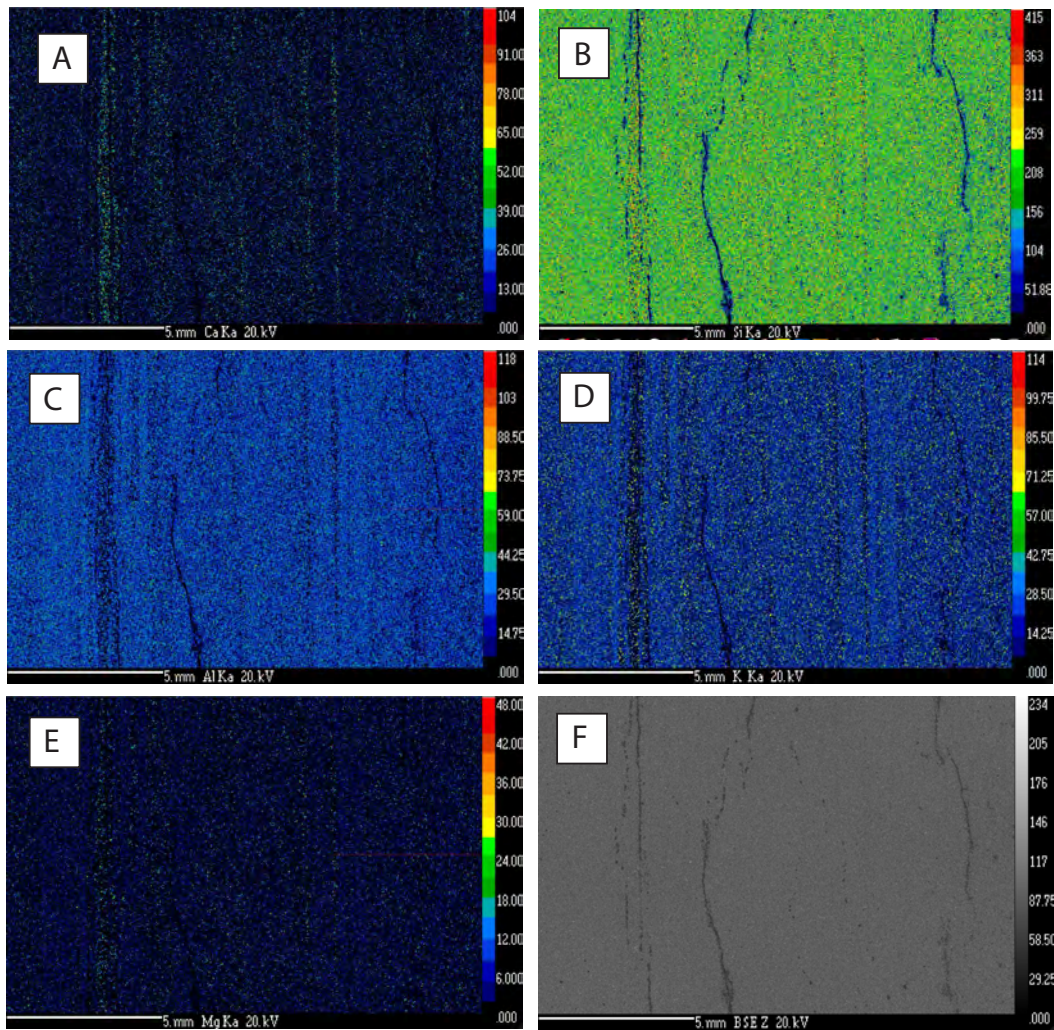
Figure 1-6 Electron microprobe element maps (false colour images) showing the concentration of calcium (A), silicon (B), alluminium (C), potassium (D) and magnesium (E). The backscattered electron image is visible in F. Displayed colour scales represent the relative abundance of a mineral within the sample. Brightly coloured (towards the red end of the spectrum) regions indicate a high concentration of the specified element. Bright regions which overlap are interpreted as representing areas of mineral occurrence (for example dolomite occurrence can be seen by comparing the elemental maps of calcium and magnesium). The concentration of Quartz and Calcite in the coarser laminae as well as the segregation of feldspars and mica can be seen by observing the concentrations of the elements calcium, silicon, potassium and alluminium. The grey scale in the backscattered electron image (F) can be interpreted as representing relative density (increasing density corresponds to a lightening of the grey colour). Note the fractures observed (dark grey in the backscattered electron image). All images are from a sample taken from well d-48-A/94-b-9 at 1990 m depth and are representative of Microfacies 1.
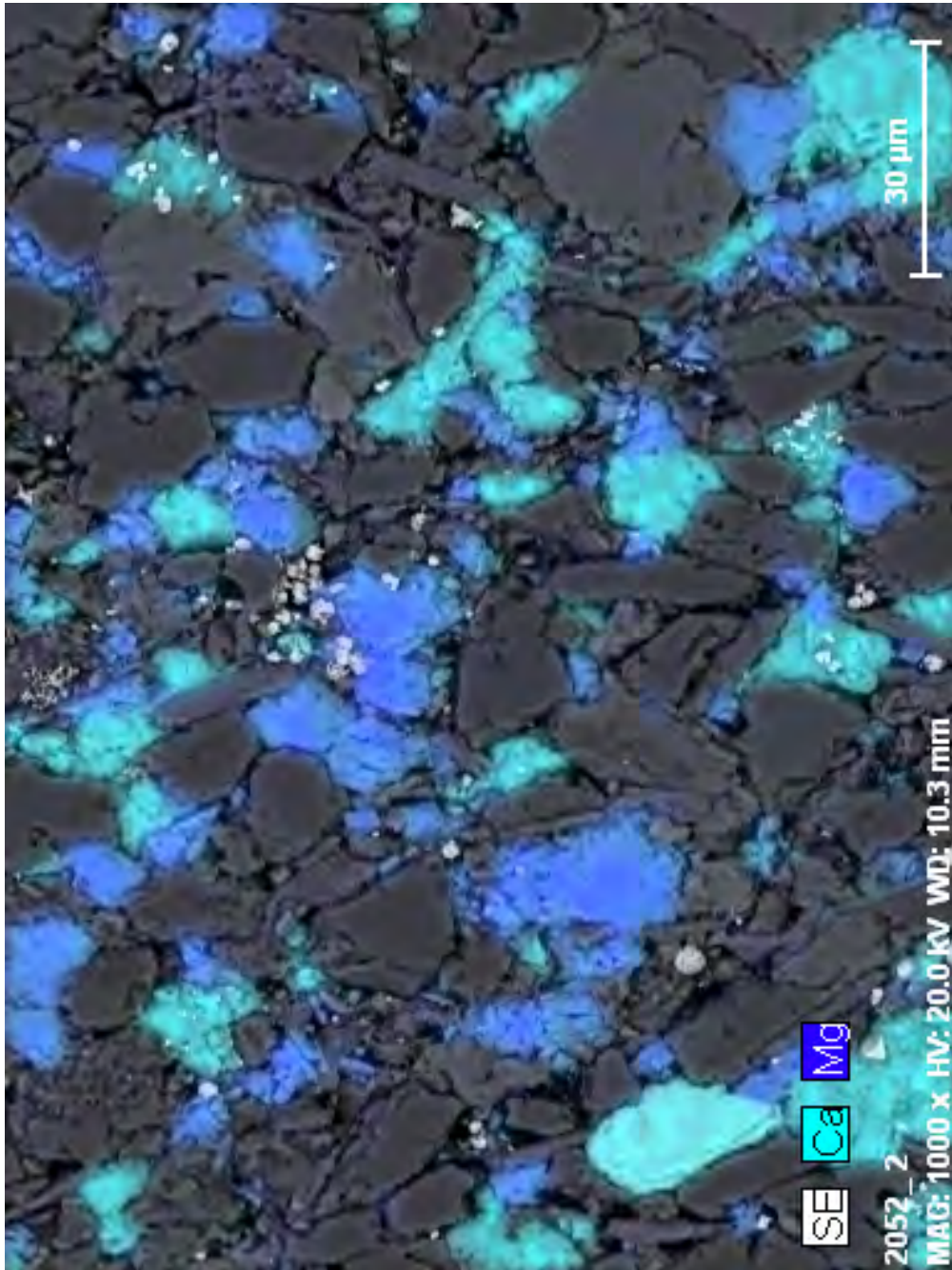
Figure 1-7 Scanning electron microscope image showing dolomite (dark blue) erosion in association with calcite (light blue). Areas where dolomite is seen to be reverting to calcite internally are interpreted as dedolomite. Note the occurrence of mica (the elongate mineral center left), and pyrite (pale grey to white framboids and crystalline nodules center and bottom right). Micropores are visible as dark black regions. This sample is from 2041 m depth within well d-48-A/94-b-9.
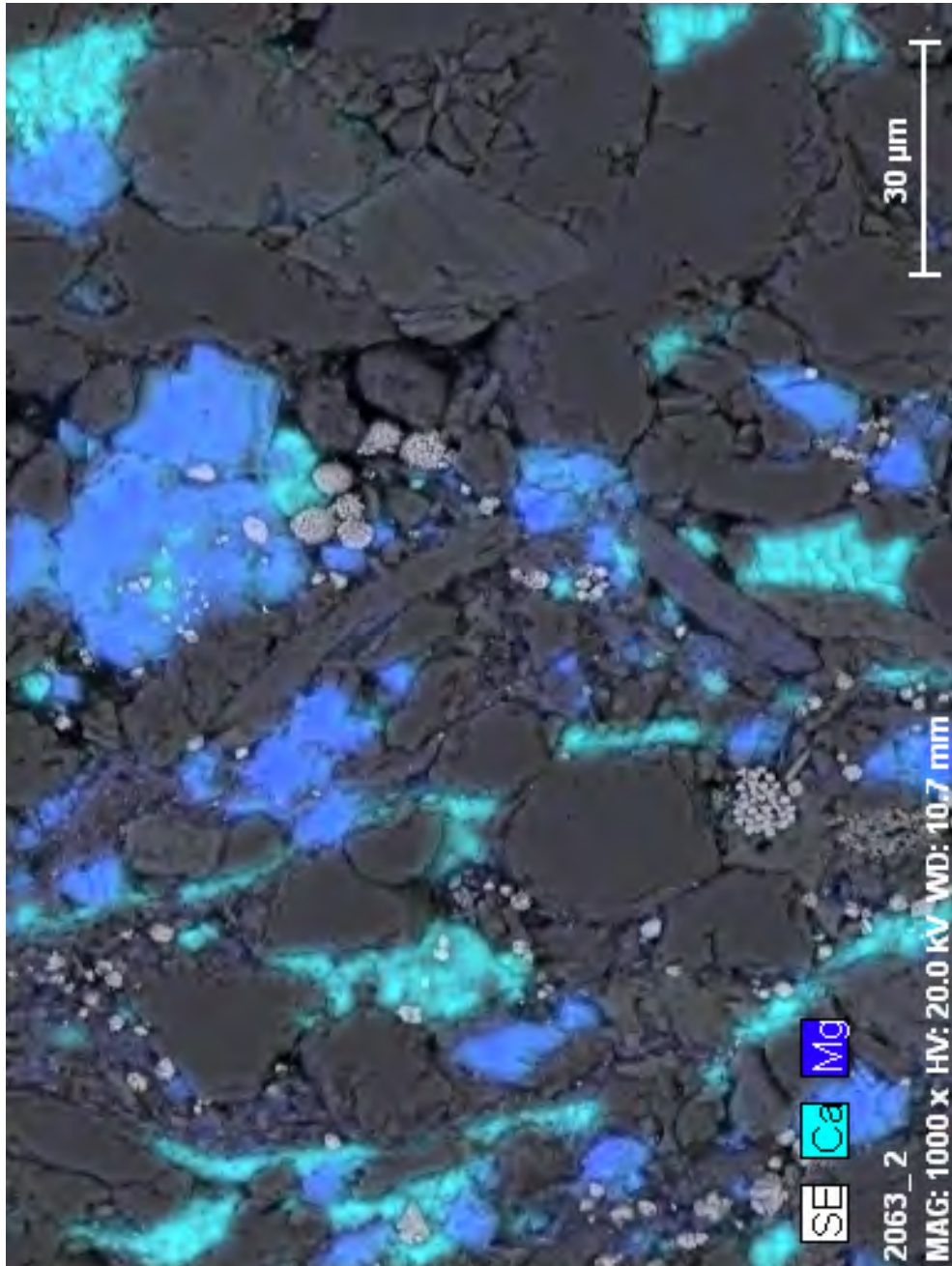
Figure 1-8 Calcite (light blue) and dolomite (dark blue) are visible in this SEM image. Note the occurrence of calcite cement. This image also shows the occurrence of pyrite framboids (light grey to white). This sample is from well d-48-A/94-b-9 at 2063 m depth.
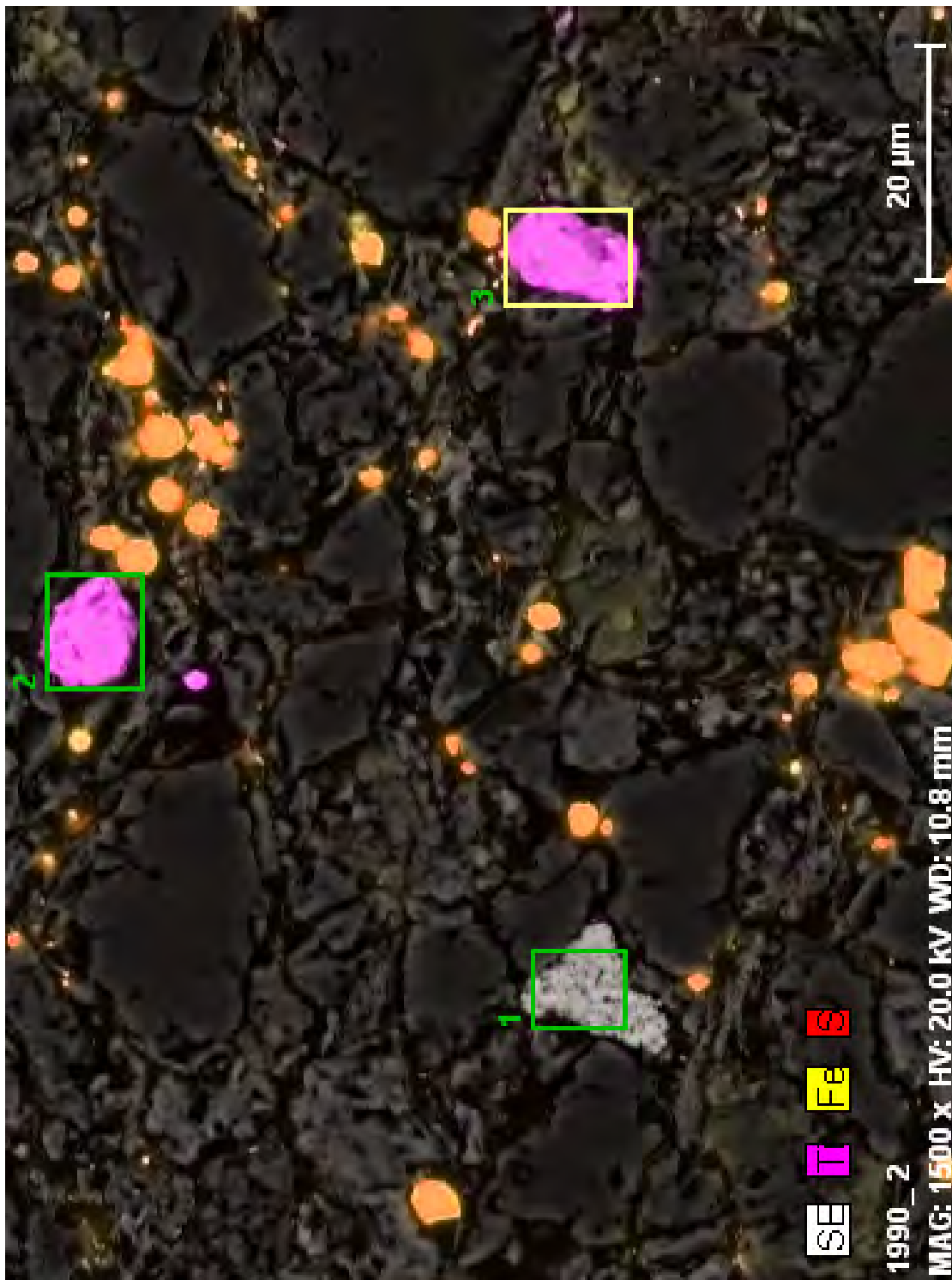
Figure 1-9 Scanning electron microscope image depicting a phosphatic grain (1; pale grey), rutile (2 and 3; pink), and pyrite (orange). This sample was taken from well d-48-A/94-b-9 at 1990 m depth.
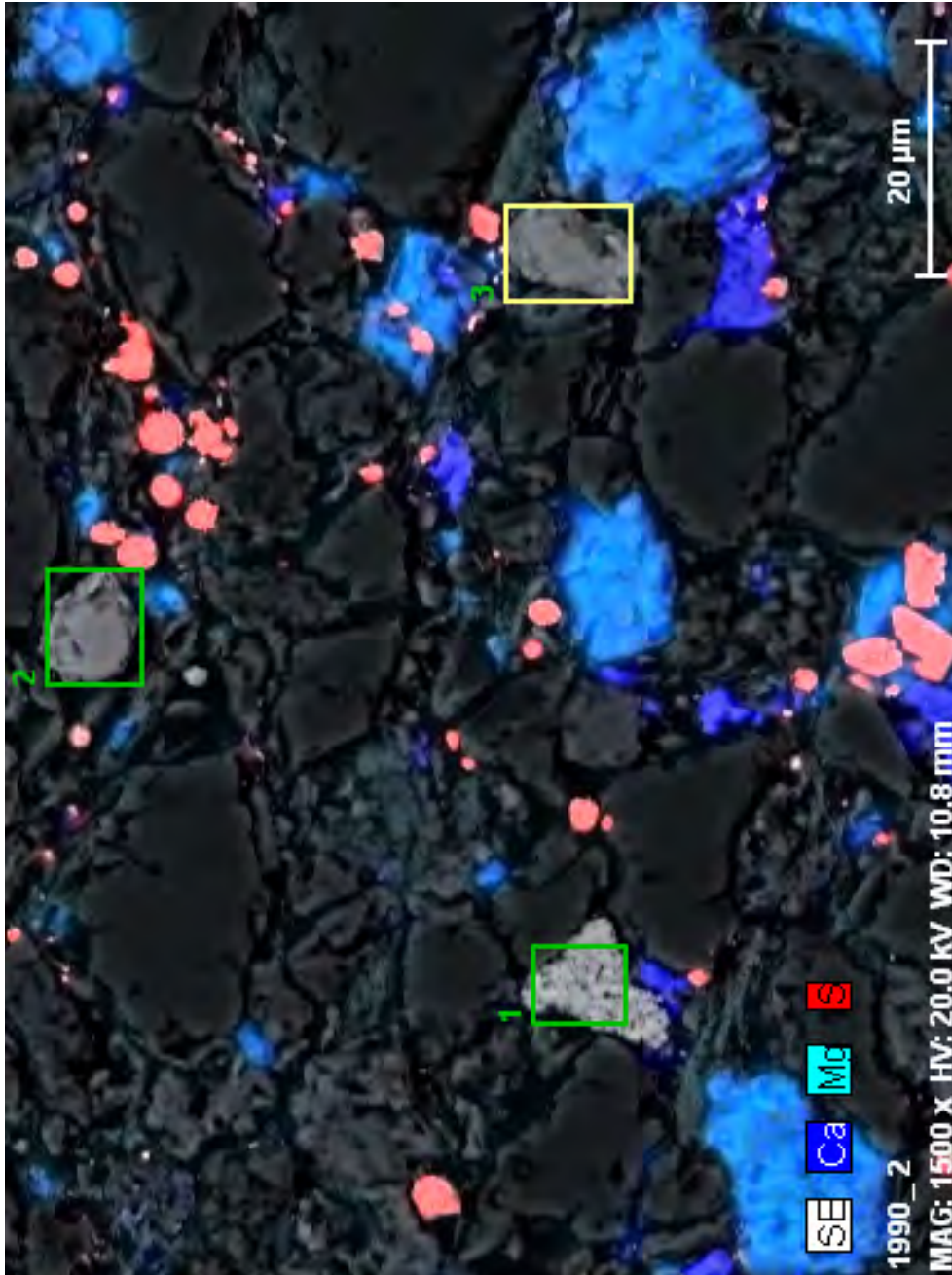
Figure 1-10 This SEM image shows the same region as Figure 10. Cabonate minerals (calcite light blue, dolomite dark blue) and pyrite (pink) are highlighted. Note also the platy features of Illite forming between the grey-scale grains in small amounts. This sample was taken from well d-48-A/94-b-9 at 1990 m depth.
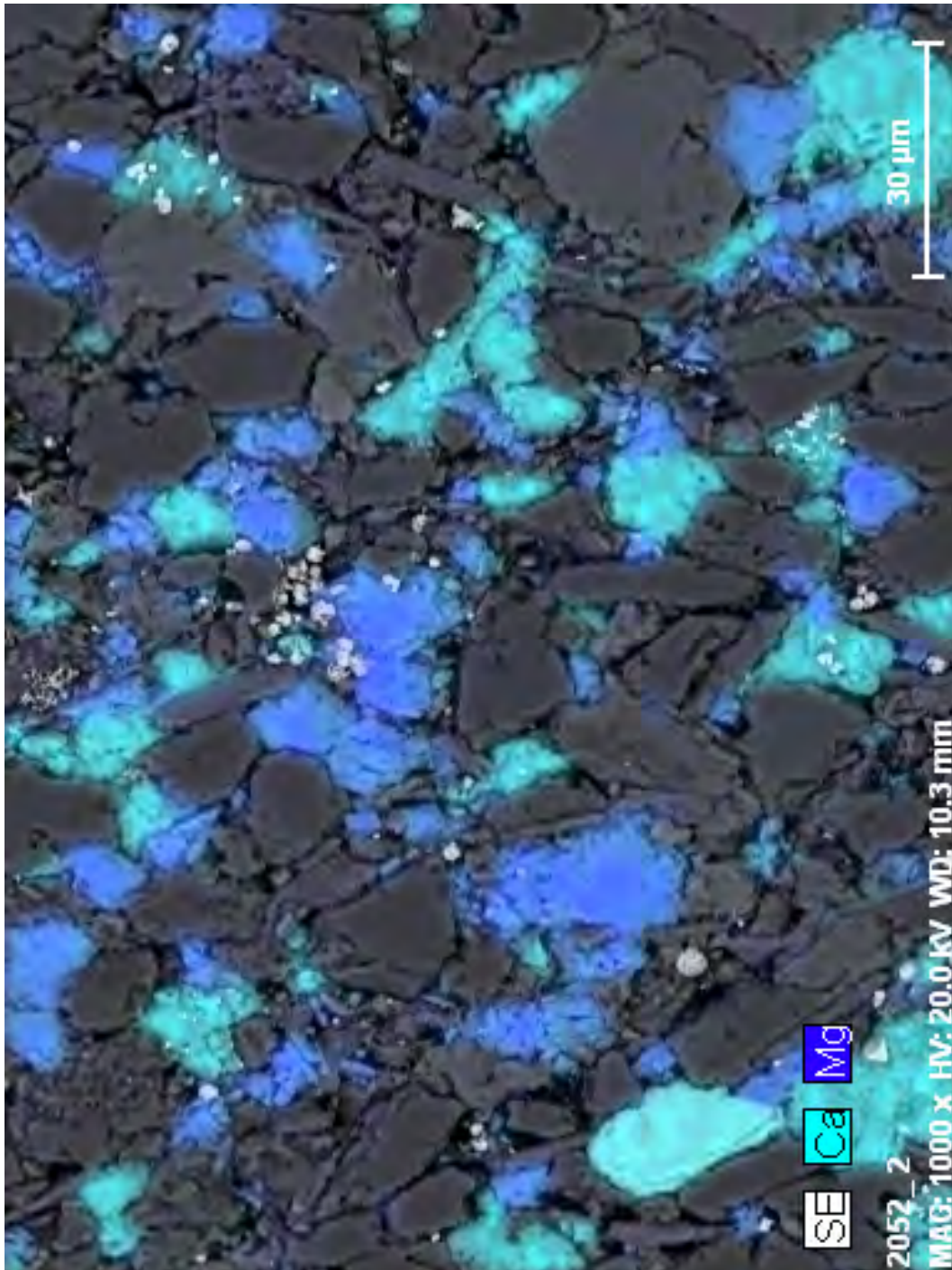
Figure 1-11 Scanning electron microscope image showing regions of calcite (speckled light blue) and dolomite (dark blue). The bright, light blue angular grain bottom left is a calcium phosphate grain. Light grey to white pyrite framboids are also observable. This sample is from 2052 m within well d-48-A-94-b-9.
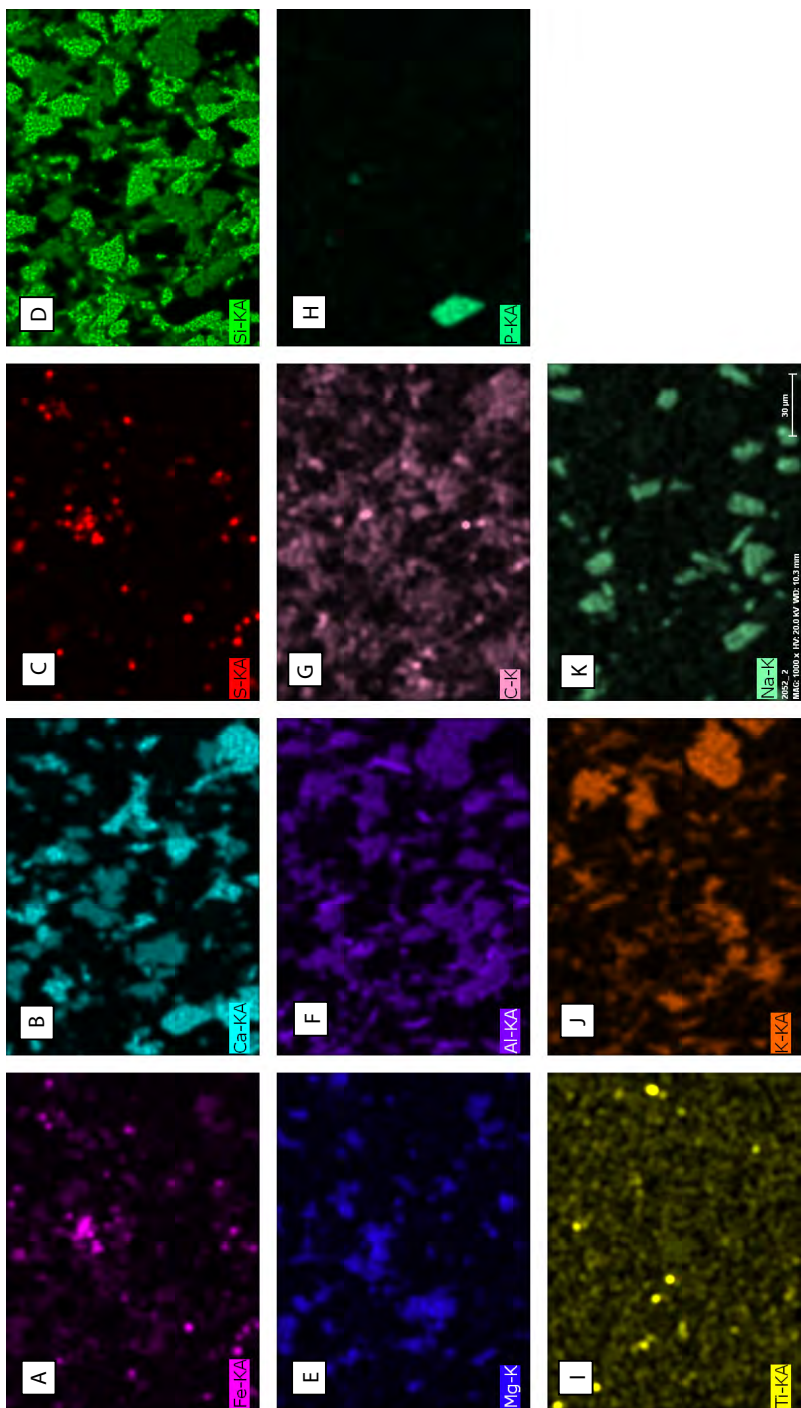
Figure 1-12 Scanning electron microscope elemental maps showing (from top left to bottom right) iron, calium, sulphur, silicon, magnesium, alluminium, carbon, phosphate, titanium, potassium and sodium. Colour brightness is associated with higher elemental concentration. The phosphate grain seen in Figure 6 is clearly visible in the phosphate map. The occurrence of pyrite is observable in the sulphur concentration map. Very bright regions in the map of carbon may indicate the presence of kerogen associated with the micropores. However, the sample was coated in carbon for analysis. This sample is from 2052 m within well d-48-A/94-b-9.
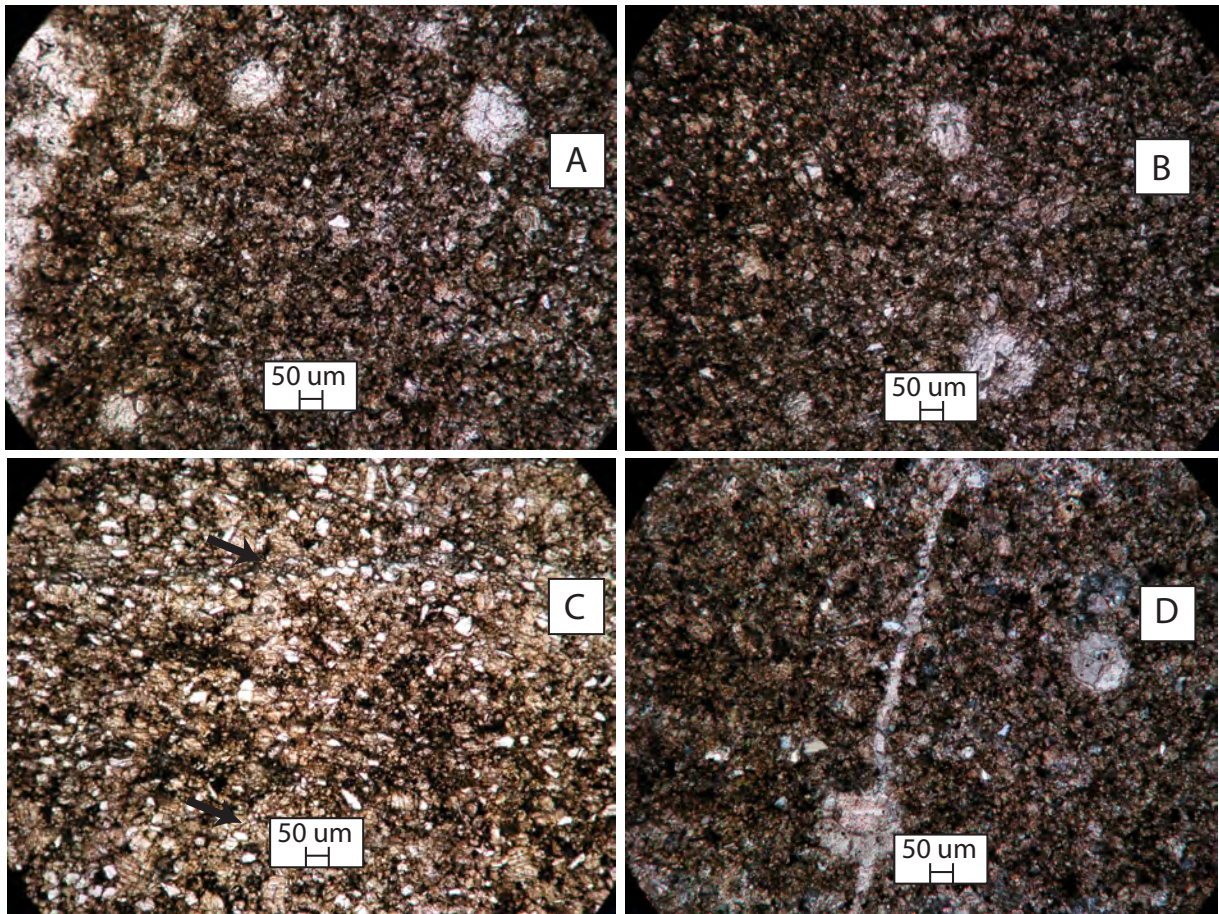
Figure 1-13 Thin section photomicrographs of Microfacies 2 showing calcite spheres interpreted as calcispheres (**A** and **B**). Shell fragments are visible in **A** and **C** as dark parabolic lines. An example is pointed out in **C**. Vertical fractures infilled with calcite are interpreted as possible stylolites (**D**). Images shown are from samples taken at depths of 2033 m (**A**, **B** and **D**) and 2044 m (**C**) from within well d-48-A/94-b-9.
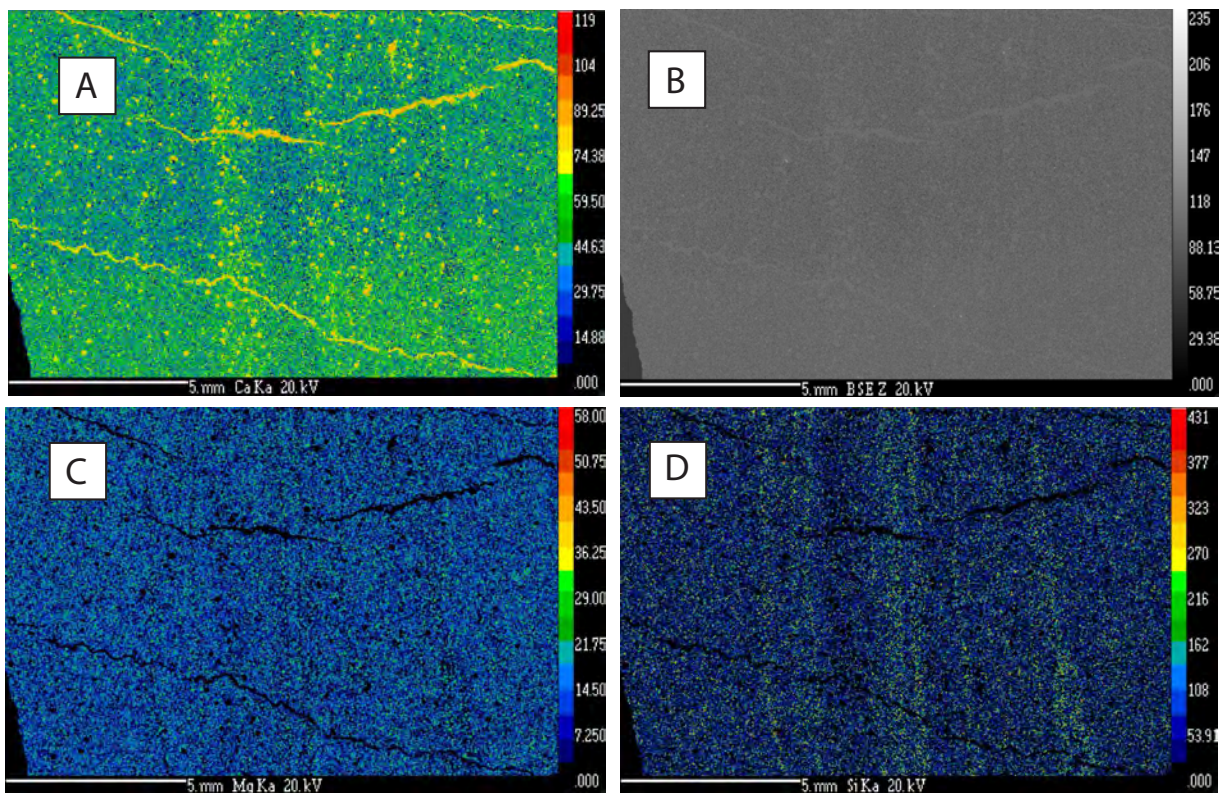
Figure 1-14 Electron microprobe elemental maps (false colour images) depicting calcium (**A**), magnesium (**C**) and silicon (**D**). The backscattered electron image is also displayed (**B**). Note the dominance of carbonate minerals (shown by the elemental maps depicting calcium and magnesium). The layers of calcispheres/ooids are also visible as is the laminae and stylolites characteristic of this microfacies. These images are of a sample taken from well d-48-A/94-b-9 at 2033 m depth.
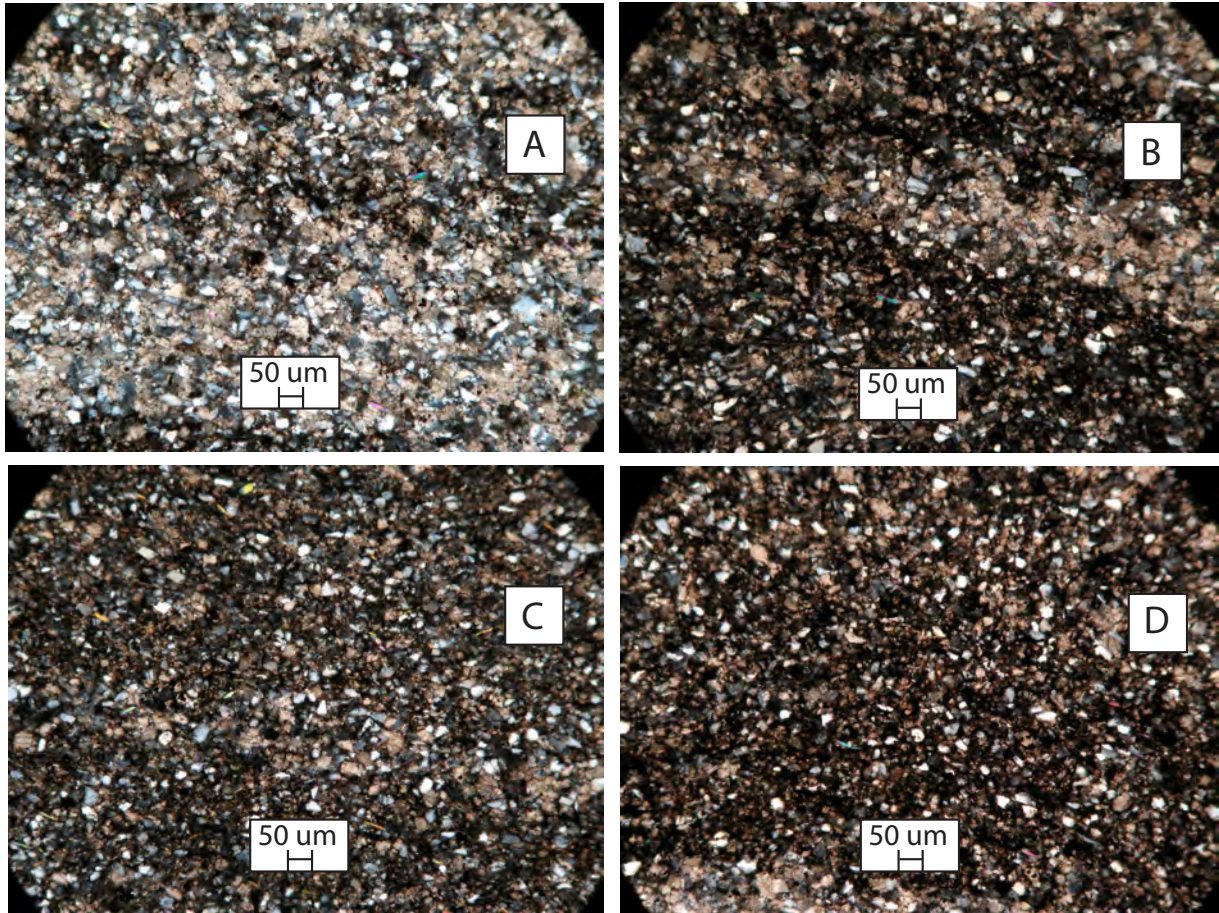
Figure 1-15 Thin section photomicrographs of microfacies 3 (**A** through **B**). Note the similarities with microfacies 1 (coarse and fine laminae, fining upward trends, pinching and swelling laminae). Microfacies 3 however lacks fractures. These images were taken under cross polarized light. All images are from a sample taken at 1993 m depth from well d-48-A/94-b-9.
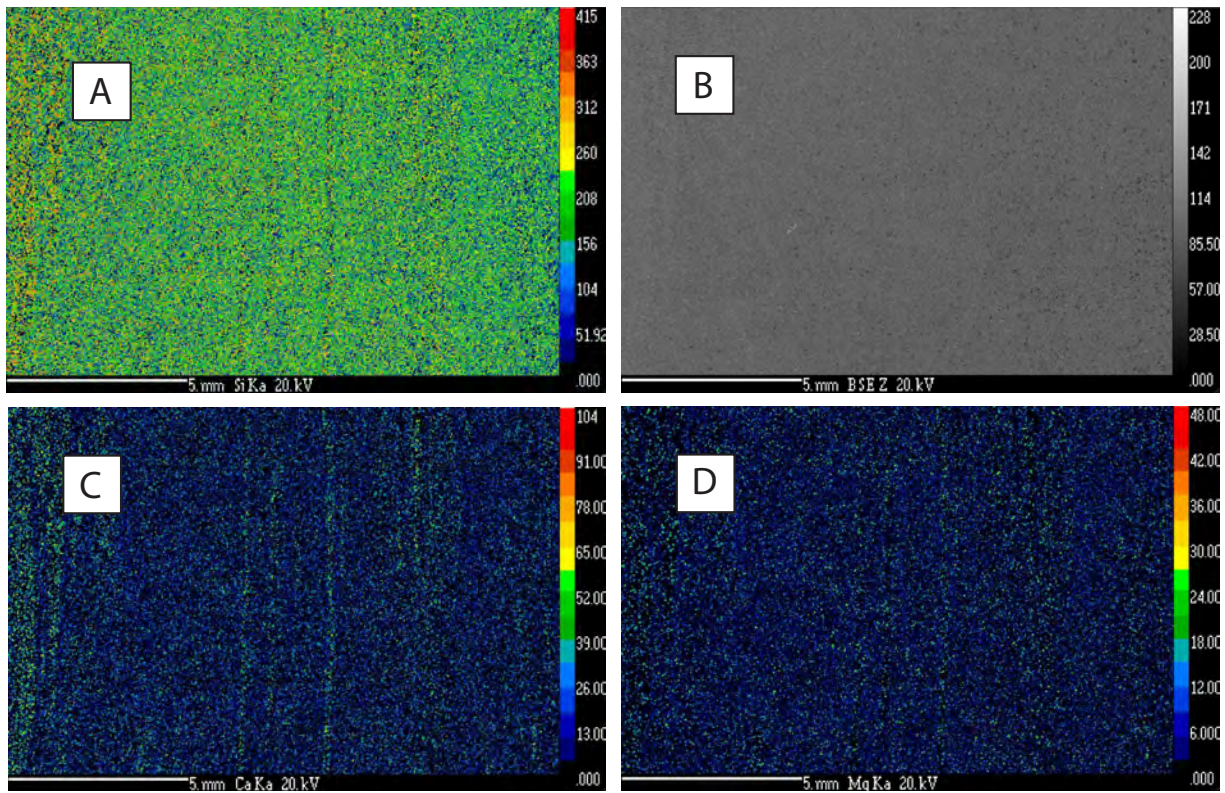
Figure 1-16 Electron microprobe elemental maps (false colour images) showing silicon (**A**), calcium (**B**) and magnesium (**C**) content. The backscattered electron image is also shown (**B**). Silicate minerals dominate this microfacies. Also, note the lack of fracture. These images are from a sample taken at 1993 m depth from well d-48-A/94-b-9.
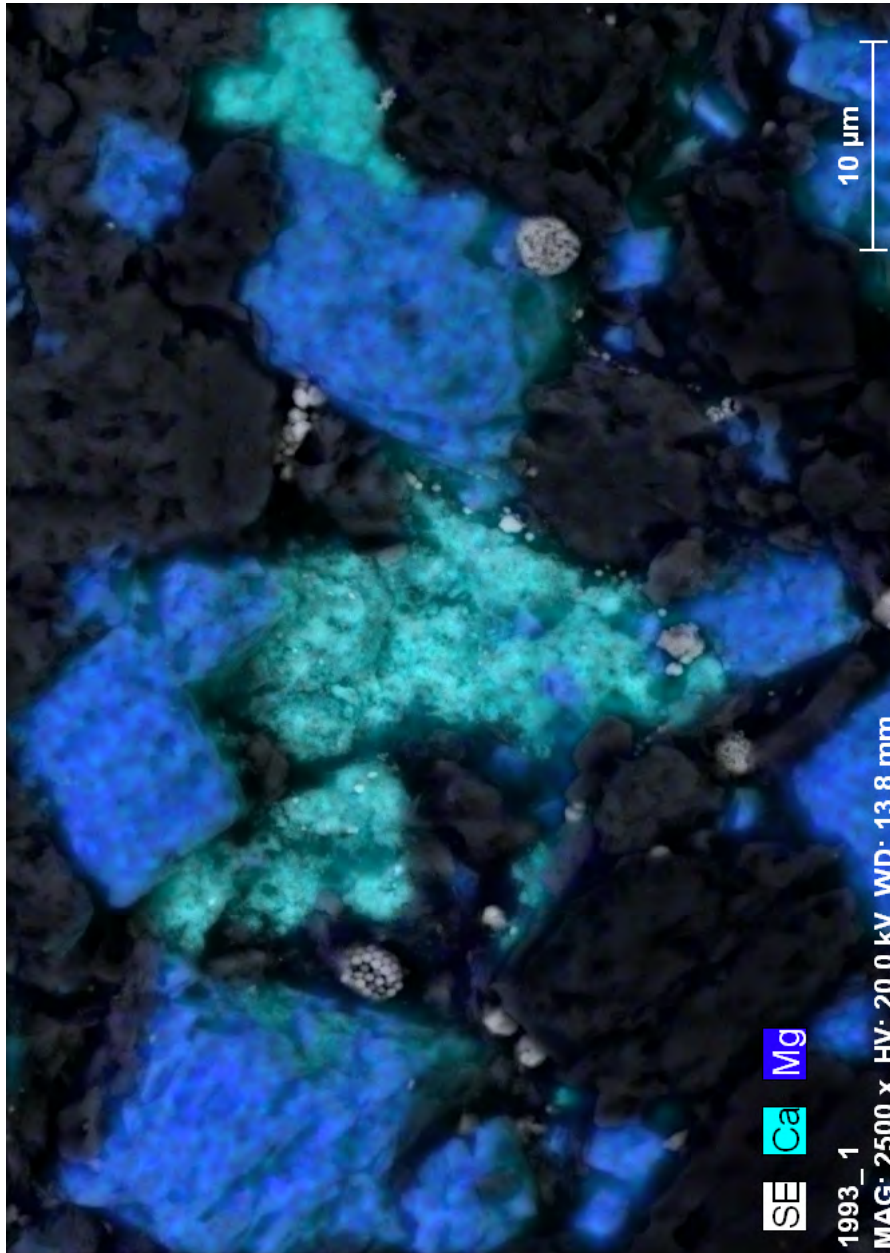
Figure 1-17 A SEM image showing the erosion of dolomite (dark blue) by calcite (light blue. Dedolomite was observed in this microfacies, as with Microfacies 1. Note also the pyrite framboids (pale grey). This image is from a sample taken at 1993 m depth within well d-48-A/94-b-9.
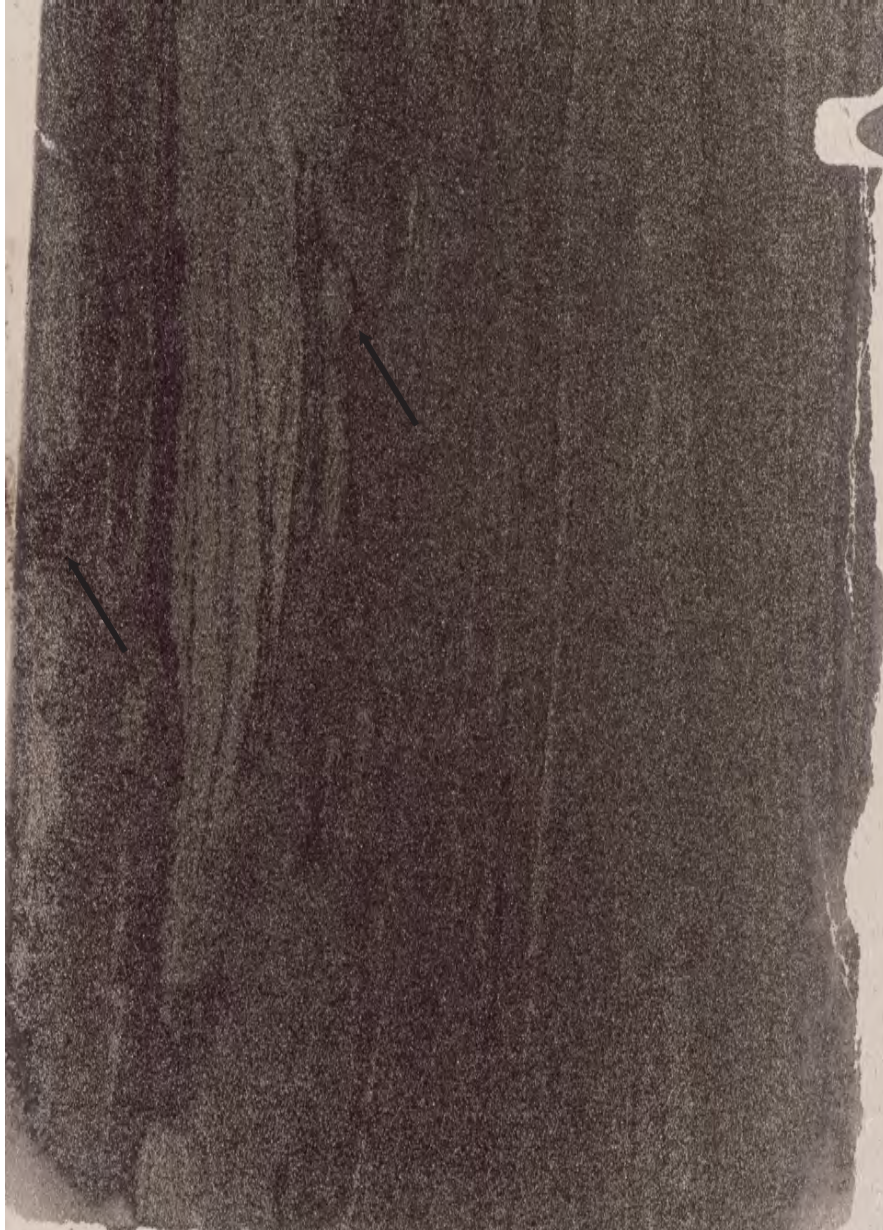
Figure 1-18 Photograph of a thin section showing the occurrence of a possible escape structure (top arrow) and of *Planolites* (lower arrow). Note the observable foresets in the light coloured (coarse grained) laminae interpreted as climbing ripples. Note also the disruption of the laminae by bioturbation. This sample was taken from 1993 m depth within well d-48-A/94-b-9.
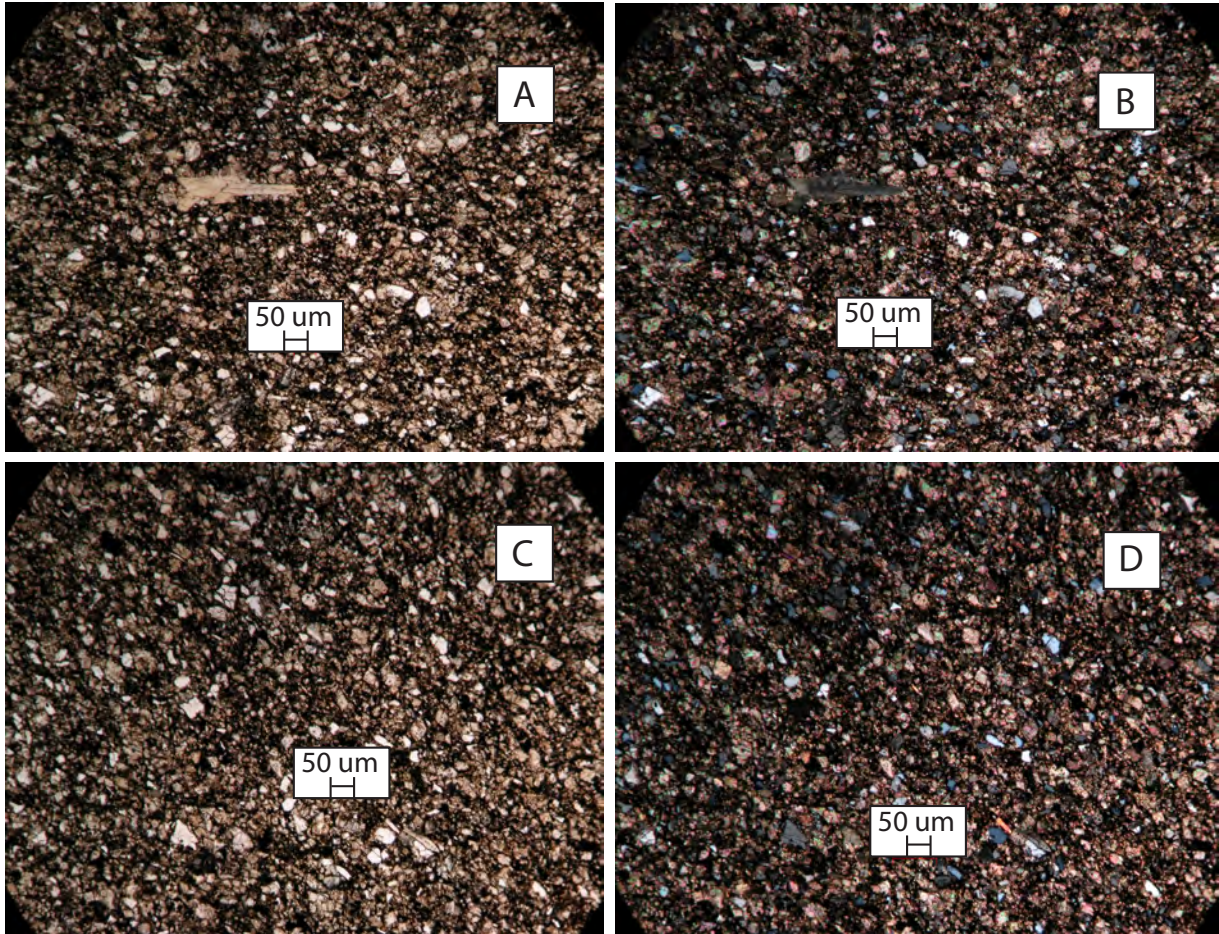
Figure 1-19 Photomicrographs of Microfacies 4 showing the massive nature of this microfacies (**A** through **D**). **A** was taken under plane polarized light; **B** is an image of the same region taken using cross polarized light. **C** was taken under plane polarized light while **D** (taken in the same area) was taken using crossed polarized light. Note the angular nature of the grains. All images are from a single sample taken from well d-48-A/94-b-9 at 1963 m depth.
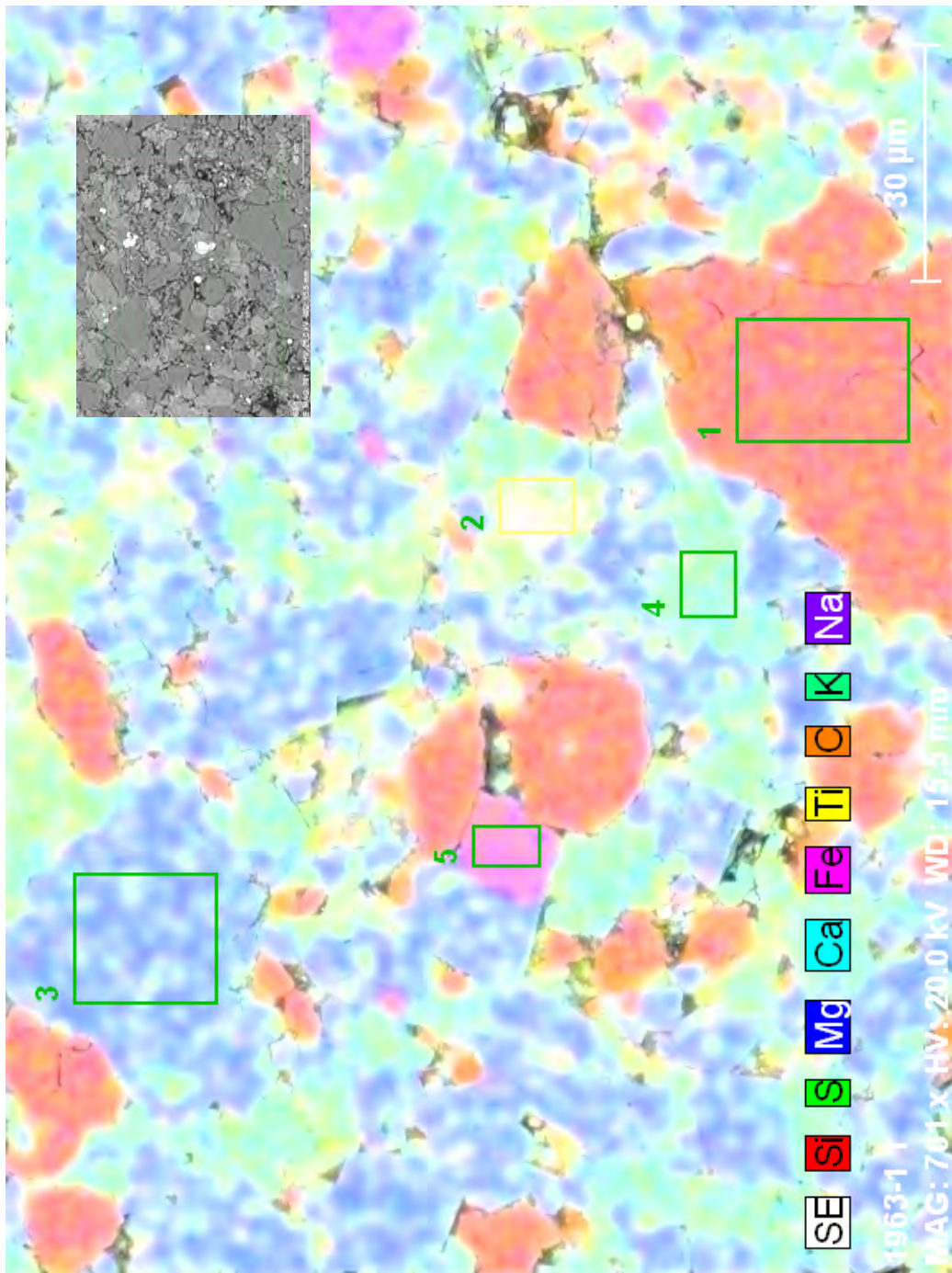
Figure 1-20 SEM image showing elemental concentration of silicon, sulphur, magnesium, calcium, iron and titanium. Inset shows the grey-scale image of the same region. Region 1 shows a quartz grain. Region 2 shows an area with higher clay content surrounding a pyrite grain. Region 3 shows a dolomite grain reverting to calcite (dedolomite). Region 4 shows a region with calcite cement. Region 5 shows a grain of Albite (Na-bearing feldspar). This image is from a sample taken at 1963 m depth from well d-48-A/94-b-9.

Figure 1-21 Electron microprobe elemental maps of Microfacies 4 showing concentrations of sulphur (B), silicon (C), calcium (D) and magnesium (E). The backscattered electron image is also displayed (A). Note the yellow diamond shape in the sulphur elemental map. This may represent a pyritized, cross-cut brachiopod shell. This sample is from well d-48-A/94-b-9 at a depth of 1963 m.
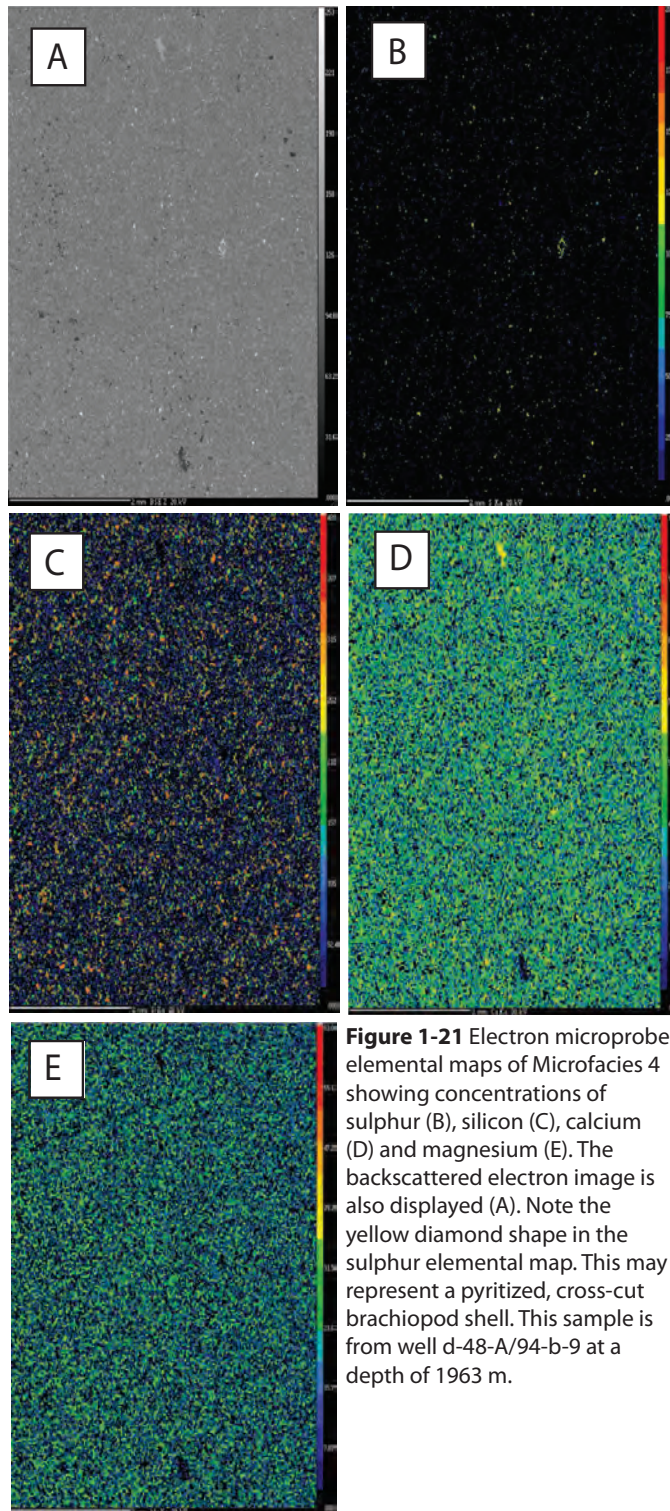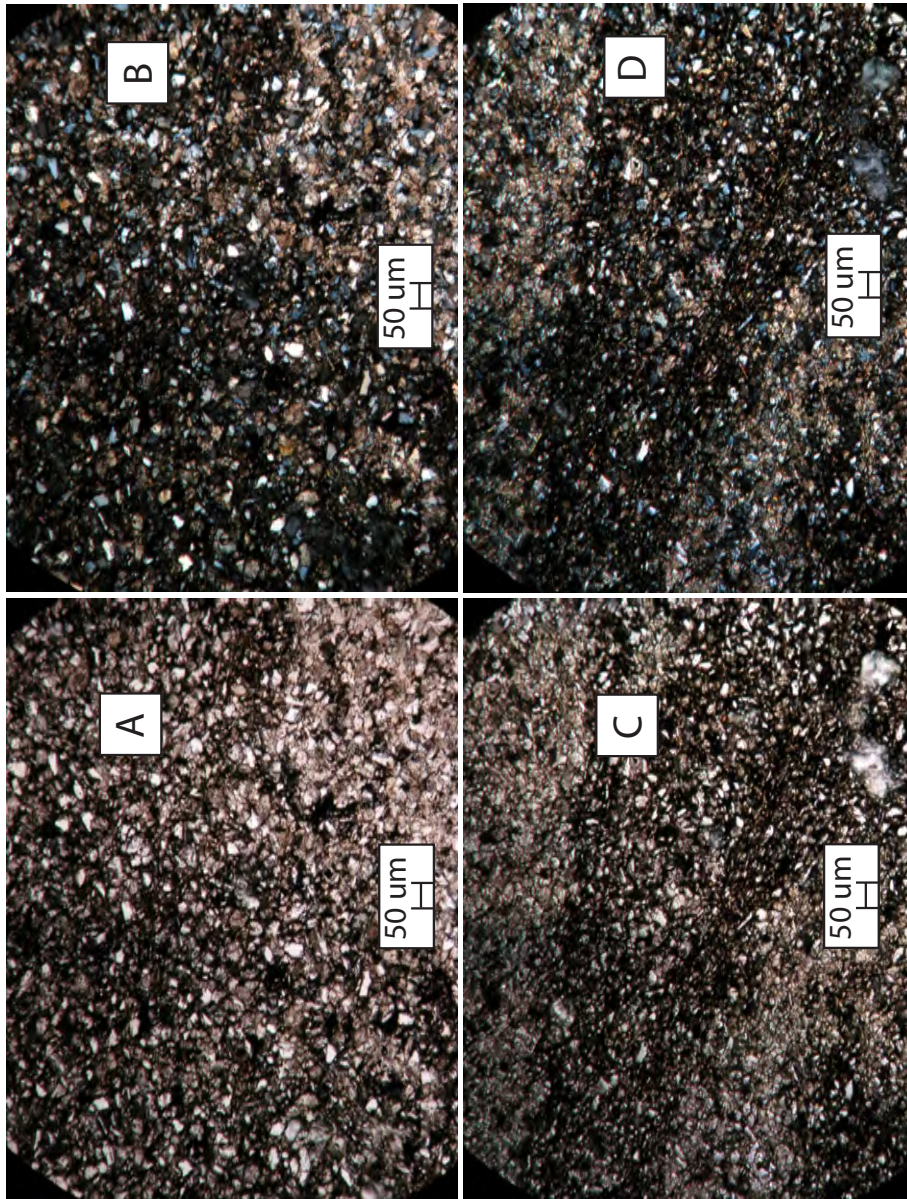
Figure 1-22 Thin section photomicrographs of Microfacies 5. Note the disruption of laminae by bioturbation (A taken using plane polarized light; B taken using crossed polarized light). Plates C (taken using plane polarized light) and D (taken using crossed polarized light) show the pinching and swelling of the coarse and fine grained laminae. All images are of a sample taken from 1986 m depth within well d-48-A/94-b-9.
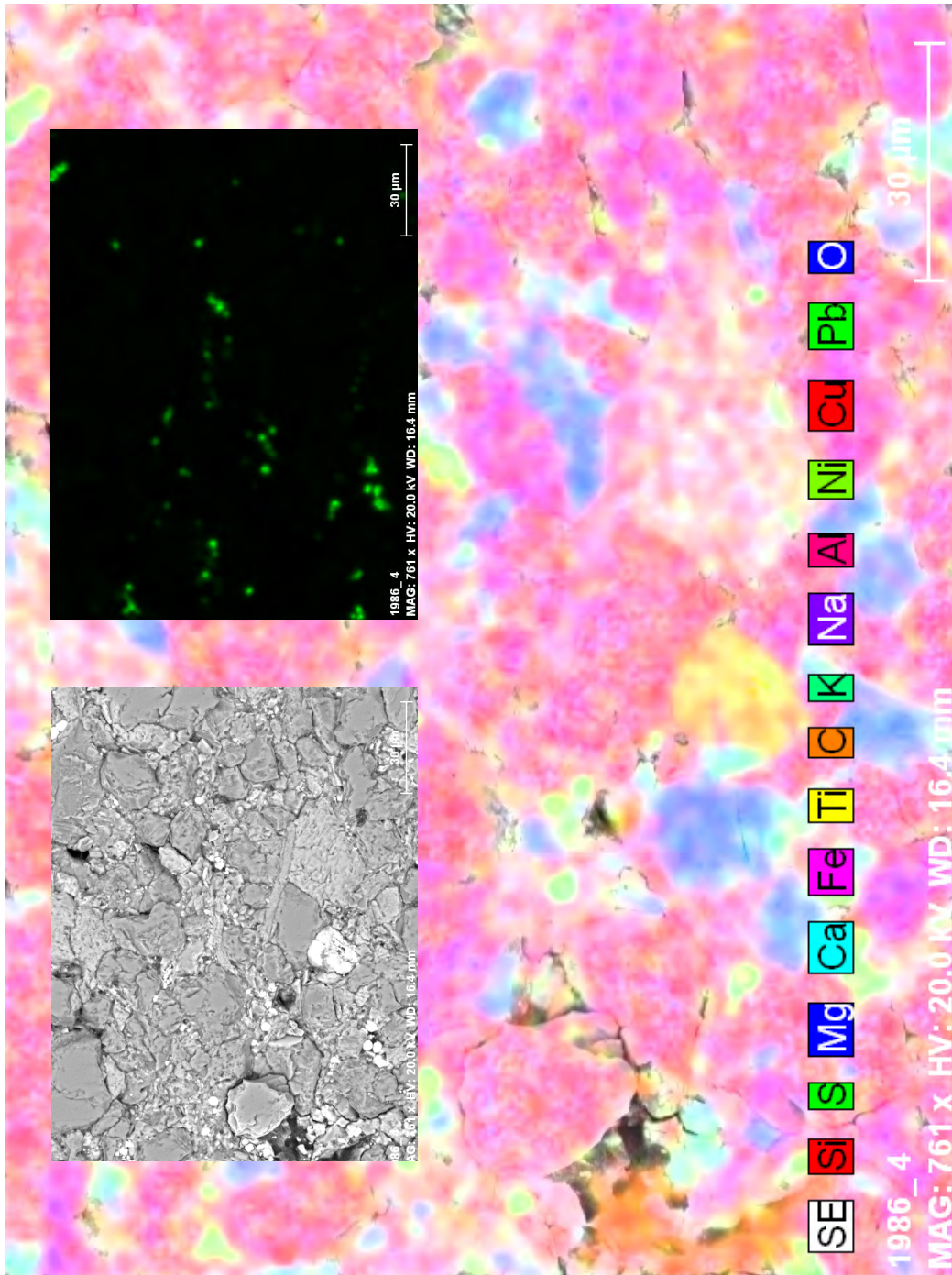
Figure 1-23 SEM image of Microfacies 5 showing elemental concentrations. Left inset is a greyscale image of the same region.Right inset is an elemental map of sulphur of the same region showing the abundance of pyrite (in this case framboidal pyrite). Micropores are clearly visible (pores appear black in the large elemental map and the left inset image). Kerogen (orange) associated with these micropores can be seen clearly (bottom left of the large elemental map). Also visible is calcite cement (blue). Note the dominance of silicate minerals. This sample is from 1986 m depth within well d-48-A/94-b-9.

Figure 1-24 Electron microprobe elemental maps of Microfacies 5. Shown are the elemental maps of calcium (A), carbon (B), silicon (C), alluminium (D), potassium (E) and magnesium (F). Also shown is the backscattered electron image (G). Note the disruption of the laminae; this is best visible in the calcium map (A). Note also the association of carbon content (including kerogen) with pores created by dissolved calcium (best seen in the silicon map, C). All images are from a sample taken at 1986 m depth from well d-48-A/94-b-9.

Figure 1-25 Thin section image showing a central conical shaped laminae disturbance interpreted as Lingulichnus. This sample is from 1986 m depth within well d-48-A/94-b-9.

References

Allen, J.R.L. 1968. Current Ripples, North-Holland Publishing Co., Amsterdam, 433 p.

Alexander, J. and Mulder, T. 2002. Experimental quasi-steady density currents. Marine Geology. v. 186, p. 195-210.

Armitage, J.H. 1962. Triassic oil and gas occurrences in northeastern British Columbia, Canada. Journal of the Alberta Society of Petroleum Geologists, v. 10, p. 35-56.

Arnott, R.W.C. 2010. Deep-marine sediments and sedimentary systems. *In:* Facies Models 4. James, N. P. and Dalrymple, R.W. (eds.). Geoscience Canada, Geotext 6. Geological Association of Canada. p.295-322.

Arnott, R.W.C. and Hand, B.M. 1989. Bedforms, primary structures and grain fabric in the presence of sediment rain. Journal of Sedimentary Petrology. v. 59. p. 1062-1069.

Bagnold, R.A. 1962. Auto-suspension of transported sediment; turbidity currents. Royal Society (London). Proceedings, Series A. v. 265. p. 315-319.

Baker, P.A. and Kastner, M. 1981. Constraints on the formation of sedimentary dolomite. Science, v. 213. p. 214-216.

Barclay, J.E., Krause, F.F., Campbell, R.I. and Utting, J. 1990. Dynamic casting and growth faulting: Dawson Creek Graben Complex, Carboniferous-Permian Peace River Embayment, western Canada. *In:* Geology of the Peace River Arch. S.C. O' Connell and J.S. Bell (eds.). Bulletin of Canadian Petroleum Geology, v. 38A, p. 115-145.

Beauchamp, B. and Grasby, S.E. 2012. Permian lysocline shoaling and ocean
        acidification along NW Pangea led to carbonate eradication and chert
        expansion. Palaeogeography, Palaeoclimatology, Palaeoecology, v. 350-352.
        p. 73-90.

Beranek, L.P. 2006. A Triassic link between Yukon-Tanana terrane and North
        America: new detrital zircon age, geochemical, and biostratigraphic data.
        102nd Annual Meeting of the Cordilleran Section, GSA, 81st Annual Meeting
        of the Pacific Section, AAPG, and Meeting of the Alaska Section, SPE.
        Geological Society of America *Abstracts with Programs,* v. 38, p. 5.

Beranek, L.P., and Mortensen, J.K., 2008. New stratigraphic and provenance studies
        of Triassic sedimentary rocks in Yukon and northern British Columbia. In:
        Emond, D.S., Blackburn, L.R., Hill, R.P. and Weston, L.H., Yukon Exploration
        and Geology 2007, p. 115-124.

Bond, D.P.G. and Wignall, P.B. 2010. Pyrite framboid study of marine Permian-
        Triassic boundary sections: a complex anoxic event and its
        relationship to contemporaneous mass extinction. Geological Society of
        America Bulletin, v. 122. p. 1265-1279.

Bouma, A.H. 1962. Sedimentology of some flysch deposits. Amsterdam. Elsevier, 162
        p.

Burns, S.J., McKenzie, J.A. and Vasconcelos, C. 2000. Dolomite formation and
        biogeochemical cycles in the Phanerozoic. Sedimentology, v. 1. p. 49-61.
        Suppl.

Davies, G.R. 1997. The Triassic of the Western Canada Sedimentary Basin: tectonic
        and stratigraphic framework, Palaeogeography, Paleoclimate and biota. In:

Triassic of the Western Canada Sedimentary Basin. T.F. Moslow and J. Wittenberg (eds.) Bulletin of Canadian Petroleum Geology, v. 45, p. 434-460.

Davies, G.R., Moslow, T.F. and Sherwin, M.D. 1997. The Lower Triassic Montney Formation, west-central Alberta. In: Triassic of the Western Canada Sedimentary Basin. T.F. Moslow and J. Wittenberg (eds.) Bulletin of Canadian Petroleum Geology, v. 45, p. 474-505.

Dixon, J. 2000. Regional lithostratigraphic units in the Triassic Montney Formation of western Canada. Bulletin of Canadian Petroleum Geology, v. 48, p. 80-83.

Domeier, M., Van der Voo, R. and Torsvik, T.H. 2012. Paleomagnetism and Pangea: The road to reconciliation. Tectonophysics, v. 514, p. 514-517.

Drzewiecki, P.A. and Simo, J.A.T. 1997. Carbonate platform drowning and oceanic anoxic events on a mid-Cretaceous carbonate platform, south-central Pyrenees, Spain. Journal of Sedimentary Research, v. 67, p. 698-714.

Edwards, D.E., Barclay, J.E., Gibson, D.W., Kvill, G.E. and Halton, E. 1994. Triassic strata of the Western Canada Sedimentary Basin: In: Geological Atlas of the Western Canada Sedimentary Basin. G.D. Mossop and I. Shetsen (comps.). Canadian Society of Petroleum Geologists and Alberta Research Council, p. 259-275.

Erwin, D.H. 2006. Extinction: How life on earth nearly ended 250 million years ago. Princeton University Press, Princeton, New Jersey, 296 p.

Faraj, B., Harold, W., Addison, G., McKinstry, B., Donaleshen, R., Sloan, G., Lee, J., Anderson, T., Leal, R., Anderson,C., Lafleur, C., and A. Ahlstrom, 2002. Shale gas potential of selected Upper Cretaceous, Jurassic, Triassic and Devonian

shale formations in the WCSB of Western Canada: Implications for shale gas production. *Gas Technology Institute.* Des Plaines, Illinois. 103 p.

Ferri, F. and Zonneveld, J.P., 2008. Were Triassic rocks of the Western Canada Sedimentary Basin deposited in a foreland? Canadian Society of Petroleum Geologists Reservoir, v. 35, p.12-14.

Föllmi, K.B. and Grimm, K.A. 1990. Doomed pioneers: gravity-flow deposition and bioturbation in marine oxygen-deficient environments: Geology, v. 18, p. 1069-1072.

Gibson, D.W. and Edwards, D.E. 1990. An overview of Triassic stratigraphy and depositional environments in the Rocky Mountain Foothills and western Interior Plains, Peace River Arch area, northeastern British Columbia. In: Geology of the Peace River Arch. S.C. O'Connell and J.S. Bell (eds.). Bulletin of Canadian Petroleum Geology, v. 38A, p. 146-158.

Golonka, J., Ross, M.I. and Scotese, C.R. 1994. Phanerozoic paleogeographic and paleoclimatic modelling maps. In: Embry, A.F. and others (eds), Pangea: Global environments and resources.Canadian Society of Petroleum Geologists, Memoir 17, p. 1-47.

Golonka, J. and Ford, D. 2000. Pangean (Late Carboniferous - Middle Jurassic) paleoenvironment and lithofacies. Palaeogeography, Palaeoclimatology, Palaeoecology, v. 161. p. 1-34.

Groves, J. R., Altiner, D., Boyce, M.D. and Craig, B.J. 2003. "Disaster oolites" in the Permian–Triassic boundary interval, Tauride Mountains (Turkey). Geological Society of America, Abstracts With Programs, North-Central Section, v. 35, p.48.

Groves, J.R. 2004. Lower Triassic oolites in Tethys: a sedimentological response to
the end-Permian mass extinction. Denver Annual Meeting, Geological Society
of America Abstracts with Programs, v. 36. p. 336.

Groves, J.R., Altiner, D. and Rettori, R. 2005. Extinction, survival, and recovery of
Lagenide Foraminifers in the Permian-Triassic boundary interval, Central
Taurides, Turkey. Journal of Paleontology, v. 79, p 1-38.

Hayes, L.E., Beatty, T.W., Henderson, C.M., Love, G.D., and Summons, R.E., 2007.
Evidence for photic zone euxinia through the end-Permian mass extinction in
the Panthalassic Ocean (Peace River Basin, Western Canada). Palaeoworld,
v. 16, p. 39-50.

Hodgson, D.M., Flint, S.S., Hodgetts, D., Drinkwater, N.J., Johannessen, E.P. and
Luthi, S.M. 2006. Stratigraphic evolution of fine-grained submarine fan
systems, Tangua Depocentre, Karoo Basin, South Africa. Journal of
Sedimentary Research, v. 76, p.19–39

Ibrahimbas, A. and Riediger, C. 2004. Hydrocarbon source rock potential as
determined by Rock-Eval 6/TOC pyrolysis, Northeast British Columbia and
Northwest Alberta. *British Columbia Ministry of Energy, Mines and Petroleum
Resources*, Summary of Activities, p. 7-17.

Jobe, Z.R., Lowe, D.R. and Morris, W.R. 2012. Climbing-ripple successions in
turbidite systems: depositional environments, sedimentation rates and
accumulation times. Sedimentology, v. 59, p. 867-898.

Jørgensen, B.B. 1982. Mineralization of organic matter in the sea bed - the role of
sulphate reduction. Nature, v. 296, p. 643-645.

Kempe, S. 1990. Alkalinity: The link between anaerobic basins and shallow water
carbonates?. Naturwissenschaften, v. 77. p. 426-427.

Krause, S., Liebetrau, V., Gorb, S., Sánchez-Román, M., McKenzie, J.A. and Treude,
T. 2012. Microbial nucleation of Mg-rich dolomite in exopolymeric substances
under anoxic modern seawater salinity: new insights into an old enigma.
Geology, v. 40, p. 587-590.

Lippmann, F. 1973. Sedimentary carbonate minerals. Springer-Verlag, New York.
228p.

Lloyd, R. M., Perkins, R.D. and Kerr, S.D. 1987. Beach and shoreface
ooid deposition on shallow interior banks, Turks and Caicos Islands,
British West Indies. Journal of Sedimentary Petrology, v. 57, p. 976–
982.

Lowe, D.R. 1982. Sediment gravity flows: II. Depositional models with special
reference to the deposits of high-density turbidity currents. Journal of
Sedimentary Petrology, v. 52. p. 279-297.

Machel, H.G. and Mountjoy, E.W. 1987. Chemistry and Environments of
Dolomitization - a reappraisal. Earth-Science Reviews, v. 23. p. 175-222.

Marynowski, L., Zaton, M., Rakocinski, M., Filipiak, P., Kurkiewicz, S. and Pearce, T.J.
2012. Deciphering the upper Famennian Hangenberg black shale
depositional environments based on multi-proxy record. Palaeogeography,
Palaeoclimatology, Palaeoecology, v. 346. p. 66-86.

Middleton, G.V. and Hampton, M.A. 1973. Sediment gravity flows: mechanics of flow
and deposition. *In:* Turbidites and deep-water sedimentation. Middleton, G.V.

and Bouma, A.H. (eds.). Society of Economic Paleontologists and
Mineralogists Special Publication. p. 1-38.

Moslow, T.F. 2000. Reservoir architecture of a fine-grained turbidite system: Lower
Triassic Montney Formation, Western Canada Sedimentary Basin. *In:*
Deep-water reservoirs of the world, Conference Proceedings, Gulf Coast
SEPM. P. Weimer, R.M. Slatt, J. Coleman, N.C. Rosen, H. Nelson, A.H.
Bouma, M.J. Styzen, and D.T. Lawrence (eds.). p. 686-713.

Moslow, T.F. and Davies, G.R. 1997. Turbidite reservoir facies in the Lower Montney
Formation, west-central Alberta. *In:* Triassic of the Western Canada
Sedimentary Basin. T.F. Moslow and J. Wittenberg (eds.), Bulletin of
Canadian Petroleum Geology v. 45, p. 507-536.

Mulder, T. and Syvitski, J.P.M. 1995. Turbidity currents generated at mouths of rivers
during exceptional discharges to the world oceans. Journal of Geology. v.
103, p. 285-299.

Mulder, T. and Alexander, J. 2001. The physical character of subaqueous
sedimentary density flows and their deposits. Sedimentology, vol. 48. p.
269-299.

Mulder, T, Syvitski, J.P.M, Migeon, S., Faugères, J-C. and Savoye, B. 2003. Marine
hyperpycnal flows: initiation, behavior and related deposits. A review. Marine
and Petroleum Geology. v. 20, p. 861-882.

Mutti, E. and Normark, W.R. 1987. Comparing examples of modern and ancient
turbidite systems: problems and concepts. In: Leggett, J.K. and Zuffa, G.G.
(eds.), Marine Clastic Sedimentology: Concepts and Case Studies p. 1–38.
Graham and Trotman, London.

Orchard, M.J. and Zonneveld, J-P. 2009. The Lower Triassic Sulphur Mountain Formation in the Wapiti Lake area: lithostratigraphy, conodont biostratigraphy, and a new biozonation for the lower Olenekian (Smithian). Canadian Journal of Earth Sciences, v. 46, p. 757-790.

Payne, J.L., Turchyn, A.V., Paytan, A., DePaolo, D.J., Lehrmann, D.J., Yu, M., Wei, J., 2010. Calcium isotope constraints on the end-Permian mass extinction. Proceedings of the National Academy of Sciences of the United States of America, v. 107, p. 8543–8548.

Pilkey, O.H. 1966. Carbonate and clay mineralogy of the Persian Gulf. Deep Sea Research, v. 13, p. 1-16.

Piper, D.J.W. and Normark, W.R. 2009. Processes that initiate turbidity currents and their influences on turbidites: a marine geology perspective. Journal of Sedimentary Research. v. 79, p. 347-362.

Preto, N., Kustatscher, E. and Wignall, P.B. 2010. Trassic climates - State of the art and perspectives. Palaeogeography, Palaeoclimatology, Palaeoecology. v. 290, p. 1-10.

Raup, D.M. 1979. Size of the Permo-Triassic bottleneck and its evolutionary implications. Science, v. 206, p. 217-218.

Sellwood, B. W. and Valdes, P.J. 2006. Mesozoic climates: General circulation models and the rock record. Sedimentary Geology, v. 190, p. 269-287.

Utting, J., MacNaughton, R.B., Zonneveld, J-P., and Fallas, K., 2005. Palynostratigraphy, organic matter and thermal maturity of the Lower Triassic Toad, Grayling and Montney formations of Yukon, British Columbia and Alberta and comparison with the Sverdrup Basin, Nunavut. BCPG 53, p. 5-24.

Van Lith, Y., Warthmann, R., Vasconcelos, C. and McKenzie, J.A. 2003. Sulphate-reducing bacteria induce low-temperature Ca-dolomite and high Mg-calcite formation. Geobiology, v.1, p. 71-79.

Vandeginste, V. and John, C.M. 2012. Influence of climate and dolomite composition on dedolomitization: insights from a multi-proxy study in the central Oman Mountains. Journal of Sedimentary Research, v. 82, p. 177-195.

Vansconcelos, C., McKenzie, J.A., Bernasconi, S., Grujic, D., and Tien, A.J. 1995. Microbial mediation as a possible mechanism for natural dolomite formation at low temperatures. Nature, v. 377, p. 220-222.

Vasconcelos, C. and McKenzie, J.A. 1997. Microbial mediation of modern dolomite precipitation and diagenesis under anoxic conditions (Lagoa Vermelha, Rio de Janeiro, Brazil). Journal of Sedimentary Research, v. 67, p. 378-390.

Walker, R.G.1965. The origin and significance of the internal sedimentary structures of turbidites. Proceedings of the Yorkshire Geological Society, v.35, p.1–32.

Walker, R.G. 1992. Turbidites and submarine fans. In: Walker, R.G. and James, N. P. (eds.), Facies Models: response to sea level change. Geoscience Canada, Geotext 1, Geological Association of Canada, p.239-263.

Walsh, W. Adams, C., Kerr, B. and Korol, J. 2006. Regional "Shale Gas" potential of the Triassic Doig and Montney Formations, Northeastern British Columbia. British Columbia Petroleum Geology Open File 2006-02, 20 p.

Warren, J. 2000. Dolomite: occurance, evolution and economically important associations. Earth-Science Reviews, v. 52, p. 1-81.

Warthmann, R., van Lith, Y., Vasconcelos, C., McKenzie, J.A. and Karpoff, A.M. 2000. Bacterially induced dolomite precipitation in anoxic culture experiments. Geology, v. 28, p. 1091-1094.

Wilkin, R.T. and Barnes, H.L., 1997. Formation processes of framboidal pyrite. Geochemica et Cosmochimica Acta, v. 61, p. 323-339.

Wilkin, R.T., Barnes, H.L. and Brantley, S.L. 1996. THe size and distribution of framboidal pyrite in modern sediments: and indicator of redox conditions. Geochemica et Comsochimica Acta, v. 60, p. 3897-3912.

Wright, D.T. and Wacey, D. 2005. Precipitation of dolomite using sulphate-reducing bacteria from the Coorang Region, South Australia: significance and implications. Sedimentology, v. 52, p. 987-1008.

Woods, A.D., Bottjer, D.J., Mutti, M. and Morrison, J. 1999. Lower Triassic large sea-floor carbonate cements: their origin and a mechanism for the prolonged biotic recovery from the end-Permian mass extinction. Geology, v. 27, p. 645-648.

Woods, A.D., Bottjer, D.J. and Corsetti, F.A. 2007. Calcium carbonate seafloor precipitates from the outer shelf to slope facies of the Lower Triassic (Smithian-Spathian) Union Wash Formation, California, USA; sedimentology and palaeobiological significance. Palaeogeography, Palaeoclimatology, Palaeoecology, v. 252, p. 281-290.

Zonneveld, J-P., 2009. Stratigraphy and sedimentary framework of the Lower Triassic Montney Formation, 3rd Unconventional Gas Technical Forum, Victoria, British Columbia, April 2009, Petroleum Geology Information Circular 2009-02, 65 p.

Zonneved, J-P., Beatty, T.W. and Pemberton, S.G. 2007. Lingulide brachiopods and the trace fossil Lingulichnus from the Triassic of Western Canada; implications for faunal recovery after the end-Permian mass extinction. Palaios, v. 22, p. 74-97.

Zonneveld, J-P. and Greene, S.E., 2010. Lingulide response to severe storms recorded in middle Trassic strata of northeastern British Columbia. Palaios, v. 25, p. 807-817.

Zonneveld, J-P., Gingras, M.K. and Beatty, T.W. 2010. Diverse ichnofossil assemblages from the Lower Triassic of northeastern British Columbia: evidence for shallow marine refugia on the northwestern coast of Pangaea. Palaios, v. 25, p. 368-392.

Zonneveld, J-P. 2011. Suspending the rules: unraveling the ichnological signature of the Lower Triassic post-extinction recovery interval. Palaios, v. 26, p. 677-681.

3-D mineralogical assessment of the Montney Formation using micro-ct and electron microprobe analysis

Introduction

Analysis of geological samples often involves the study of thin sections using a transmitted light microscope. Although accurate and robust, this method of analysis can be time consuming (as with point-count analysis) and requires extensive sample preparation. Moreover, thin-section petrography only allows for 2 dimensional study. Pore networks, fractures and 3D grain shape are difficult to assess.

In contrast, X-ray computer tomography (CT) and microfocus computed tomography (micro-ct or µCT) allows for the 3D petrographic analysis of geological samples. Micro-ct analysis is fast and accurate and requires minimal sample preparation (Remeysen and Swennen, 2008). Geoscience applications of micro-ct are widespread (see Duliu, 1999; Mees *et. al.*, 2003 for overviews). This technique has been used in reservoir characterization, such as in pore and fracture studies for fluid flow analysis (Wellington and Vinegar, 1987; Coles *et. al.* 1998; Bertels *et. al.*, 2001; Van Geet *et. al.,* 2002). CT scanning has also been used in geological applications such as paleontology (Snelling *et. al.*, 2010), petroleum engineering (Zhou, *et. al.*, 2010), soil analysis (Monga, *et. al.,* 2008) and sedimentology (Kentner, 1989). Petrological applications have also begun to be explored (Van Geet *et. al.,* 2001; Long *et. al.,* 2009). Diagenetic, petrophysical and quantitative mineralogical studies have been carried out by Van Geet *et. al.* (2000), Van Geet and Swennen (2001), Remeysen and Swennen, (2008) and Long *et. al.* (2009). These studies have shown that 3-D visualizations of pore networks and mineral grains (calcite, dolomite, *etc.*) are possible using micro-ct analysis.

The ability to obtain 3-D images is based on the attenuation of X-rays as they pass through the material. This is exemplified by Beer's law, which states:

$$I = I_0 e^{(-\mu s)} \tag{1}$$

where I_0 represents the initial intensity of the X-rays directed at the sample, μ is the attenuation coefficient of the sample material, *s* is the thickness of the sample and *I* is the final intensity of the X-rays after they are attenuated by the sample (Pullan *et. al.,* 1981; Long *et. al.*, 2009). The detector measures the intensity of the attenuated X-rays and, by rotating the sample around its axis (over 180° or 360°), projected images of the sample are obtained (Long *et. al.*, 2009). These projected images collectively map the distribution of the attenuation coefficients (μ) within the sample material, which depends on density and the effective atomic number of the constituents (Long *et. al.,* 2009). These vertical images are converted, with software, into 2D horizontal slices (Long *et. al.*, 2009). By stacking these slices, 3D images are obtained made up of voxels (Long *et. al.,* 2009). Each voxel represents an average attenuation value for a single volume-element (Long *et. al.,* 2009).

Although previous work has been done on mineral identification and characterization using micro-ct analysis, this has largely been done using dual-energy scanning (Remeysen and Swennen, 2008; Long *et. al.*, 2009) where, by scanning a sample at both low and high energy, density and effective atomic number can be determined (Wellington and Vinegar, 1987; Coenen and Maas, 1994; Van Geet *et. al.*, 2000). An alternative method, the evaluation of which is the purpose of this study, is to use electron microprobe analysis (EMP) to calibrate the micro-ct data and determine the grey-scale values for each mineral constituent. This method does not require multiple scans or internal calibration. A sample of the Lower Triassic Montney Formation will be evaluated using this technique.

Geological Background

The material used in this study comes from a well in northeastern B.C. in the Kobes region. Sample material consists of very fine grained sandstone and siltstone from the Lower Triassic Montney Formation. Mineralogy consists mainly of quartz, dolomite, potassium feldspar, diagenic calcite, plagioclase, mica and pyrite (Davies, 1997; Dixon, 2000; Moslow, 2000; Zonneveld *et. al.*, 2010). The Montney Formation was deposited in the Western Canada Sedimentary Basin along the western coast of Pangea (Davies et. al., 1997; Moslow and Davies, 1997; Dixon, 2000; Moslow, 2000;

Utting et. al., 2005; Hayes et. al., 2007; Zonneveld et. al., 2010). Recent petrological study involving thin section petrography, scanning electron microscope (SEM) and EMP analysis has revealed the existence of abundant dedolomite, pyrite framboids and calcite cementation (this volume, chapter 1). In addition, mineral types were found to be segregated based on the overall grain size of laminae (coarse grained laminae contained quartz and calcite while feldspars and mica were only observed within finer grained laminae) (this volume, chapter 1). Porosity was found to be low (less than 3%; this volume, chapter 1).

The Montney Formation covers an area of approximately 150,000 km² and can reach thicknesses of nearly 300 m (Davies, 1997; Zonneveld et. al., 2010). Estimates of original gas in place range from 5.67-42.8 million m³ (200 to 1500 TCF; Moslow, 2000; Ibrahimbas and Riediger, 2004; Faraj *et al*., 2002). The organic-rich silty shale portions have a total organic carbon content (TOC) ranging from 0.5% to 7% with an overall overage of approximately 4% in productive intervals (Moslow, 2000; Ibrahimbas and Riediger, 2004; Faraj *et al*., 2002). The Montney Formation has become one of Canada's major unconventional gas reservoirs in the last five years making it an interesting formation to study.

Methods

Microfocus Computed Tomography

As previously mentioned, CT analysis (including micro-ct) is a function of Beer's Law. A beam of photons, with intensity I_0, is emitted by the X-ray source and subsequently passes through the sample. While passing through, the photons interact with the sample components, causing the exiting X-ray beam to have a lower intensity, I. This exiting beam is measured by the detector, which converts the X-ray photons received into a digital image. This image is referred to as a radiographic image or a projection image. In the case of micro-ct, the sample is rotated on a stage through a set rotation step (often less than a degree) and another image is taken. Images are taken as the sample is rotated through a full 180° or 360°. These projection images are subsequently used to create horizontal slices by means of a

"filtered back-projection" algorithm (Remeysen and Swennen, 2008). These reconstructed horizontal slices are divided into pixels, which represent the average linear attenuation coefficient over each pixel area. Components of the sample can then be identified based on differences in linear attenuation coefficient as this coefficient is determined by effective atomic number and density. This allows for mineral identification and pore analysis (Remeysen and Swennen, 2006; Remeysen and Swennen, 2008).

Image resolution is affected by sample size (Long, *et. al.*, 2009). The larger the sample, the lower the resolution (Long, *et. al.,* 2009). Sample size is limited by the scanner itself, determined by a ratio (distance separating the detector and the source divided by the distance separating the sample and the source) as well as by the X-ray point source focal spot size (Long, *et. al.*, 2009). However, a large enough sample must be chosen so as to be representative of the larger-scale lithological character (Long *et. al.*, 2009). The pixel size of the detector also has an effect on resolution (Remeysen and Swennen, 2008; Long *et. al.*, 2009). Pixel size can be as small as 1micron (sample size must be extremely small), however, this accounts for pixel width. In the case of a 3 micron pixel width, the area a pixel would encompass would actually be 3^2 microns or 9 μm². When taken into three dimensions, the pixel becomes the voxel and would encompass a volume of 3^3 microns or 27 μm³ (Remeysen and Swennen, 2008). Thus pixel resolution scales geometrically.

Artifacts

Micro-ct analysis is made difficult by a number of artifacts associated with producing images. Star, line and ring artifacts as well as beam hardening are all inherent problems with CT images. Artifacts (ring, line and star) can be reduced during data acquisition and reconstruction using software (Remeysen and Swennen, 2006; Long *et. al.*, 2009). Beam hardening, however, cannot fully be eliminated.

The energy of the X-rays photons has an affect on the linear attenuation coefficient (Remeysen and Swennen, 2008). This is shown in the equation:

$$\mu(E) = \rho Z^{3.8}\,\alpha(E) + \rho\beta(E) \qquad\qquad (2)$$

where μ is the linear attenuation coefficient, E is the X-ray energy, ρ is the density, Z is the atomic number of the scanned substance, α is the Klein-Nishina coefficient and β is a constant (Wellington and Vinegar, 1987). Because polychromatic X-rays are used, beam hardening results and influences the measured attenuation values (Brooks and Di Chiro, 1976). To help prevent this, filters (such as Copper) can be used to absorb weak (low-energy) photons, making the X-rays more monochromatic in nature (Remeysen and Swennen, 2008). Beam hardening is most pronounced in the outer rim of the sample and so the inner portion of the sample is analyzed in order to avoid this issue (Remeysen and Swennen, 2008).

Sample Preparation

Because the Montney Formation is very fine grained and monotonous, a small sample (approximately 1 cm³) was considered to be representative. A single sample was selected for the preliminary examination of this method. The sample was mounted in epoxy with one face exposed (perpendicular to bedding) and polished to a mirror finish. The mounted sample was then scanned at an energy level of 100 kV and a current of 100 μA to obtain projection images. The sample was scanned with a pixel resolution of 3.9 μm. A Skyscan 1072 desktop scanner (located at the University of Alberta) was used, equipped with an aluminum copper filter. The source type consists of a Hamamatsu 100/250 and the camera used was a Hamamatsu 10 Mp camera with an exposure time of 2945 ms. The distance from the sample to source was 73.8 mm and the distance between the camera and source was 215.7 mm. The rotation step was 0.32° and frame averaging was set at 6 with a random movement setting of 20. The sample was rotated over a total of 180°. Flat field corrections as well as geometrical corrections were applied during scanning. The total scan duration was 3 hours and 40 minutes. These images were reconstructed using N-Reconstruction software (SkyScan, 2005). 3D models were created using CT-Analyser and CT-Volume software (SkyScan, 2005).

The sample was then coated in carbon and analyzed using a Cameca SX100 electron microprobe equipped with both wave dispersion spectrometers and electron

dispersion spectrometers. Element maps of the polished surface of each sample were obtained. Elements analyzed for include: Si, Ca, Fe, K, Na, Al, Mg, S, Ti and C (although the samples were carbon coated, relative differences in carbon levels could be determined). Additionally, backscattered electron images were obtained.

Image analysis

The EMP elemental maps and backscattered electron images were compared to the micro-ct slices of the polished sample surface. The correlation between these images was used to determine the grey scale values for each mineral constituent in the micro-ct images. In addition, ideal grey scale values were determined using attenuation coefficients generated from the online database XCOM (hosted by NIST, http://physics.nist.gov/PhysRefData/Xcom/html/xcom1.html). These values were used to further calibrate the micro-ct images (see Table 2-1). Because previous thin section work (chapter 1, this volume) and the electron microprobe analysis allowed for mineral composition to be determined, XCOM values could be used. Grey scale levels were determined by converting the XCOM attenuation coefficients to hounsfield units using the formula:

$HU = (\mu_x - \mu_w) / (\mu_w - \mu_a) \times 1000$

where HU refers to the grey scale level or hounsfield units, μ_x represents the linear attenuation coefficient of the mineral constituent, μ_w represents the linear attenuation coefficient of water (at 20° C) and μ_a refers to the linear attenuation coefficient of air (at 20° C).

Results

Based on the EMP analysis, five major mineral constituents were identified. Pyrite, with relatively high abundances (around 5%) has the highest density and therefore appeared pale grey in the micro-ct images (see Figures 2-1 and 2-2). This mineral was the easiest to identify and was calculated to have a Hounsfield value of 2022. It often occurred within very thin laminae (less than a millimeter thick), although

it was also found scattered throughout the samples (see Figure 2-2). Calcite, which was generally confined to millimeter thick laminae, was also rather straightforward to identify (Figure 2-3). It appeared as a light grey in the micro-ct images (see Figure 2-1). The hounsfield value for calcite was calculated to be 2114. Calcite was found to occupy only 9% or less in the sample examined. Dolomite, likewise did not account for a large portion of the samples, occurring in abundances of 11% or less (see Figure 2-3). Dolomite appeared as darker grey in the micro-ct images (Figure 2-1) and, because it occurred randomly within the sample, was comparably difficult to identify. The calculated hounsfield value was found to be 2022 when using XCOM data. Dolomite grains were also found containing calcite cores after the 3D images were created. Quartz was the most abundant (60%) mineral constituent in all samples analyzed (see Figure 2-4). Although it appeared in the calcite laminae, quartz was abundant throughout the samples. The calculated hounsfield value was determined to be 1610. Feldspar composition was dominated by potassium, with minor plagioclase evident from the EMP analysis (see Figure 2-5). For analysis purposes, the feldspars were grouped together. Feldspar occurred in approximately 15% abundance. The range of hounsfield units for this group of minerals was calculated to be 1545 to 1645. These mineral analysis were compared to previously identified micro-facies (this volume, chapter 1).

In addition to analyzing greyscale images, a colour scale (available with the N-Reconstruction software) was used to help distinguish mineral phases (see Figure 2-6). Using this method, calcite was assigned blue, dolomite pink, pyrite white, quartz red to orange and feldspar yellow to pale orange. Using a colour scale allowed for better differentiation between phases. Three dimensional models were created showing the overall mineralogy of a small portion of sample (approximately 1mm by 3 mm by the depth of the sample (approximately 1 cm)). In addition, models showing quartz and feldspar only, calcite and dolomite only, pyrite only and porosity were made.

Porosity was found to be low overall (less than 2%) and was not observed to correspond to bedding. Pores are tiny (less than 1 mm) and appear between larger

grains. Pores appeared to be largely air filled, although because of the carbon coating and tiny nature of the pores, true carbon content was difficult to determine.

Discussion

  The mineralogical findings place this sample within microfacies 1 of (this volume, chapter 1) and classify it as a dolomitic lithic arkos. Although no mica was observed, aluminum content was confined to fine-grained laminae (observable in the EMP elemental maps), suggesting that resolution may have been too low to observe mica grains. Additionally, the true form of the pyrite observed (framboids or crystalline) could not be determined due to the small grain size, however pyrite framboids and crystalline pyrite have been observed within this microfacies (this volume, chapter 1). The calcite found within the dolomite grains fits with previous findings of dedolomite within this microfacies (see Figure 2-6; this volume, chapter 1). These previous findings found a detrital dolomite population which was dedolomitized and an authogenic population (this volume, chapter 1). The authogenic dolomite population appeared to nucleate off the dedolomitized portion and occurred in rhombohedral form (this volume, chapter 1).

  The replacement of the dolomite cores by calcite would require the interaction of the rock with fluids containing a high Ca^{2+}/Mg^{2+} ratio (Vandeginste and John, 2012). Dedolomitization is thought to require 1) a low partial pressure of CO_2, 2) a high rate of fluid flow to elevate the Ca^{2+}/Mg^{2+} ratio and 3) a low temperature (below 50℃; De Groot, 1967; Vandeginste and John, 2012). Generally thought to form under surface conditions, dedolomite can, however, form due to deep burial processes as well (Goldberg, 1967; Sanz-Rubio *et. al.,* 2001; Vandeginste and John, 2012).

  Two models have been used to explain the process of dedolomitization; 1) ferrous iron within the dolomite is oxidized due to subaerial exposure and 2) calcium-sulfate-rich fluids from the dissolution of evaporite minerals (gypsum or anhydrite) raise the Ca^{2+}/Mg^{2+} ratio, allowing for dolomite destabilization (Goldberg, 1967; Katz, 1971; Vandeginste and John, 2012). However, instantaneous precipitation of calcite

associated with dolomite dissolution and replacement (the two previous models) is not necessary (Vandeginste and John, 2012). Dolomite can be dissolved and the cavities infilled at a later time by calcite; this would involve a different solution (Jones *et.al.,* 1989; Vandeginste and John, 2012). This would allow for an increase in porosity if the voids were not completely infilled by calcite.

Because a *Glossifungites* surface was observed in the litholog (this volume, chapter 1), subaqeous exposure may have occurred and so the mechanism of dedolomitization may have involved ferrous iron oxidation. This would suggest that dolomite dissolution and replacement occurred concurrently (Katz, 1971) and so overall porosity may not have increased.

Minerals observed during these analyses are more or less homogeneously distributed. This should mean that fracture propagation is not hindered by geological heterogeneities. Porosity (and therefore permeability) should be both homogeneous and comparably isotropic. This would imply that permeability would be similar both vertically and horizontally. However, small sample size does make it difficult to determine the true significance of mineral distributions.

Factors that contributed to the success of mineralogical determination using EMP and micro-ct analysis include the ability to use the backscattered electron images to help resolve artifacts in the micro-ct images as well as the ability to refer to the XCOM database for verification. This analysis was made difficult, however, because of artifacts observed. Beam hardening, as well as line artifacts made mineralogical determination difficult at times. In addition, difficulties found in completely leveling the sample complicated the comparison between EMP images and the micro-ct images. Using a fully adjustable stage will eliminate this issue and make the comparison straightforward. Also, because element maps obtained using EMP are themselves qualitative in nature (because of error), in addition to artifacts generated during micro-ct analysis, this method of analysis qualitative as of yet. Reducing artifacts and improving EMP resolution would minimize these errors and allow for more quantitative analysis to take place. Using this method of calibration in partnership with other methods (such as dual energy scanning using micro-ct) would also allow for a more quantitative result. Additionally, the fine-grained nature (very fine

sand and silt) of the Montney Formation made analysis a challenge. Coarser grained samples would be much easier to resolve and would require lower resolution.

It should be emphasized that samples analyzed using this method must be done so perpendicular to bedding in order to analyze different laminae. Failure to align the sample in this fashion allows for the analysis of only a single bed or laminae.

Future work includes analyzing coarser grained samples to further determine the validity of this method. A precambrian dolomite and calcite sample will be analyzed. This will allow for a refinement of this method for carbonate determination. Moreover, sample coatings will also be explored. The epoxy coating, in addition to stabilizing the sample, seemed to reduce artifacts (including beam hardening). This aspect requires further exploration. Coating the analyzed surface with epoxy after EMP analysis may help to further reduce artifact issues and make surface alignment easier.

Conclusions

Using electron microprobe and micro-ct analysis, a sample of the Lower Triassic Montney Formation was examined. This analysis revealed that the sample was quartz-rich with low porosity and fit with previous findings about Montney mineralogy and porosity (this volume, chapter 1). This sample was determined to correspond to microfacis 3 described by (this volume, chapter 1).

Using this sample, the technique of calibrating micro-ct images using EMP element maps was evaluated. This technique was found to be valid for semi-quantitave analysis only, as of yet. This is owing to artifacts and stage position complicating interpretations. Coupling this method with other methods (dual energy scanning, etc.) in addition to artifact reduction using sample coating and improved EMP resolution would allow for quantitative applications. A larger grained sample of dolomite and calcite only will be scanned in future to further explore this method. In addition, sample coating will also be explored to see if image artifacts (such as beam hardening) can be reduced.

Mineral	Formula	xray absorption coefficient
Quartz	SiO_2	0.1684
Pyrite	FeS_2	0.2810
Dolomite	$(CaMg)(CO_3)_2$	0.1786
Calcite	$CaCO_3$	0.1955
Orthoclase	$KAlSi_3O_8$	0.1764
Albite	$NaAlSi_3O_8$	0.1661
Anorthite	$CaAlSi_3O_8$	0.1790
Muscovite	$KAl_2(AlSi_3O_{10})(F,OH)_2$	0.1707

Table 2-1 Attenuation coefficients generated from XCOM (hosted by NIST, http://physics.nist.gov/PhysRefData/Xcom/html/xcom1.html) for select mineral phases. Values represent total attenuation with coherent scattering at 100kV. All x-ray absorption coefficients are given in cm²/g.

Figure 2-1 Greyscale image taken using micro-ct. Shade is determined by density via atomic number; the denser the mineral, the lighter the grey. Note the bright white spots are pyrite, the most dense of the observable mineral phases. Calcite appears as light grey and is seen to be concentrated within laminae. Dolomite, quartz and feldspar are more difficult to distinguish within this image because the attenuation coefficients are closer in value.
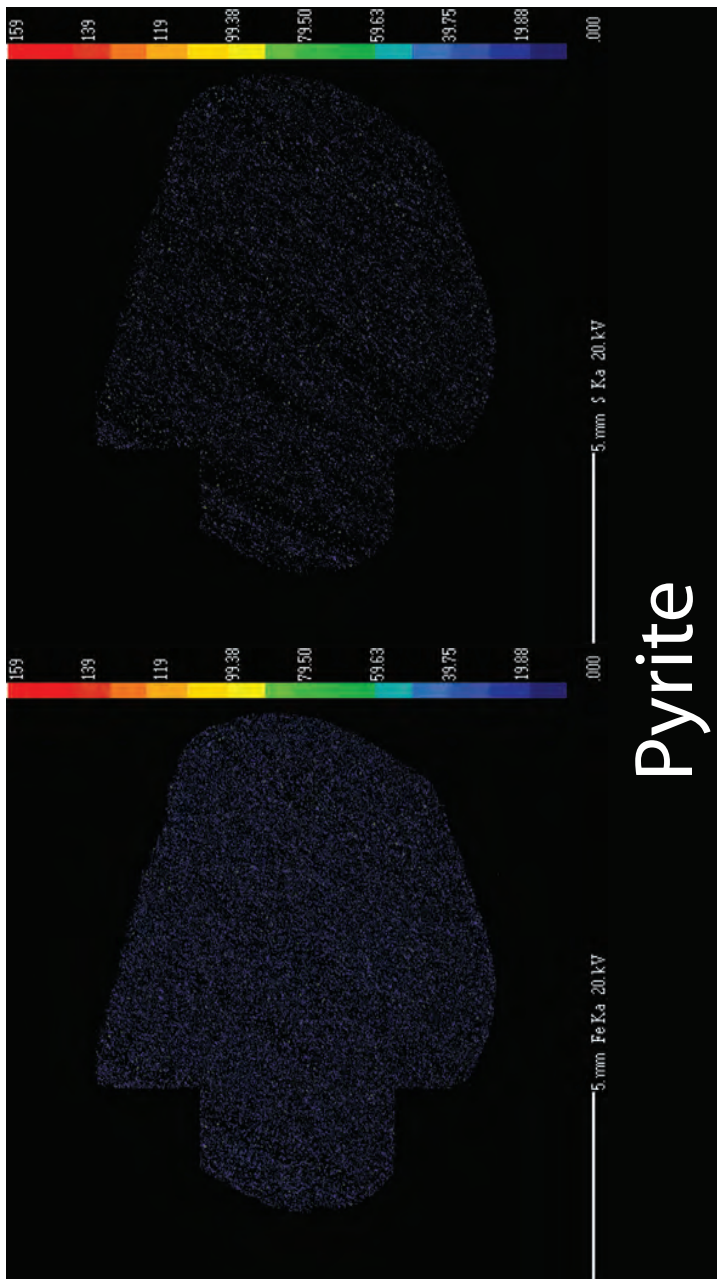
Figure 2-2 Electron microprobe element maps (false colour images) showing concentrations of iron (left) and sulfur (right). Displayed colour scales are determined from the relative concentrations of an element within the sample. In these images, brightly coloured regions (toward the red end of the spectrum) which overlap in both images indicate the presence of pyrite. These bright spots correlate with the white regions seen in the greyscale micro-ct image as well as the backscattered electron image. Pyrite occurs in abundance of 5%.
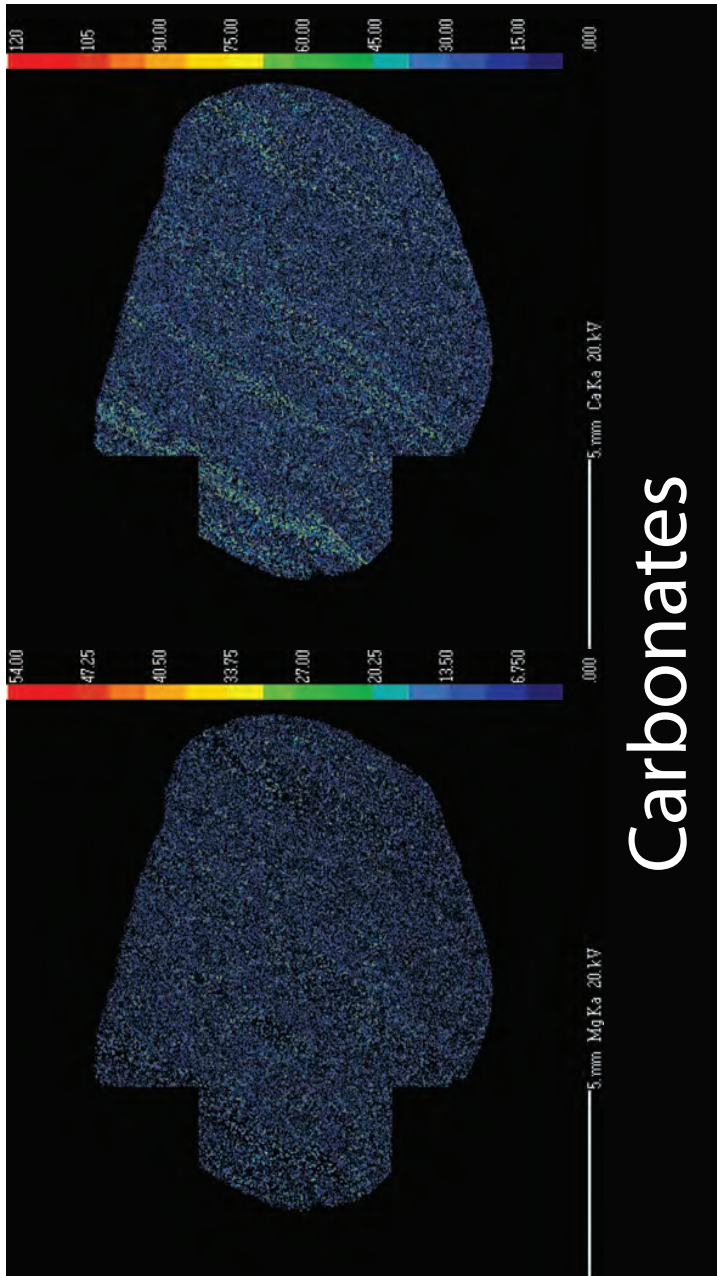
Figure 2-3 Electron microprobe element maps (false colour images) showing concentrations of magnesium (left) and calcium (right). Displayed colour scales are determined from the relative concentrations of an element within the sample. In these images, overlapping regions of relative high abundance exclusive of silicon (see Figure 4) denote dolomite. Dolomite appears as green to yellow in the magnesium map. High abundances of calcium (green to red), exclusive of silicon, represent the mineral calcite. Comparison of the calcite element map with the element map of silicon was necessary to distinguish calcium-bearing feldspar from dolomite and calcite.
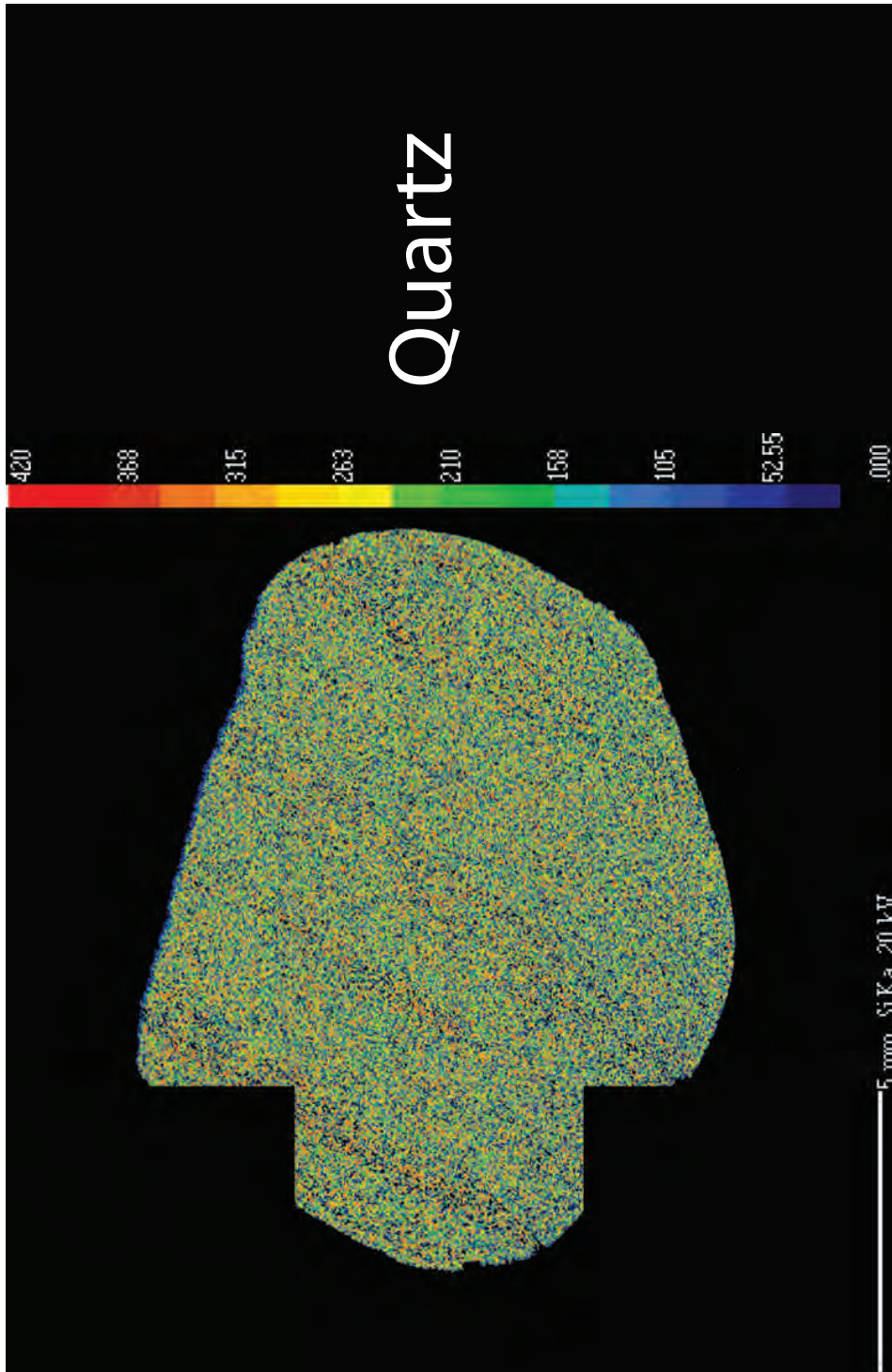
Figure 2-4 Electron microprobe element map (false colour images) showing concentrations of silicon. The displayed colour scale is determined from the relative concentrations of silicon within the sample. Occurrences of quartz are denoted by regions of high intensity colour (pale green to red). Initial comparison with the element maps showing calcium and potassium was necessary to distinguish regions of quartz from feldspar. Note the high abundance of Quartz (60%).
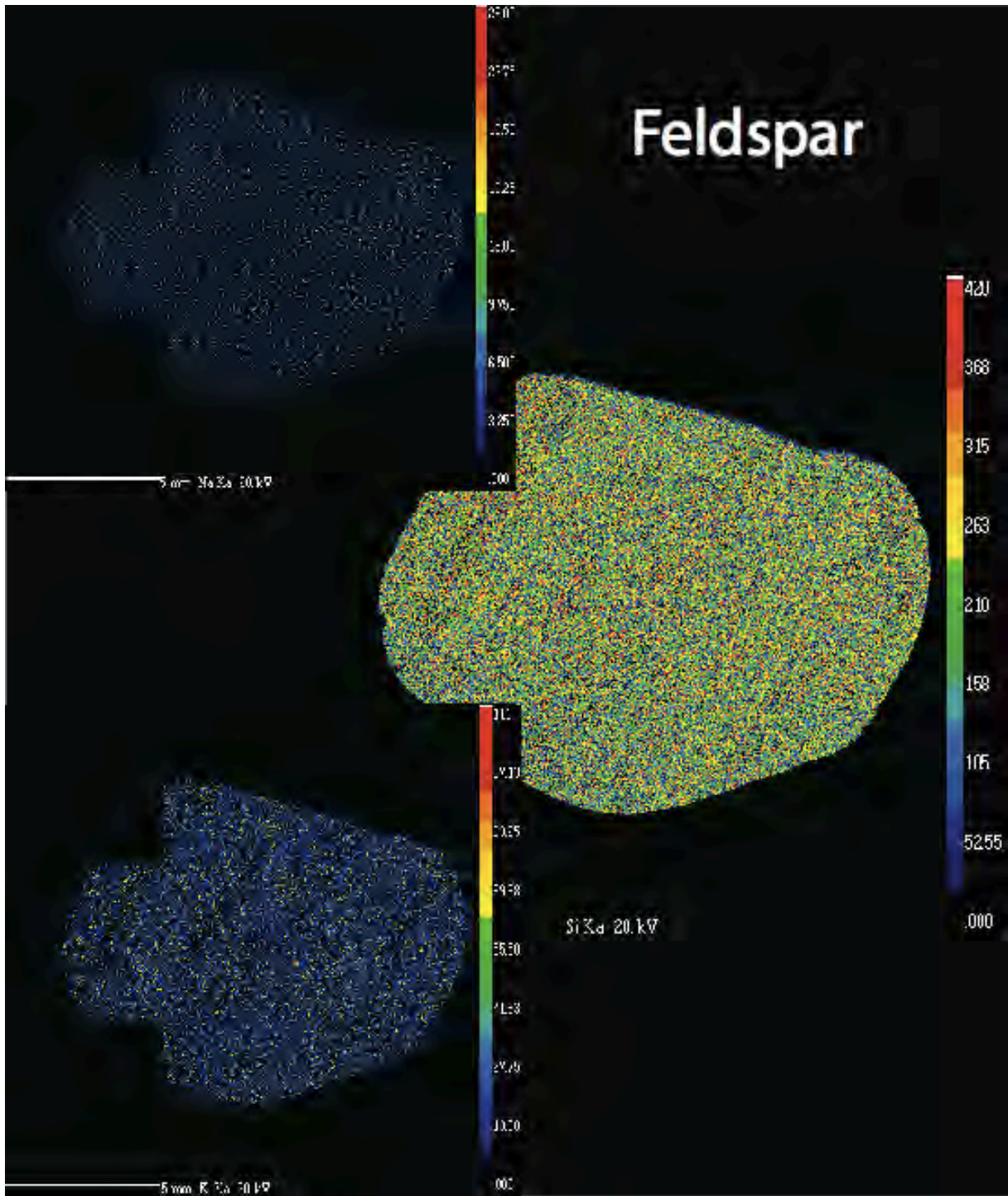
Figure 2-5 Electron microprobe element maps (false colour images) showing concentrations of sodium (top left), silicon (right) and potassium (bottom left). The displayed colour scales are determined from the relative concentrations of an element within the sample. For ease of analysis, feldspars (plagioclase and potassium feldspar) were grouped together. Again, occurrence is denoted where brightly coloured regions overlap between the three maps.
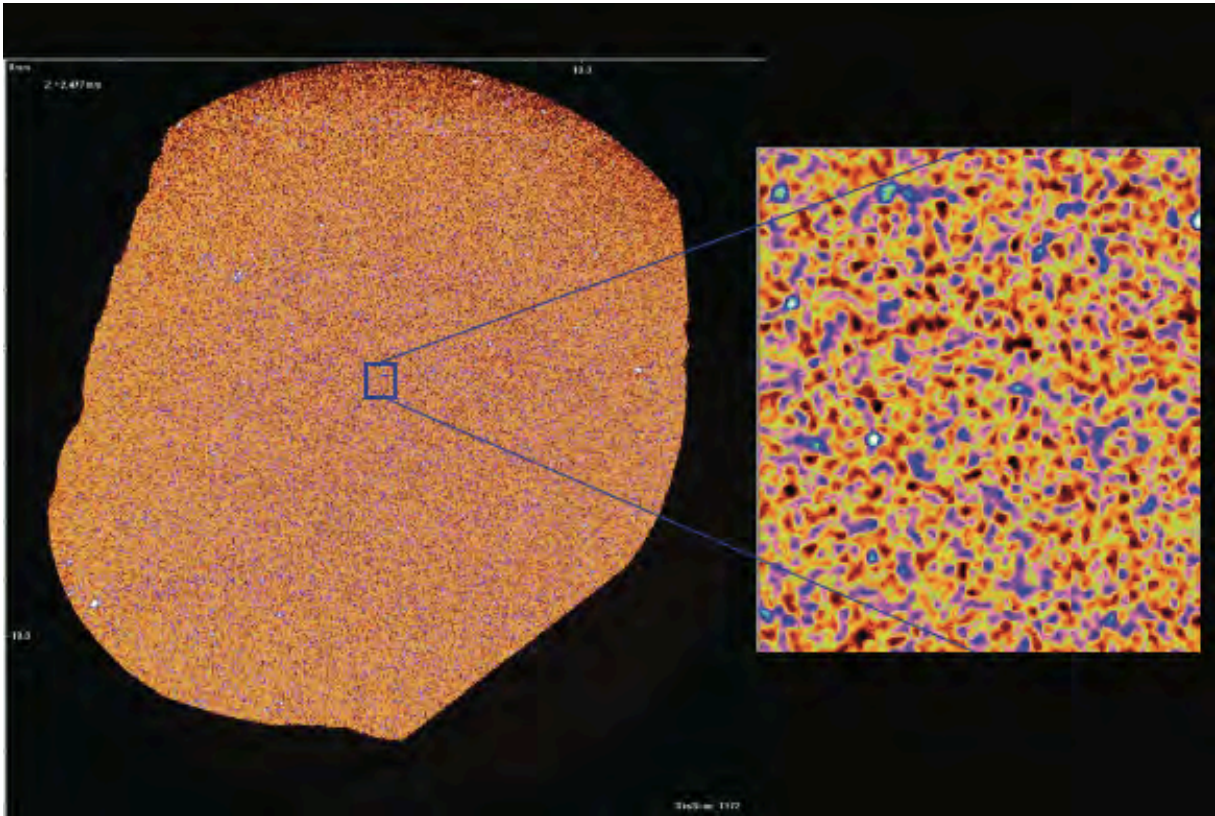
Figure 2-6 Micro-ct image utilizing a colour scale. Scale bars (in mm) are visible along the top and side. In this image, calcite is blue, dolomite pink, pyrite white, quartz red to orange and feldspar yellow to pale orange. The inset shows a close up of the sample where dolomite can be seen to have calcite cores (interpreted to be dedolomite).
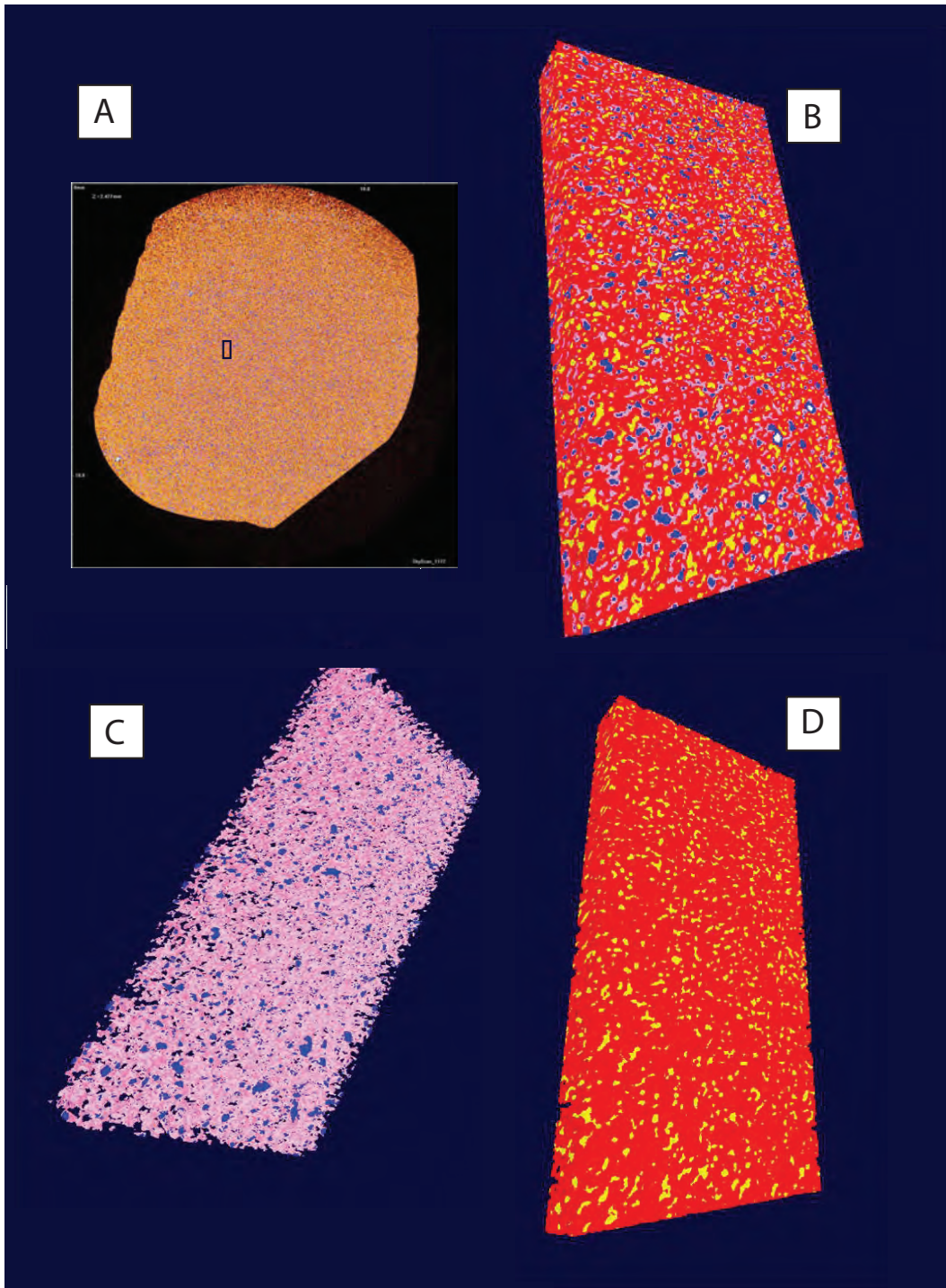
Figure 2-7 Rendered three dimensional models showing different mineral phases in a small subsection of the sample (denoted by the small rectangle in image A). The first model (B) shows all of the major mineral constituents (pyrite in white, calcite in blue, dolomite in pink, feldspars in yellow and quartz in red). The second (C) shows carbonates only. The third (D) shows quartz and feldspar only. Dedolomite is interpreted to be visible where pink regions (dolomite) have calcite cores (blue; see image B).

References

Bertels, S.P., Dicarlo, D.A. and Blunt, M.J., 2001. Measurement of aperture
distribution, capillary pressure, relative permeability, and in situ saturation in
a rock fracture using computerized tomography scanning. Water Resources
Research v. 37, p.649-662.

Brooks, R.A. and Di Chiro, G., 1976. Beam hardening in X-ray reconstructive
tomography. Physics in Medicine and Biology v. 21, p. 390-398.

Coenen, J.G.C. and Maas, J.G., 1994. Material classification by dual-energy
computerized X-ray tomography. In: Proceedings on the International
Symposium on Computerized Tomography for Industrial Applications, Berlin,
p. 120-127.

Coles, M.E., Hazlett, R.D., Spanne, P., Soll, W.E., Muegge, E.L. and Jones, K.W.,
1998. Pore level imaging of fluid transport using synchrotron X-ray
microtomography. Journal of Petroleum Science and Engineering v. 19, p.
55-63.

Davies, G.R. 1997. The Triassic of the Western Canada Sedimentary Basin: tectonic
and stratigraphic framework, Palaeogeography, Paleoclimate and biota. In:
Triassic of the Western Canada Sedimentary Basin. T.F. Moslow and J.
Wittenberg (eds.) Bulletin of Canadian Petroleum Geology, v. 45, pages
434-460.

Davies, G.R., Moslow, T.F. and Sherwin, M.D. 1997. The Lower Triassic Montney
Formation, west-central Alberta. In: Triassic of the Western Canada
Sedimentary Basin. T.F. Moslow and J. Wittenberg (eds.) Bulletin of Canadian
Petroleum Geology, v. 45, pages 474-505.

De Groot, K., 1967. Experimental dedolomitization. Journal of Sedimentary Petrology, v. 37, p. 1216–1220.

Dixon, J. 2000. Regional lithostratigraphic units in the Triassic Montney Formation of western Canada. Bulletin of Canadian Petroleum Geology, v.48, pages 80-83.

Duliu, O., 1999. Computer axial tomography in geosciences: An overview. Earth-Science Reviews v. 48, p. 265–281.

Faraj, B., Harold, W., Addison, G., McKinstry, B., Donaleshen, R., Sloan, G., Lee, J., Anderson, T., Leal, R., Anderson,C., Lafleur, C., and A. Ahlstrom, 2002. Shale gas potential of selected Upper Cretaceous, Jurassic, Triassic and Devonian shale formations in the WCSB of Western Canada: Implications for shale gas production. Gas Technology Institute. Des Plaines, Illinois. 103 pages.

Goldberg, M., 1967. Supratidal dolomitization and dedolomitization in Jurassic rocks of Hamakhtesh Haqatan, Israel. Journal of Sedimentary Petrology, v. 37, p. 760–773.

Hayes, L.E., Beatty, T.W., Henderson, C.M., Love, G.D., and Summons, R.E., 2007. Evidence for photic zone euxinia through the end-Permian mass extinction in the Panthalassic Ocean (Peace River Basin, Western Canada): Palaeoworld, v. 16, p. 39-50.

Ibrahimbas, A. and Riediger, C. 2004. Hydrocarbon source rock potential as determined by Rock-Eval 6/TOC pyrolysis, Northeast British Columbia and Northwest Alberta. British Columbia Ministry of Energy, Mines and Petroleum Resources, Summary of Activities, p. 7-17.

Jones, B., Pleydell, S.M., Kwoi-Choi, N., AND Longstaffe, F.J., 1989. Formation of poikilotopic calcite–dolomite fabrics in the Oligocene–Miocene Bluff formation of

Grand Cayman, British West Indies. Bulletin of Canadian Petroleum Geology, v. 37, p. 255–265.

Katz, A., 1971. Zoned dolomite crystals. Journal of Geology, v. 79, p. 38–51.

Kenter, J.A.M., 1989. Applications of computerized-tomography in sedimentology. Marine Geotechnology v. 8, p. 201–211.

Long, H., Swennen, R., Foubert, A., Dierick, M. and Jacobs, P., 2009. 3D quantification of mineral components and porosity distribution in Westphalian C sandstone by microfocus X-ray computed tomography. Sedimentary Geology v. 220, p. 116-125.

Mees, F., Swennen, R., Van Geet, M., Jacobs, P., 2003. Applications of X-ray Computed Tomography in the Geosciences. Geological Society, London. Special Publications v. 215, 243p.

Monga, O., Bousso, M., Garnier, P., and Pot, V., 2008. 3d geometric structures and biological activity: Application to microbial soil organic matter decomposition in pore space. Ecological Modeling v. 216, p. 291–302.

Moslow, T.F. and Davies, G.R. 1997. Turbidite reservoir facies in the Lower Montney Formation, west-central Alberta. In: Triassic of the Western Canada Sedimentary Basin. T.F. Moslow and J. Wittenberg (eds.), Bulletin of Canadian Petroleum Geology v. 45, p. 507-536.

Moslow, T.F. 2000. Reservoir architecture of a fine-grained turbidite system: Lower Triassic Montney Formation, Western Canada Sedimentary Basin. In: Deep-water reservoirs of the world, Conference Proceedings, Gulf Coast SEPM. P. Weimer, R.M. Slatt, J. Coleman, N.C. Rosen, H. Nelson, A.H. Bouma, M.J. Styzen, and D.T. Lawrence (eds.). p. 686-713.

Pullan, B.R., Ritchings, R.T. and Isherwood, I., 1981. Accuracy and meaning of computed tomography attenuation values. In: Newton, T.H., Potts, D.G. (Eds.), Radiology of the Skull and Brain: Technical Aspects of Computed Tomography. C.V. Mosby Company, St.-Louis, USA, p. 3904-3917.

Remeysen, K. and Swennen, R., 2006. Beam hardening artifact reduction in microfocus computed tomography for improved quantitative coal characterization. International Journal of Coal Geology v. 67, p. 101-111.

Remeysen, K. and Swennen, R., 2008. Application of microfocus computed tomography in carbonate reservoir characterization: Possibilities and limitations. Marine and Petroleum Geology v. 25, p. 486-499.

Sanz-Rubio, E., Sa´ Nchez-Moral, S., Can˜ Aeras, J.C., Calvo, J.P., and Rouchy, J.M.,2001. Calcitization of Mg-Ca carbonate and Ca sulphate deposits in a continental Tertiary basin (Calatayud Basin, NE Spain). Sedimentary Geology, v. 140, p. 123–142.

SkyScan N.V., 2005, SkyScan 1172 Desktop X-ray Microtomograph Instruction Manual, 53 p.

Snelling, A., Zalasiewicz, J., and Reeds, I., 2010. Using x-ray images to analyze graptolite distribution and alignment in welsh mudrocks. Proceedings of the Yorksire Geological Society v. 58, p. 129–140.

Utting, J., MacNaughton, R.B., Zonneveld, J-P., and Fallas, K., 2005. Palynostratigraphy, organic matter and thermal maturity of the Lower Triassic Toad, Grayling and Montney formations of Yukon, British Columbia and Alberta and comparison with the Sverdrup Basin, Nunavut. BCPG 53: 5-24.

Vandeginste, V. and John, C.M. 2012. Influence of climate and dolomite composition on dedolomitization: insights from a multi-proxy study in the Central Oman Mountains. Journal of Sedimentary Research, v. 82, p. 177-195.

Van Geet, M., Swennen, R. and Wevers, M., 2000. Quantitative analysis of reservoir rocks by microfocus X-ray computerized tomography. Sedimentary Geology v. 132, p. 25-36.

Van Geet, M. and Swennen, R., 2001. Quantitative 3D-fracture analysis by means of microfocus computer tomography (µCT): an example from coal. Geophysical research letters v. 28, p. 3333-3336.

Van Geet, M., Swennen, R. and Wevers, M., 2001. Towards 3-D petrography: application of microfocus computer tomography in geological science. Computers & Geosciences v. 27, p. 1091-1099.

Van Geet, M., Swennen, R., Durmishi, C., Roure, F. and Muchez, P., 2002. Paragenesis of Cretaceous to Eocene carbonate reservoirs in the Ionian fold and thrust belt (Albania): relation between tectonism and fluid flow. Sedimentology v. 49, p. 697-718.

Wellington, S.L., and Vinegar, H.J., 1987. X-ray computerized tomography. Journal of Petroleum Technology v. 39, p. 885-898.

Zhou, N., Matsumoto, T., Hosokawa, T., and Suekane, T., 2010. Pore-scale visualization of gas trapping in porous media by x-ray ct scanning. Flow Measurement and Instrumentation v. 21, p. 262–267.

Zonneveld, J-P., Gingras, M.K. and Beatty, T.W. 2010. Diverse ichnofossil assemblages from the Lower Triassic of northeastern British Columbia:

evidence for shallow marine refugia on the northwestern coast of Pangaea. Palaios, v. 25, p. 368-392.

Conclusion

Analysis of 14 thin sections from the Upper Montney Formation (obtained from well d-48-A/94-b-9 in the Kobes area of northeastern British Columbia, Canada) was conducted using electron microprobe (EMP), scanning electron microscope (SEM) and petrographic imaging. An additional sample was analyzed using microfocus computed tomography (micro-ct) and EMP. Five microfacies were identified, one of which may in fact be from the Doig Formation (occurrence is near the Doig phosphate zone). Deposition is thought to have occurred dominantly *via* ephemeral river input and storm activity along the coast. Trace fossil analysis suggests a stressed environment with rare bioturbation. Bioturbation observed may be sourced from doomed pioneers (Föllmi and Grimm, 1990). Pyrite analysis reveals deposition in a dysoxic environment. Anoxia spikes were observed, however, in association with an increase in carbonate content and may reflect periods of an elevated carbonate compensation depth (ccd) and an increase in alkalinity (Beauchamp and Grasby, 2012). The presence of significant pyrite suggests the presence of a shallow redox zone during deposition.

Thin section analysis reveals dominance by sub-mature grains (i.e. sub-angular, moderately to moderately well sorted). Mineralogy includes abundant carbonates (calcite and dolomite), quartz, feldspar, muscovite and opaques such as pyrite. Some kerogen is also present. Alternating bands of light (1-3mm) and dark sediment (1mm-0.5cm) occur, which are related to the dominant grain size. Dark bands correspond to areas dominated by very fine grained sediment (medium silt). Light bands consist of relatively coarse grains (very fine sand). Regarding the reservoir character, the observed porosity is variable, even at the decimetre scale, however high intergranular porosity is observed in some thin sections. Intraparticle porosity due to the presence of dissolved carbonate grains also contributes to the overall porosity.

Aeolian sourcing of the Montney sediments (Davies, 1997), most notably the dolomite fraction, is considered to be minor. An expectation of aeolian transport is that the sediment will be well sorted, sub-rounded to rounded, and dominantly mono-

mineralic in its composition. The poor to moderate sorting and polymictic nature of Montney sandstone samples analysed herein suggests that other (likely aqueous) means of sediment transport was the dominant depositional process. Therefore, fluvial transport to the coastline, likely through a periodically active ephemeral system seems a more likely hypothesis. Offshore-oriented sediment transport likely occurred by sediment hyperpycnal flows and storm-related turbidites. This assertion is supported by the presence of abundant sharp-based, graded beds and common localized soft-sediment deformation features. This hypotheses requires, however, a source of detrital dolomite which could be explained by the production of dolomite by sulfate-reducing bacteria.

Scanning electron microscope (SEM) analysis reveals a distinct depositional and diagenetic history, which includes the deposition of detrital dolomite, feldspar, quartz, mica, calcite and organic matter. After shallow burial, or near the sediment-water interface, small pyrite spheres precipitated within pore spaces. Following deeper burial, dedolomitization, evidenced by corroded dolomite grains, accompanied by calcite cementation occurred. This was likely accompanied, and followed by, gas production associated with kerogen trapped in pore spaces. The ubiquitous presence of kerogen probably contributed to the preservation of porosity during deeper burial. In short, the petrogenetic model for the Montney in the Kobes region suggests that the critical depositional / diagenetic phases that contributed to its resource potential are: (1) the preservation of kerogen in a low-oxygen setting; (2) rapid passage through the sulphate reducing zone in the sediment so that porosity is not occluded by pyrite precipitation and organics are not consumed by sulphate reduction; (3) the limited extent to which later calcite cement has occupied porosity (possibly affected by pH in the presence of organic materials); and (4) the generation of more porosity through minor dedolomitization.

Comparative analysis using electron microprobe (EMP) and micro-ct scanning was successfully carried out using a sample of the Upper Montney from the same well. Mineral phases identified during EMP analysis have been correlated with specific density signatures identified with the micro-ct scanner. This has allowed for 3-

D characterization of the mineralogy of fine-grained Montney sample. Mineral phases identified include quartz (60%), feldspar (15%), dolomite (12%), calcite (8%) and pyrite (5%). This analysis revealed the sample to be a dolomitic lithic arkos with low porosity (less than 2%). Although successful, this analysis proved to be semi-quantitative only because of errors associated with the EMP analysis and artifacts produced during micro-ct scanning. Mineral percentages were therefore more accurately determined by comparison with previously identified micro-facies. Reduction of these errors and artifacts, in addition to improved stage alignment within the micro-ct machine will improve analysis and potentially allow for quantitative evaluations to take place.

References

Davies, G.R. 1997. The Triassic of the Western Canada Sedimentary Basin: tectonic and stratigraphic framework, Palaeogeography, Paleoclimate and biota. In: Triassic of the Western Canada Sedimentary Basin. T.F. Moslow and J. Wittenberg (eds.) Bulletin of Canadian Petroleum Geology, v. 45, p. 434-460.

Beauchamp, B. and Grasby, S.E. 2012. Permian lysocline shoaling and ocean acidification along NW Pangea led to carbonate eradication and chert expansion. Palaeogeography, Palaeoclimatology, Palaeoecology, v. 350-352, p. 73-90.

Föllmi, K.B. and Grimm, K.A. 1990. Doomed pioneers: gravity-flow deposition and bioturbation in marine oxygen-deficient environments: Geology, v. 18, p. 1069-1072.